This is to certify that the
dissertation entitled

THERMOELECTRIC MATERIAL CHARACTERIZATION AND
MODULE FABRICATION

presented by

Jonathan James D'Angelo

has been accepted towards fulfillment
of the requirements for the

Doctor of Philosophy degree in Electrical Engineering

Major Professor's Signature

9-15-2009

Date

THERMOELECTRIC MATERIAL CHARACTERIZATION AND MODULE FABRICATION

By

Jonathan James D'Angelo

A DISSERTATION

Submitted to
Michigan State University
in partial fulfillment of the requirements
for the degree of

DOCTOR OF PHILSOPHY

Electrical Engineering

2009

ABSTRACT

THERMOELECTRIC MATERIAL CHARACTERIZATION AND MODULE FABRICATION

By

Jonathan James D'Angelo

Thermoelectric generators operate with no moving parts to convert heat flow to electricity. Significant interest in developing new materials in recent years has led to the discovery of several promising thermoelectrics; however there can be considerable challenges in developing the materials into working devices. Testing and feedback is needed at each step to gain valuable information for identification of difficulties in; quality of the materials and modules, electrical contacts to the materials, repeatability in fabrication, and longevity of the devices. The goal of this dissertation is to show results in all of these categories.

Acknowledgements

I would like to thank the generous support of the Office of Naval Research and Strategic Environmental Research and Development Program. I would also like to acknowledge the support and guidance given to me by my advisor, Dr. Timothy Hogan. Lastly, I would like to say thank you to my mother and father; thank you mom, this is for you.

TABLE OF CONTENTS

LIST OF TABLES

LIST OF FIGURES

1.0 Introduction

1.1 The "Thermomagnetic Effect"

In early 1820, Thomas Seebeck was experimenting with the possibility of a relationship between heat and electricity [1]. His experimental setup was a current loop formed by the junctions at both ends of a copper and a bismuth wire. Seebeck heated up one of the copper-bismuth junctions while the other remained at room temperature. What he measured was a magnetic field radiating from the wire. He believed that the temperature gradient was causing the magnetic field. He called this the "Thermomagnetic Effect." This is was wrong. The magnetic field that he measured was produce by the current flowing due to the temperature gradient in the current loop, however the relationship between current flow and magnetic field was not known at that time. If one of the wires is cut, then no magnetic field results; instead a voltage can be measured at the open circuit terminals. This voltage is the Seebeck coefficient for the junction formed by those metals, and is a temperature integral sum of the thermopowers (or absolute Seebeck coefficients) of each metal.

In 1834 when another scientist by the name of Peltier discovered that when electricity is forced to flow through a junction of dissimilar metals, heat would either be absorbed or liberated at the junction based on the direction of current flow [2].

Later Thomson showed that heating or cooling along the length of a single material also takes place when electrical current flows through the material. This

became known as the Thomson Effect. Today's thermoelectric devices are based on these scientific principles.

1.2 Thermoelectric Devices

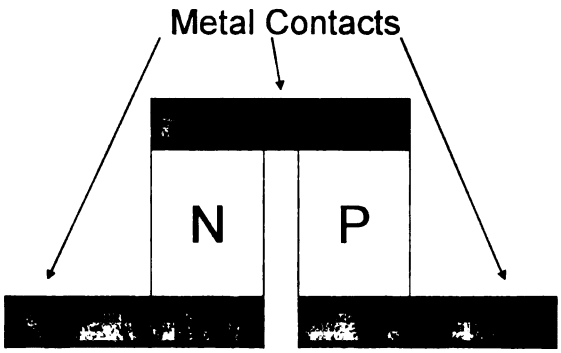

Figure 1: Thermoelectric Device.

Figure 1 shows a single junction (unicouple) between n-type and p-type thermoelectric material in a standard thermoelectric device. Both the n-type and p-type materials are doped to degeneracy and form ohmic contacts to the electrodes; thus although it is an n-type to p-type structure it does not form a diode and these devices exhibit linear current vs. voltage profiles.

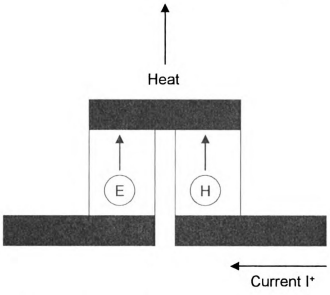

Figure 2: Thermoelectric heating device (E-Electrons in n-type leg, H-Holes in p-type leg).

By supplying electrical power to this device as shown in Figure 2 heat can be pumped from one side of the device to the other to establish a temperature gradient. Heat will flow through the p-type leg in the same direction as the electrical current flow through that leg. The carriers, or holes, in the p-type material move in the direction of current flow and also carry heat from the bottom of the device to the top. The electrons on the n-type side are also moving in the same upwards direction along the device, also carrying heat. This makes the top side of the device hot and cools the bottom of the device as shown in Figure 2. With this same layout and reversing the current direction, the top of the device will then be cooled following the same principles.

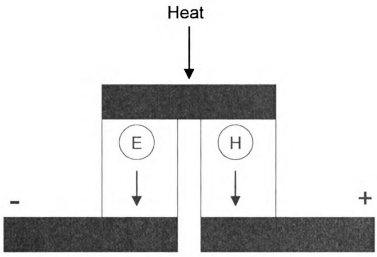

Figure 3: Thermoelectric power generation device.

These devices, thus serve as heat pumps. If instead of supplying electrical power to the device in order to create a temperature gradient, a temperature gradient is supplied to the device, then electrical power can be generated. The larger the temperature gradient the more voltage produced by the module. A portion of the heat supplied to the module is carried to the cold side of the device by the electrons in the n-type and the holes in the p-type. This makes one side a positive potential and the other a negative, and can be attached to an electrical circuit and be used as a power supply. There are a number of advantages for using thermoelectric devices as listed in the next section, however the most significant disadvantage is the relatively low efficiency in thermal to electric energy conversion (typically 5% for Bi2Te3 based devices).

1.3 Advantages of Thermoelectrics

The science of thermoelectrics was born some time ago, now a number of companies are based on their fabrication and application. Most thermoelectrics are used for cooling and heating devices. A list of advantages includes[3];

1. No moving parts for long device lifetimes and little maintenance
2. They can be made into small or large devices without loss of efficiency
3. The same module can be used as a power generator and a cooler
4. They can operate in any orientation
5. They give very little electronic noise
6. They can be used for accurate temperature control

Common thermoelectric materials and their operating temperatures are given in Table 1.

Table 1: Common thermoelectric materials, maximum operating temperature, maximum figure of merit (Z), and their temperature of Z_{max}.

	Z_{max} (K^{-1})	Useful Range	T_{Zmax} (K)
Bi_2Te_3	$3x10^{-3}$	< 500 K	300
PbTe	$1.7x10^{-3}$	< 900 K	650
Si-Ge	$1x10^{-3}$	< 1300 K	1100

The figure of merit, Z, is used to evaluate thermoelectric materials, has units of (1/K) and is based on the material properties of electrical conductivity, Seebeck coefficient (or thermopower), and thermal conductivity. The unitless figure of merit, *ZT* is given by

$$ZT = \frac{S^2\sigma}{\kappa} \cdot T \qquad (1)$$

where S is the thermopower, σ is the electrical conductivity, κ is thermal conductivity, and T is temperature. To obtain a high ZT the thermopower and electrical conductivity must be high, and the thermal conductivity should be low. Maximizing ZT can be challenging as these materials properties are not independent of one another. Usually a material that has a higher electrical conductivity will have a low thermopower, and a high thermal conductivity. This behavior is seen in most conductors, such as copper. For insulators, such as glass, a low thermal conductivity and a high thermopower is typically accompanied by a very low electrical conductivity. Optimization of the three material properties is generally found in heavily doped semiconductors [4].

Modules that use bismuth telluride as their thermoelectric materials operate near room temperature, and solder contacts can be used to bond both the hot and cold side electrical-mechanical junctions. The devices built here at Michigan State University need to have bonds on the hot junctions that can withstand rigorous temperature cycling and high temperature operations where solder contacts are not possible. The Chemistry Department at Michigan State University has discovered several chalcogenide based materials that have shown promising thermoelectric properties [5]. Recently compounds in the $Ag_{1-x}Pb_mSbTe_{2+m}$ and $Ag(Pb_{1-x}Sn_x)_mSbTe_{2+m}$ systems have exhibited outstanding thermoelectric properties for power generation applications [6].

Lead antimony silver tellurium or also know as LAST and lead-antimony-silver-tin-tellurium, or LASTT, are the n-type and p-type materials (respectively) used for fabrication of the thermoelectric devices. The purpose of this dissertation is to give the research of both high and low temperature electrical contacts of metals to LAST materials. The contact resistance drops the efficiency of the device and thus should be minimized.

2.0 Literature Review

2.1 The Foundations of Thermoelectrics

For fabrication of thermoelectric refrigeration devices there are many important contributions for the development of the modules. Metals with the highest thermopowers are needed. These are antimony and bismuth alloys [7].

There is a great importance of the electrical contacts at the junctions. Large contact resistances between the thermoelectric and the metal electrode are detrimental to the efficiency of the thermoelectric module.

The minimization of the thermal conductivity is important. It has an electronic and lattice component. The electronic contribution can be small for insulator, and lightly doped semiconductors. For metals and highly doped semiconductors the electronic contribution is amplified. The lattice component comes from phonon scattering in the lattice.

For materials to have the highest figure of merit possible it is desirable to have a ratio of the carrier mobility to the thermal conductivity to be large, and the effective mass of the carriers to be as large as possible. Therefore semiconductors

used for thermoelectric refrigeration should be chosen with the highest mean atomic weights for reduced lattice thermal conductivity contributions, and with large effective masses of the charge carriers. Goldsmid suggested in 1954 that Bi_2Te_3 as a potential candidate for thermoelectric devices and it is still used today.

The highest ZT for room temperature materials was seen in $(Bi_2Te_3)_{0.25}(Sb_2Te_3)(Sb_2Se_3)_{0.03}$ [8]. This alloy has a Z of $3.4x10^{-3}K^{-1}$ and a room temperature resistivity of 1.1mΩcm.

2.2 Properties of Good Thermoelectric Materials [9]

Thermoelectrics (TE) need electronic bands near the Fermi level with many valleys preferably away from the Brillouin zone boundaries to improve thermopower and mobility. Such high degeneracy is typically found in crystals with high symmetry. TE's elements with large atomic numbers and large spin-orbit coupling helps to lower the overall thermal conductivity. Compositions with more than two elements also lowers the thermal conductivity. A low average electronegativity difference between the elements improves mobility. A large unit cell with many atoms will lower the thermal conductivity. Having an energy gap equal to about $10k_BT$, where T is the operating temperature of the thermoelectric, and k_B is Boltzman's constant improves the thermopower. The band gap for room temperature materials should range from 0 to 0.3eV.

2.3 *B* Factor; 3D and 2D

Chasmar and Stratton first introduced the *B* parameter in 1959 [10]. The *B* parameter is directly proportional to the βE_g, which is the energy gap divided by the thermal energy. $ZT=F(B,\beta E_g)$, where $\beta=1/k_BT$.

$$B = \gamma \frac{1}{3\pi^2}\left(\frac{2k_BT}{h^2}\right)^{3/2}\sqrt{m_x m_y m_z}\,\frac{k_B^2}{e\kappa_l}\mu_x \tag{2}$$

where *m* is the effective mass in the its corresponding crystallographic direction, μ_x is the mobility in the *x* direction, or it can be set to the direction of majority transport, and γ is the degeneracy of the bands for the carries in the material.

A high *B* factor translates to a high figure of merit. In the formula shown above, a highly anisotropic material can be utilized if the highest mobility direction can be chosen to correspond to the electrical current flow direction. This approach may counter attempts to increase the *B* factor through large band degeneracy, which is commonly found in highly symmetric crystal structures, for example cubic. It is also beneficial to have many atoms in the unit cell. Highly anisotropic effective masses are not found in such materials. Bi_2Te_3 has a band degeneracy of six.

Below is shown a calculation of *Z* through the chemical potential and *B* factor for the 3D case [11]. The following assumption are made for the calculations; a general, anisotropic, one-band material, constant relaxation times, and parabolic bands.

$$E\left(k_x,k_y,k_z\right)=\frac{h^2k_x^2}{2m_x}+\frac{h^2k_y^2}{2m_y}+\frac{h^2k_z^2}{2m_z} \tag{3}$$

is the energy for parabolic bands.

The electrical conductivity is defined as,

$$\sigma = \frac{1}{2\pi^2}\left(\frac{2k_BT}{\hbar^2}\right)^{3/2}\left(m_x m_y m_z\right)^{1/2} F_{1/2} q_e \mu_x \tag{4}$$

The thermopower and electronic contribution of the thermal conductivity are as follows;

$$S = -\frac{k_B}{q_e}\left(\frac{5}{3}\frac{F_{3/2}}{F_{1/2}} - \zeta^*\right) \tag{5}$$

$$\kappa_e = \frac{\pi\hbar^2}{6\pi^2}\left(\frac{2k_BT}{\hbar^2}\right)^{5/2}\left(\frac{m_y m_z}{m_x}\right)^{1/2} \times k_B\left(\frac{7}{2}F_{5/2} - \frac{25F_{3/2}^2}{6F_{1/2}}\right) \tag{6}$$

$$F_i = F_i\left(\zeta^*\right) = \int_0^\infty \frac{x^i}{e^{x-\zeta^*}+1}dx \tag{7}$$

$\zeta^* = \frac{\zeta}{k_BT}$ is the reduced chemical potential relative to the edge of the conduction band, q_e is the magnitude of the electronic charge [1.602×10^{-19} (C)], m_x, m_y, m_z are the effective mass components, and μ_x is the mobility in the x-direction. This shows the thermopower gives a measure of the reduced chemical potential, which can be used in conjunction with measured electrical conductivity to gain insight on the factor of $\mu_x\left(m_x m_y m_z\right)^{1/2} = q_e\tau\left(\frac{m_y m_z}{m_x}\right)^{1/2}$ where τ is the relaxation time.

Therefore Z is given as;

$$Z = \frac{S^2\sigma}{\kappa_e + \kappa_{ph}} \tag{8}$$

$$Z_{3D}T = \frac{\frac{3}{2}\left(\frac{5F_{3/2}}{3F_{1/2}} - \zeta^*\right)^2 F_{1/2}}{\frac{1}{B} + \frac{7}{2}F_{5/2} - \frac{25F_{3/2}^2}{6F_{1/2}}} \tag{9}$$

This calculation does not take degeneracy into account.

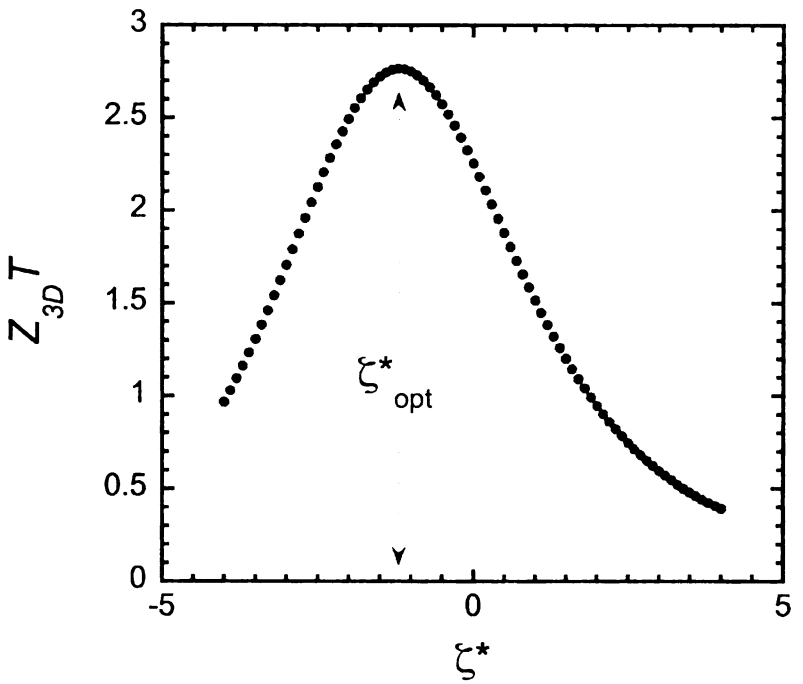

Figure 4: $Z_{3D}T$ versus reduced chemical potential. This plot shows the optimal chemical potential for a certain *B* factor Value to give a maximum Z3DT.

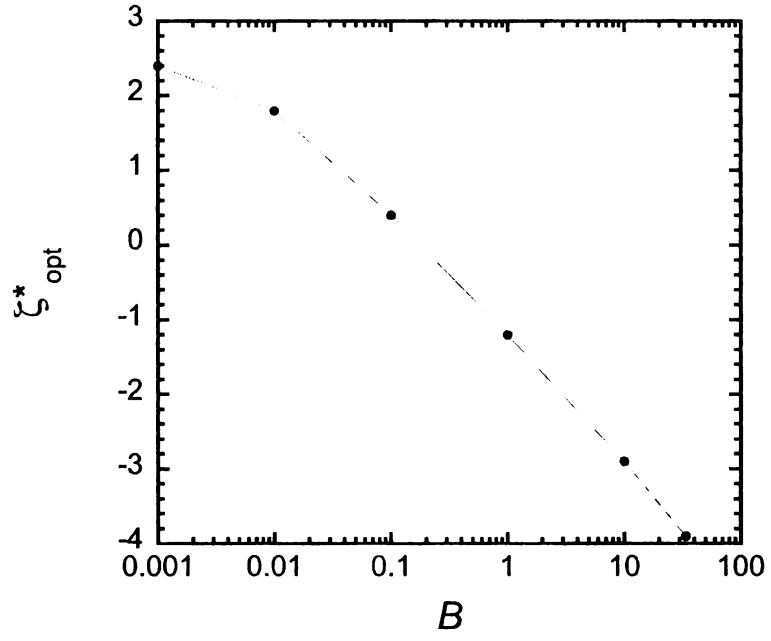

Figure 5: Reduced chemical potential as a function of the B factor.

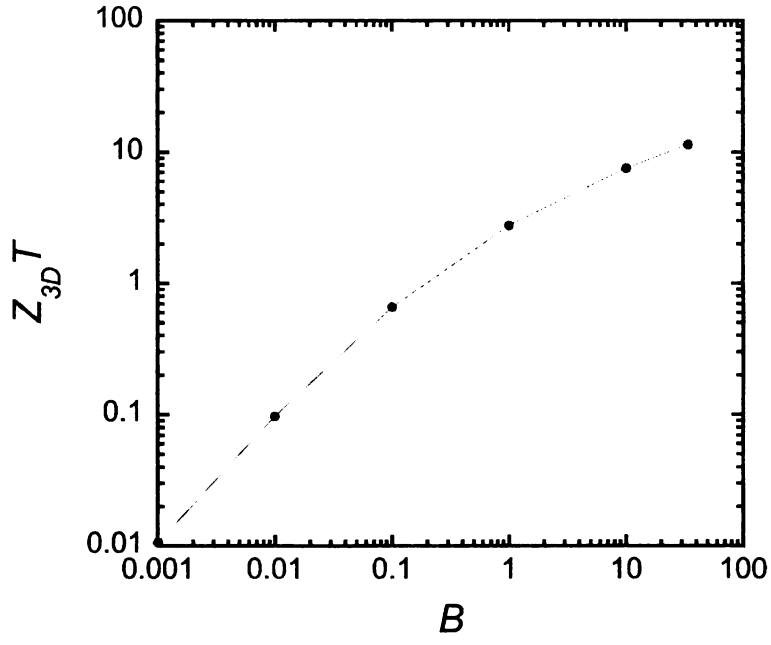

Figure 6: Plot of $Z_{3D}T$ as a function of the B factor at optimal reduced chemical potential.

A proposed method to increase of ZT in some materials is by preparing them in the form of a multilayered super lattice [11]. These structures will increase Z due to the fact that the electrons are now confined to move in two dimensions. This also may reduce the phonon thermal conductivity and therefore increase Z with the interface scattering of the phonons.

For the 2D case the energy band functions are as follows;

$$E(k_x,k_y)=\frac{\hbar^2 k_x^2}{2m_x}+\frac{\hbar^2 k_y^2}{2m_y}+\frac{\hbar^2\pi^2}{2m_z a^2} \tag{10}$$

The electrical conductivity, thermopower and the electronic contribution to the thermal conductivity are;

$$\sigma=\frac{1}{2\pi a}\left(\frac{2k_BT}{\hbar^2}\right)^{3/2}(m_xm_y)^{1/2}F_0q_e\mu_x \tag{11}$$

$$S=-\frac{k_B}{q_e}\left(\frac{2F_1}{F_0}-\zeta^*\right) \tag{12}$$

$$\kappa_e=\frac{\pi\hbar^2}{4\pi a}\left(\frac{2k_BT}{\hbar^2}\right)^{5/2}\left(\frac{m_y}{m_x}\right)^{1/2}k_B\left(3F_2-\frac{4F_1^2}{F_0}\right) \tag{13}$$

The reduced chemical potential in the 2D case is;

$$\zeta^*=\left(\zeta-\frac{\hbar^2\pi^2}{2m_za^2}\right)\Big/k_BT \tag{14}$$

$$Z_{2D}T=\frac{\left(\frac{2F_1}{F_0}-\zeta^*\right)^2F_0}{\frac{1}{B}+3F_2-\frac{4F_1^2}{F_0}} \tag{15}$$

$$\Rightarrow B' = \frac{1}{2\pi a}\left(\frac{2k_B T}{h^2}\right)\sqrt{m_x m_y}\,\frac{k_B^2 T}{q\kappa_{ph}}\mu_x \qquad (16)$$

The reduced chemical potential now can be varied by both doping and changing the layer *a* of the quantum well structure. Recall that in the 3D case, the only means to increase *B* in an anisotropic crystal is to choose the current direction to be the direction of the highest mobility. The situation is more complex for the 2D quantum well. $Z_{2D}T$ not only can be optimized by choosing the best current direction, but also by narrowing layers and choosing the best orientation to make the layers. A layer thickness of 10Å is optimal for Bi2Te3 materials.

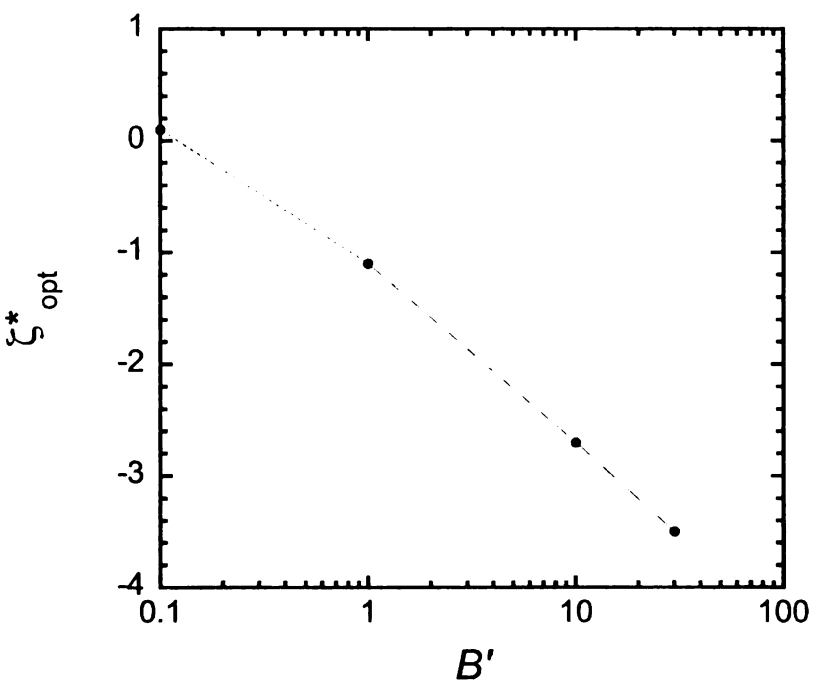

Figure 7: *B'* vs. the optimal chemical potential.

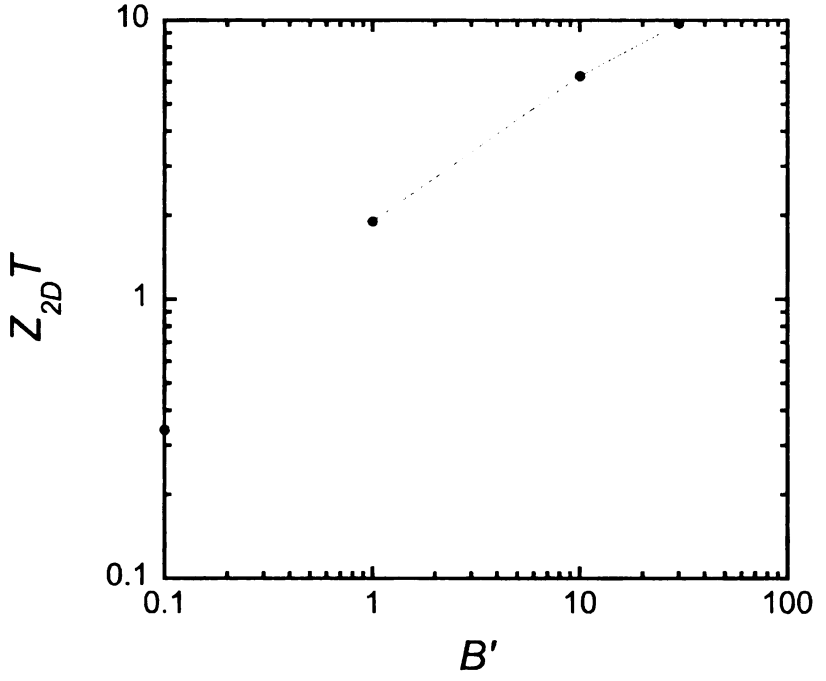

Figure 8: $Z_{2D}T$ as a function of B'.

2.4 Large Z value Contributions

Materials with a large effective mass, high carrier mobility, and low lattice thermal conductivity will yield high Z values. Semiconductors with an energy gap of $10k_BT$ is good for an efficient thermoelectric, $\beta E_g \sim 10$ [12].

Table 2: Table of Energy Band gap and βE_g values for typical thermoelectric materials.

Material	E_g(eV)	Temp of Operation (K)	E_g/k_bT
Bi_2Te_3	0.16	300	9.7
PbTe	0.5	650	8.9
$AgSbTe_2$	0.3	650	5.4
GeTe	0.4	700	6.6
SiGe	0.7	1100	7.4

2.5 Electronegativity, Mobility, and Weighted Mobility

As discussed earlier, mobility is a contribution to improving the figure of merit of thermoelectric materials. High mobilities come from direct bandgap semiconductors, but the effective mass is small. A small effective mass will reduce the *B* factor. An indirect band gap material would be ideal for a thermoelectric material.

Goldsmid and Mahan stressed the importance of the weighted mobility [13].

$$U = \mu\left[m^*/m_o\right]^{3/2} \tag{17}$$

The weighted mobility, *U*, is defined by m^*, the effective density of states mass for the conduction band, m_0, the free electron mass, and μ, the mobility. Better thermoelectrics exhibit large weighted mobilities. *U* values of 100 or above are typical for thermoelectrics. Compounds with *U* values of 100 or above typically have an average electronegativity below 0.5. Mobility is high in compounds where there is no charge motion associated with phonons in purely covalent lattice. In compound semiconductors made of two or more elements with differing elecronegativity values there is an electron transfer between the ions. The amount of charge transfer increases with the electronegativity difference. Therefore it key to have low average electronegativities for thermoelectric materials made with multiple elements.

Table 3: *U* values and electronegativity differences for some thermoelectric materials.

	U value ($cm^2/V•sec$)		Electronegativity Difference (ΔX)
	n-type	p-type	
PbTe	200	79	0.53
Bi_2Te_3	406	608	0.38

2.6 Bi_2Te_3 [14]

Bismuth Telluride, and its alloys exhibit the best *ZT* near room temperature. Bismuth telluride's melting point is 585°C. When the percentage composition of tellurium exceeds 62.5%, it goes from being a p-type material to n-type material. Bismuth telluride is usually alloyed with Sb_2Te_3, which has the same crystal structure. There is a S_1 alloy, $Bi_8Sb_{32}Te_{60}$, and a S_2 alloy, $Bi_{10}Sb_{30}Te_{60}$. The S_1 alloy has no ZT change if transport is measured parallel or perpendicular to the cleavage plane. This is not the case for the S_2 alloy, which has a higher ZT on the plane parallel to the cleavagee plane. The n-type solid solution optimal figure of merit carrier concentration is $2x10^{19}cm^{-3}$. The p-type solid solution optimal figure of merit carrier concentration is $4x10^{19}cm^{-3}$. The alloying of the bismuth telluride to the antimony telluride can reduce the room temperature thermal conductivity as low as 1W/m•K. The low thermal conductivity is the main contribution for it high *ZT*. Bismuth telluride's both n-type and p-type materials have equally good

thermoelectric properties. Its crystal structure is considered to be rhombohedric, but it is easier to represent it as a layered crystal with hexagonal symmetry. Both the conduction and valance bands have six equivalent minima. The energy bands are nonparabolic, and the effective masses are temperature dependent. The band gap for undoped Bi_2Te_3 is 0.16eV.

2.7 IV-VI Semiconductors (PbTe) [15]

Group IV-VI semiconductors all have a NaCl crystal structure. PbTe has a maximum *ZT* around 700K. The room temperature band gap is 0.31eV. The standard alloy for lead telluride is $Pb_{1-x}Sn_xTe$. With x >0.25 there is a ferroelectric transition of the alloy at 100K, which is a spontaneous electric polarization of a material. The composition with the highest figure of merit is when x=0.25. Lead telluride's *ZT* exceeds 1 at 800K. The use of a few tenths of 1% of sodium can make p-type lead telluride. Lead telluride is the base composition of the LAST materials.

2.8 SiGe [16,17]

Silicon has one of the highest weighted mobilities at room temperature, however is also has a large value of thermal conductivity, 100W/m•K at room temperature, which decreases with increasing temperature. It was then later discovered that alloying silicon with germanium decreases the thermal conductivity by a large amount. SiGe's minimum resistivity is at 1100K, which is also the point of its maximum *ZT*. Silicon germanium ingots are fabricated by zone

leveling, which is time consuming, or by hot pressing. The highest *ZT* mixture is $Si_{0.7}Ge_{0.3}$ and boron and phosphorus are used for doping.

It was first used in space for the SNAP-10A nuclear reactor, and has been the preferred space born thermoelectric since 1976. Silicon germanium operates at temperatures up to 1300K for years without degradation of its properties. It has accumulated over 250 million device hours without a single known failure.

With silicon germaniums high operating temperatures, thermal expansion issues, Silicon germanium is 3-4 times stronger in compression than in tension. Therefore contact materials should have a larger CTE than Si-Ge.

2.9 Bismuth Antimony [18,19]

Bismuth antimony is a semimetal with a rhombohedral structure and a carrier concentration of $10^{18}cm^{-3}$. It has six electron ellipsoids and is a multivalley material. Alloying bismuth antimony with group IV materials will add donors or acceptors, and modify the band structure. Alloying with group V materials can modify the band structure and change the carrier concentration. The *ZT* is 0.6 at room temperature with around 10-15% antimony.

2.10 Skutterudites [20-23]

Skutterudites are a natural occurring material that was first discovered in Skutterud, Norway. It has a cubic crystal structure with 32 atoms per unit cell. The atoms are arranged in an open, cage like structure. Atoms can be placed inside these cages to reduce the thermal conductivity.

Skutterudites meet the basic conditions for a high *ZT*. They have a large unit cell, heavy constituent atom masses, a low electronegativity difference between atoms, and have the highest reported mobilities among all know materials. Filling the voids in the cage like structures has been the focus of efforts to improve the thermoelectric properties. Lanthanum, cerium, and thallium partially filled skutterudites have been reported to possess relatively good electronic properties while also possessing much lower thermal conductivites than the unfilled cages of $CoSb_3$.

2.11 Clathrates [24,25]

Transport properties of semiconductor type-I Si and Ge clathrates reveal low thermal conductivity values along with relatively high Seebeck coefficients and electrical conductivity. The crystal structure of these clathrate compounds consists of a framework of group-IV atoms having several polyhedral cages, each of which can incorporate relatively large guest atoms, not unlike skutterudites. Thermal conductivities of these crystalline compounds are similar in temperature dependences and magnitudes to that of amorphous materials. The experimental trends in thermal conductivity are similar to those found in skutterudites. These are semiconductors with good electron properties that can be synthesized with a glasslike thermal conductance.

Group IV elements can also form clathrates of type X_8E_{26}, where E represents a group IV element and X represents an atom in the voids formed by

elements E. The X atoms do not enter the lattice substitutionally but are interstitial, residing inside the oversize cage.

2.12 Half-Heusler Alloys [26]

Half-Heusler alloys have a MNiSn composition where M is a group IV transition metal (Hf, Zr, or Ti). The alloys have a band gap of 0.1-0.5eV. Room temperature values of power factor are comparably to that of Bi_2Te_3, however the room temperature thermal conductivity is approximatley 10 W/m•K. They have a MgAgAs type crystal structure, forming three interpenetrating face centered cubic sublattices with one Ni sublattice vacant.

2.13 TAGS [27]

TAGS is GeTe alloyed with 10-20% $AgSbTe_2$. TAGS has a very low lattice thermal conductivity. The two most well known TAGS compounds are called TAGS-80 and TAGS-85. The number represents the percentage of GeTe. TAGS-80 has a ZT of 1.85 at 800K. TAGS-85 has a ZT of 1.35 at 800K. TAGS has been used in numerous space applications, for example pioneer 10 and 11.

2.14 Quantum Well, Supperlattice Materials [28,29,30]

As discussed earlier, supperlattice (SL) materials are phonon blocking/electron transmitting superlattices. Structures utilize the acoustic mismatch between the superlattice components to reduce the lattice thermal conductivity, rather than using the alloying approach which can scatter carriers as well as phonons. Layers as thick as 10Å offer significantly higher in-plane carrier

mobilities parallel to the superlattice interfaces, than alloys, due to the near absence of alloy scattering and random interface carrier scattering.

P-type Bi_2Te_3/Sb_2Te_3 SL structure have a ZT of 2.4 with a 32.2K gradient across the module. The enhancement achieved by controlling the transport of phonons and electrons in the superlattice. The thickness of the heterojunction layers influences the mobility of the samples.

A type one quantum well (QW) is a semiconductor with a narrow banggap sandwiched between two materials with larger band gaps. Impurities are put in the barrier materials so the conducting layer is free of impurities, unlike in bulk materials where impurities cause scattering. These devices have promising applications but are very expensive and difficult to fabricate.

2.15 Quantum Dots [31]

Quantum dot supperlattice structures have a delta function distribution of the density of states, and discrete energy levels due to three-dimensional quantum confinement. This is a more favorable carrier scattering mechanism, and a much lower lattice thermal conductivity. Devices have been grown by molecular beam epitaxy, with compositions of PbSeTe/PbTe.

2.16 Electrical Conductivity

The electrical conductivity has a direct relation to the dopant concentration of a semiconductor material.

$$\sigma = q(\mu_n \cdot n + \mu_p \cdot p) \tag{18}$$

In the above equation, *n* and *p* are the dopant concentrations of a semiconductor material. The concentration of dopants in LAST materials is around 10^{19} cm^6. At this concentration, the sample is degenerately doped and shows metallic temperature dependence for the electrical conductivity (decreasing σ with increasing temperature). We have experimentally found electrical conductivity values in the range of 800 to1500 $S \cdot cm^{-1}$ to correspond to some of the highest *ZT* samples for the LAST and LASTT materials we are investigating.

2.17 Thermopower, Mott Equation

The thermopower of a device, or also known as the absolute Seebeck coefficient is the open circuit voltage of a semiconductor under the influence of a temperature gradient. The thermopower of a material is a measure of the local entropy, and is influenced by effective masses and the energy dependence of the density of states. For LAST materials we have experimentally found values near $100 \mu V \cdot K^{-1}$ at room temperature tend to yield the highest *ZT* materials. When adjusting the composition and doping of LAST, a reduction in the carrier concentration causes an increase in the thermopower, however also corresponds to a decrease in the electrical conductivity.

$$S = \frac{\pi^2 k^2 T}{3e} \cdot \frac{d \ln \sigma(E)}{dE}\bigg|_{E=E_f} \tag{19}$$

The equation above is the Boltzmann transport theory equation for thermopower, the Mott equation [32]. The electrical conductivity in the equation is a function of the Fermi energy. The thermal power is a measure of the asymmetry in electronic

structure and scattering rates near the Fermi level, finding materials with electrical conductivities that have strong asymmetrical energy dependence in a small energy interval near E_f is a way to approach high thermopower. This has lead to searching for materials with complex structures and compositions. Fabricating materials with 2D, 1D, and 0D structures of the density of states give a large value in $d\ln\sigma(E)/dE$.

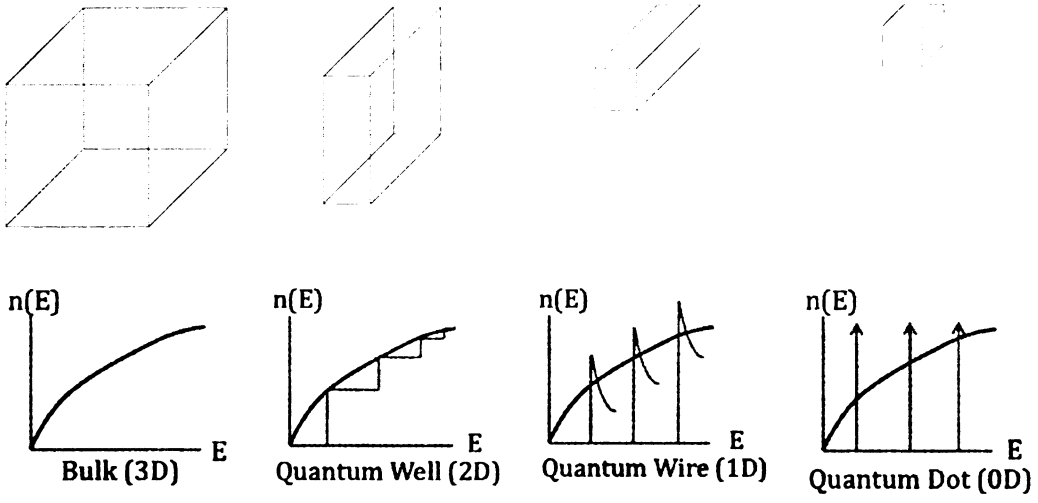

Figure 9: Models of the density of states for different dimensionalities.

2.18 Thermal Conductivity

The thermal conductivity is the measurement of a materials ability to conduct heat. From the *ZT* equation it can be seen that a low thermal conductivity material helps to increase the figure of merit. For the materials studied in this thesis, a thermal conductivity near $1 W \cdot m^{-1} \cdot K^{-1}$ is commonly seen for the high *ZT* samples. There are two contributions to thermal conductivity.

$$\kappa = \kappa_e + \kappa_l \tag{20}$$

The first part is the electronic contribution and the second part is the lattice (or phonon) contribution to the thermal conductivity. For metals, the electronic contribution to the thermal conductivity was found to obey the Weidemann-Franz law

$$\kappa_e = L \cdot \sigma \cdot T \tag{21}$$

where L is the Lorentz number, σ is the electrical conductivity of the material, and T is the temperature. This indicates that a trade off between high electrical conductivity and low thermal conductivity must be considered for optimizing the ZT of a sample.

The lattice thermal conductivity can also be adjusted through mass fluctuations within the crystal lattice. This can be accomplished through the choice of multielement semiconductor materials containing high and low mass elements, and through alloying of materials. More recently, the prediction of ZT enhancements through quantum confinement [33] has led to thin film materials that exhibit high ZT values primarily through a significant reduction in thermal conductivity [34]. The LAST and LASTT bulk materials developed by the Kanatzidis group at Michigan State University and Northwestern University also exhibit endotaxially imbedded nanostructures which form during ingot growth through a spinodal decomposition mechanism [6]. These nanostructures are believed to reduce electron-phonon interaction by preferentially scattering phonons while allowing electrons to flow through them.

2.19 Contact Resistance

Contact resistance reduction is crucial for building an efficient thermoelectric power generation module. The contact resistance is measured at the interface of two dissimilar materials which electrical current is passing through. Thermoelectric devices have a semiconductor-metal interface where a detrimental non-ohmic behavior can arise from the Schottky effect. Thermoelectric power generation devices are linear and reversible devices, therefore low resistance ohmic contacts are desired. The losses due to Joule heating at the contacts is a non-reversible energy loss component that reduces the overall efficiency of the device as shown in the equations below.

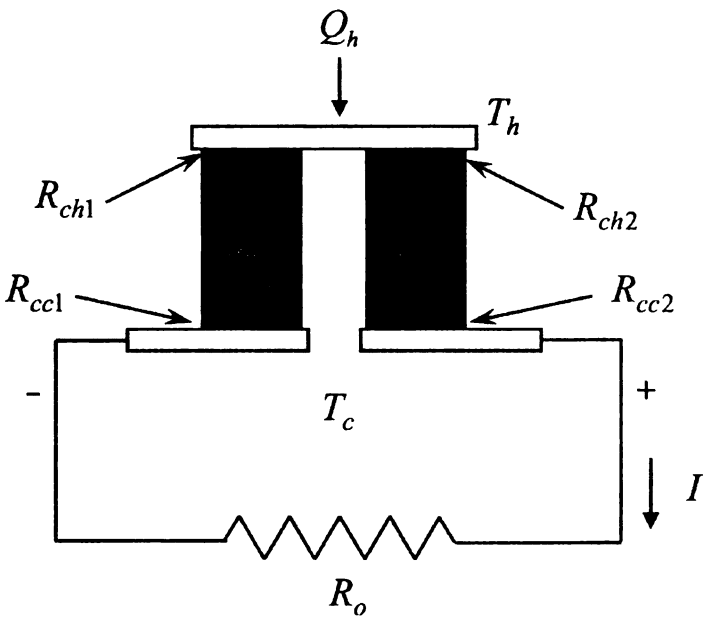

Figure 10: Thermoelectric module power generation circuit.

$$\eta = \frac{P_O}{Q_h} \qquad (22),$$

Equation (6) is the thermoelectric efficiency of a module.

$$P_O = I^2 R_O \tag{23},$$

P_O is the electrical output.

$$Q_h = K\Delta T + ST_h I - \frac{1}{2} I^2 (R + R_C) \tag{24},$$

Q_h is the heat input into a thermoelectric device.

$$\eta_C = \frac{\Delta T}{T_h} \tag{25},$$

Equation (5) is the equation for carnot efficiency.

$$\mu = \sqrt{(1+\delta)^2 + (1+\delta) Z T_{av}} \tag{26},$$

where

$$\delta = \frac{R_C}{R} = \frac{R_{cc1} + R_{cc2} + R_{ch1} + R_{ch2}}{R_n + R_p} \tag{27}.$$

And the complete module efficiency becomes [35],

$$\eta = \frac{\mu \eta_C}{\frac{(\mu+1+\delta)^2}{ZT_h} + (\mu+1+\delta) - \frac{(1+\delta)\eta_C}{2}} \tag{28}.$$

Figure 11 shows plots of the relationship between ZT and module efficiency at different values of δ. The values for δ for fabrication of a efficient (~20%) thermoelectric devices is between 0.0 and 0.1.

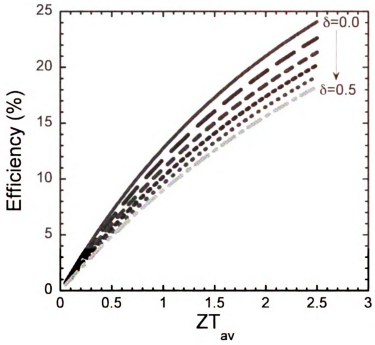

Figure 11: Efficiency degradation due to contact resistance [36].

The purpose of this project is to develop a method of making electrical contacts that have low contact resistance and are mechanically strong.

2.20 Measuring Contact Resistance

After bonding runs, a measure of the contact resistance is needed to determine how well the contact material bonds to the LAST materials. A room temperature scanning probe was built to do a voltage scan across the contact.

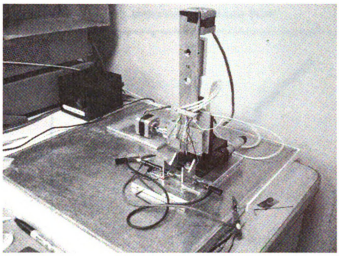

Figure 12: Room temperature scanning probe.

A discontinuity in slope of the voltage across the junction indicates significant contact resistance. For the power generation devices investigated in this study we wish to have a voltage drop across all contacts which is less than one tenth of the voltage drop across the full length of the thermoelectric leg. The room temperature scanning probe is a quick and accurate way to determine the quality of a contact material.

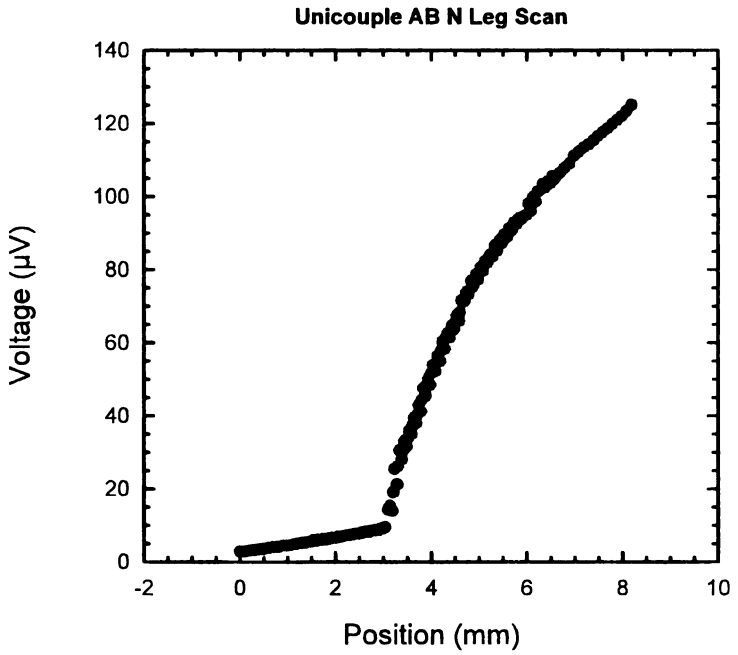

Figure 13: N leg thermoelectric to 316 stainless steel scan.

As shown in Figure 13 LAST to 316 stainless steel show room temperature contact resistivities below $20\mu\Omega\bullet cm^2$ which corresponds to less than a 9μV drop across the junction for these samples. The 316 stainless has a well matched coefficient of thermal expansion to that of LAST, which will reduce thermal stresses during high temperature operation.

The contact resistance can change as a function of temperature, and is therefore of interest to measure contact resistivities as a function of temperature [37]. A system is presently being assembled by my colleague, Muhammad Farhan for temperature dependent measurements of the contact resistances.

3.0 Ultra High Temperature Measurement System (UHT)

Measurements of the thermoelectric properties must be done at the operating temperatures of these devices. Typical thermoelectric power generation modules operate anywhere from 300K to 1000K. Systems described in the literature for characterization of thermoelectric materials commonly utilize the four probe measurement configuration to minimize the errors associated with the contacts [38-43]. The system designed in our lab also utilizes the four probe configuration in a manner that allows for simultaneous electrical conductivity and thermopower measurements and has the capability of measurements from room temperature to 1000°C. Accuracy of the system was evaluated by using a reference platinum wire.

3.1 Experimental Setup [44]

The high temperature system is made up of four main components; furnace, computer, measurement stage, and a vacuum pump. For uniform sample heating, a 1200ºC split tube furnace with a 2 foot long heating zone was used. With such a large furnace capacity, the maximum natural drift cooling rate is less than 2°C per minute. The slow cooling rate allows for accurate measurements of the thermopower and electrical conductivity from high temperatures (~800-900K) back down to room temperature. The ProboStat^{TM} measurement platform and wiring terminal is a purchased item from NorECs. Platinum wiring is used due to the fact that it remains stable in inert or non-inert atmospheres [45], and type S thermocouples are used. The base of the system remains at room temperature to allow for solder connections of all electrical leads needed for measurement. The

voltages measured for thermopower and electrical conductivity are in the nano to microvolt range. For measuring these voltages, Keithley 2182 nanovolt meters are used. Currents are sourced with a Keithley 2400 source meter. The measurements of electrical conductivity and thermopower needs three 2182 meters. A Varian dry scroll and turbo pump is used to pump the system down to pressures below 20μTorr. The system is for measuring bulk samples only. The minimum sample dimensions are on the order of 2x2x2mm.

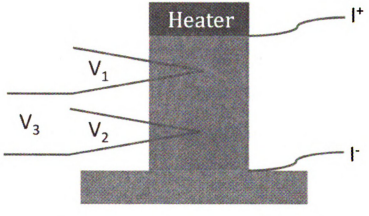

Figure 14: Sample with mounting configuration.

As shown in Figure 14, two thermocouples, a heater and two currents leads are attached to the sample for measurement. The diameter of the platinum wire used is .003 inches, which was found to be the smallest diameter that could be easily handled.

3.2 System Characterization

To test the accuracy of the system platinum was used. The data was compared to NIST data of platinum.

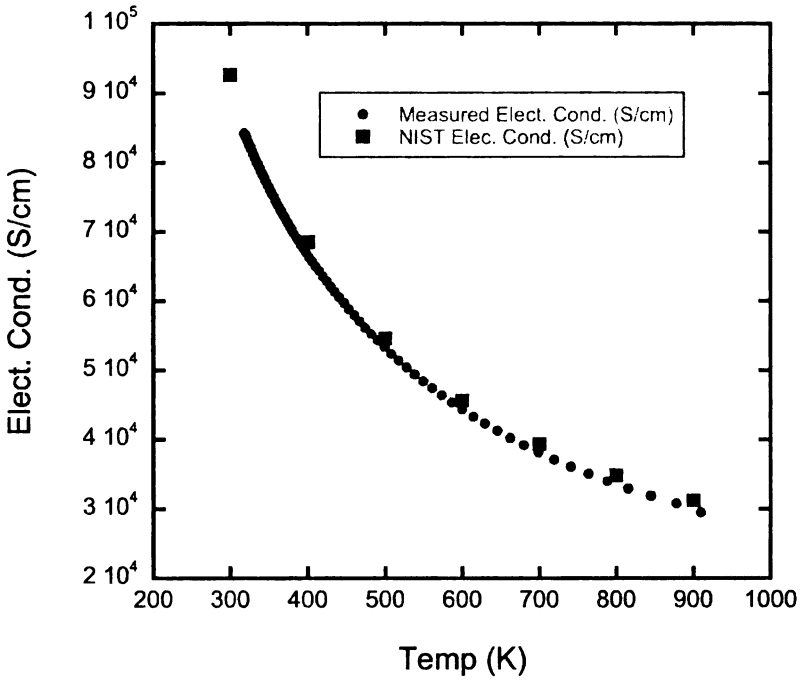

Figure 15: Comparison of NIST data and system-measured data.

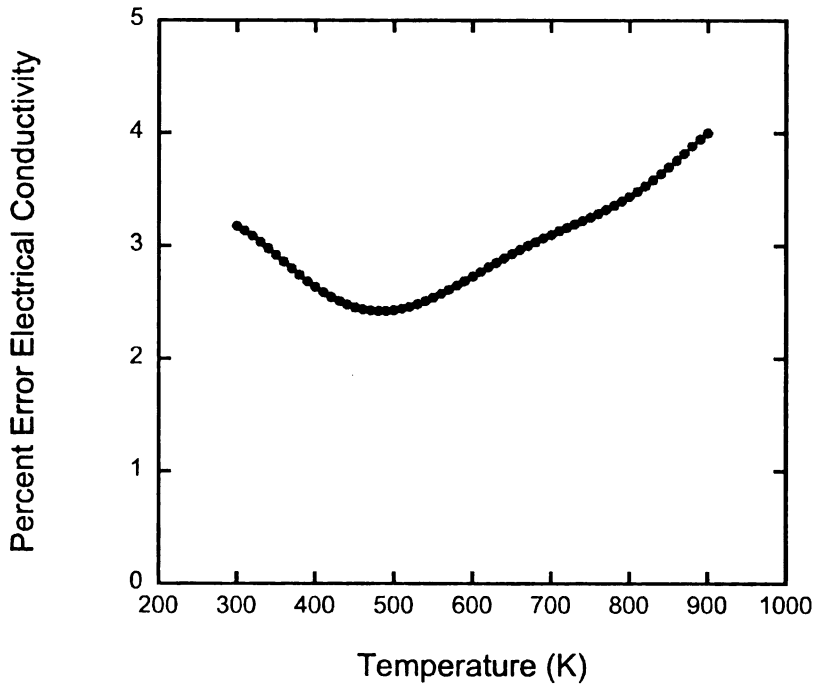

Figure 16: Percent error from NIST data and measured data of electrical conductivity.

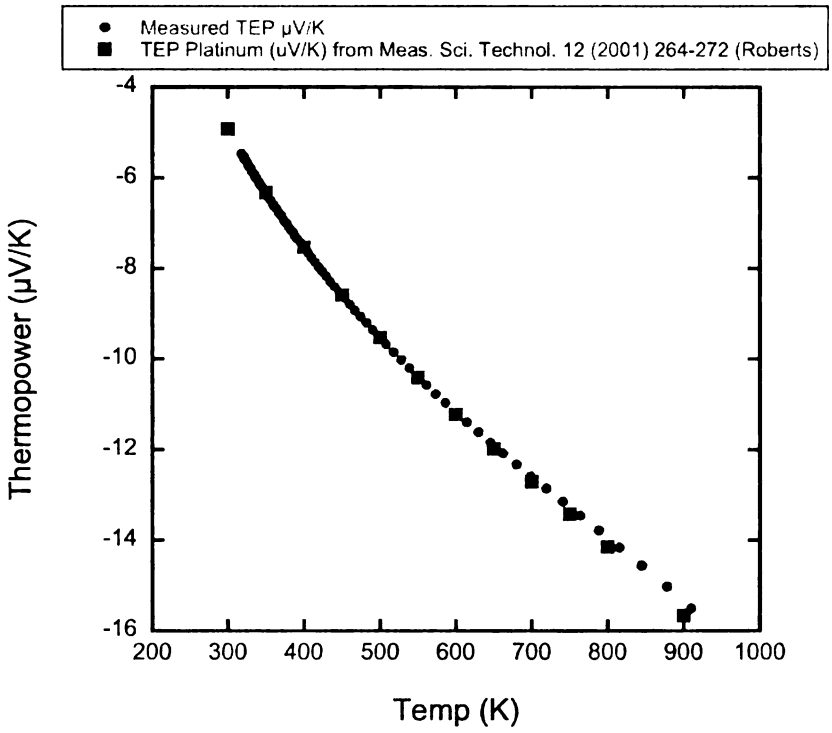

Figure 17: Measured thermopower and reference thermopower of platinum.

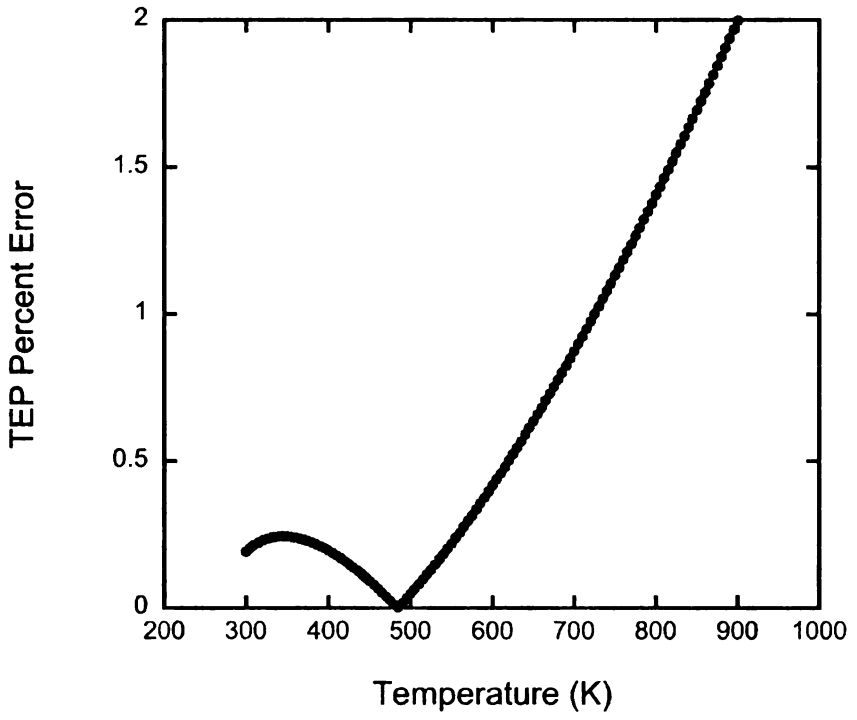

Figure 18: Percent error between measured and reference thermopower.

The percent error for both the thermopower and electrical conductivity is below four percent over the 300K to 900K temperature range.

3.3 N-Type Material Annealing Experiment

The alloys of lead, tellurium, silver, and antimony (LAST) are proven excellent thermoelectric materials for temperatures ranging from room temperature to 800K [46,47]. The material is either used as cast or hot pressed. Ingots of LAST are cast in a quartz tube and then machined into thermoelectric legs for use in fabrication of thermoelectric power generation modules. Annealing of these materials may improve the properties of the LAST material. Properties such as electrical conductivity (S/cm) and thermoelectric power (μV/K) are improved. Annealing of thermoelectric materials is a quite prevalent technique. Some

examples found in the literature include long thermal anneals at temperatures of 800-850°C that were used to obtain β-$FeSi_2$ phase from the metallic α-$FeSi_2$ phase [48]. The samples were cut and annealed in a quartz ampoule filled with argon gas. A comparison of as grown and annealed samples of $Ba_8Au_xSi_{46-x}$ was done to show a chemical composition variation [49]. Annealing was used to improve the thermal stability of the thermoelectric material Zn_4Sb_3, and healed certain defects and surface states, which were created either during the synthesis or with the removal of elemental zinc [50]. Thermal investigation revealed an enhanced heat capacity for nc-Zn_4Sb_3, which could be reduced to the bulk value of Zn_4Sb_3 by annealing at 190°C. Cold compacted and sintered $Pb_{1-x}Sn_xTe$ samples were examined for their annealing effects [51]. Annealing of these materials under controlled pressures of Te and Pb can be used to change the carrier concentration. The carrier concentration can be varied by changing the annealing temperature, on account of the variations of the solubility limits of the Te and Pb with temperature. For this study, the sample's thermoelectric properties were measured before and after annealing to compare property changes.

To investigate annealing effects, a sample from an n-type ingot, ETN207was prepared for measurement. The room temperature electrical conductivity before the measurement was 147.4 (S/cm).

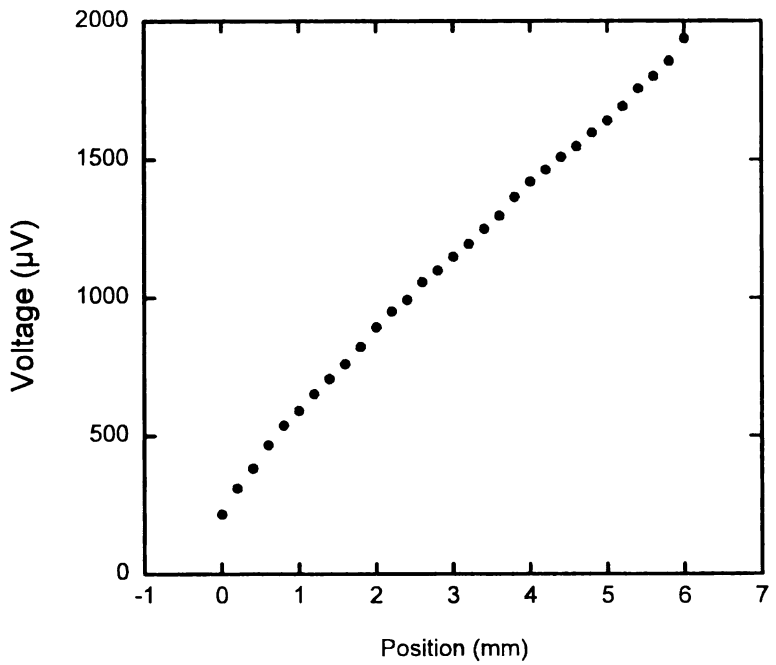

Figure 19: ETN207 sample 1 before the high temperature measurement, electrical conductivity scan.

The sample was first taken to 400K and cooled to let the silver paste contacts cure. The probe separation was then adjusted so the room temperature conductivity matched the room temperature scanning probe electrical conductivity. It is assumed that the sample does not change when cycling to 400K. The sample was then cycled three times to 700K and back to room temperature. Twice the sample was held at 700K to see if the sample would anneal. A typical result of an annealed sample is that the conductivity of the sample will increase while the thermopower would remain the same. This sample however had a conductivity that decreased and an increase in the thermopower.

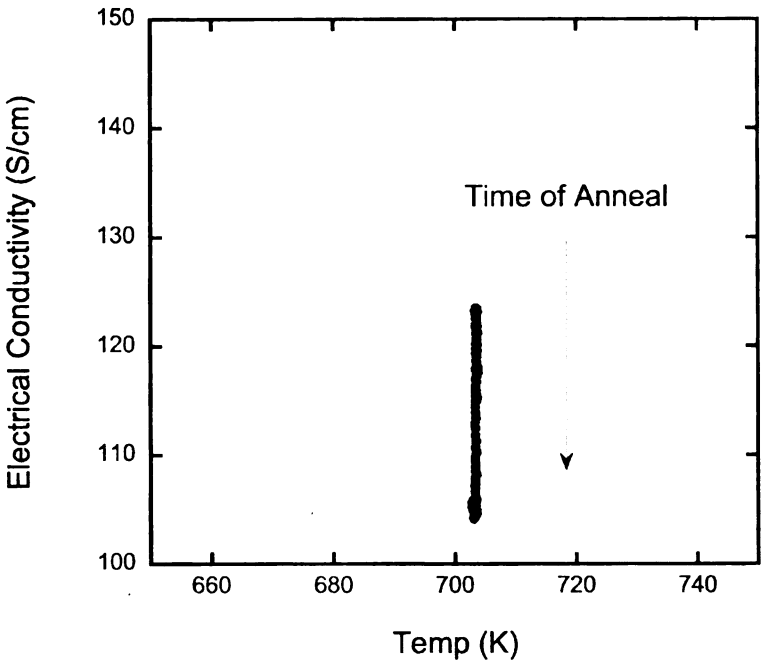

Figure 20: Electrical conductivity anneal at 700K.

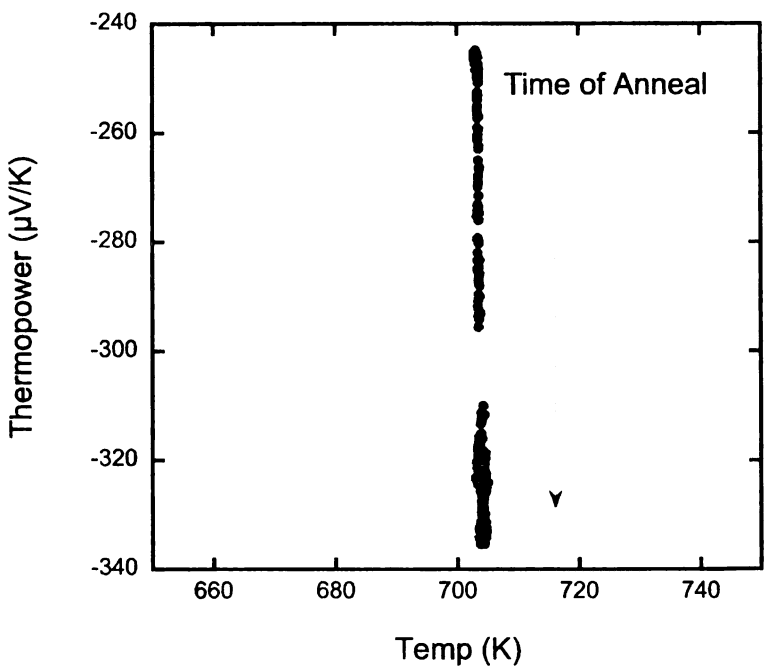

Figure 21: Thermopower anneal at 700K.

The sample was removed from the measurement system and there was a noticeable coating on the outside of the sample. This coating suggests that there was an outgassing or evaporation of material during the measurement run.

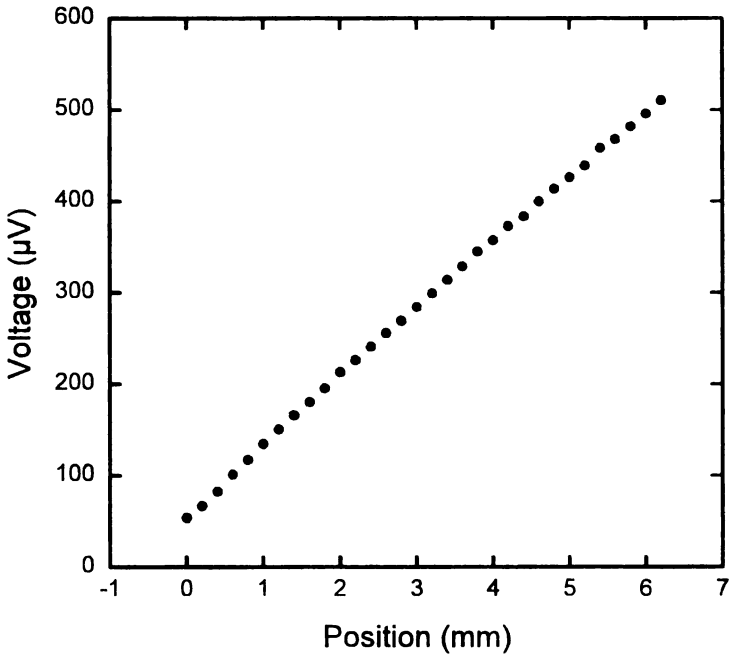

Figure 22: Scan of ETN207 after temperature cycling and measurement of thermoelectric properties. RT σ=544.68 (S/cm).

The sample properties changing during the temperature cycling was also an issue. Most samples measurements repeat their properties through temperature cycling. Four of the ETN207 were annealed at 423°C for 24 hours under a flow of Ar/H2 gas. These samples were then scanned at room temperature for their electrical conductivity. One of these samples was then used for a temperature dependent run to see how the properties changed as a function of temperature compared to the un-annealed ETN207.

Four samples were annealed at 423°C for 24 hours. The samples were named as follows; ETN207_sample number_annealed temperature. After annealingETN207_1_423 had a room temperature conductivity of 388.68 (S/cm). The sample's conductivity before the anneal was 147 (S/cm). Sample ETN207_1_423 was mounted in the UHT for measurement of its temperature dependent properties. The measurements were taken from room temperature to 700K.

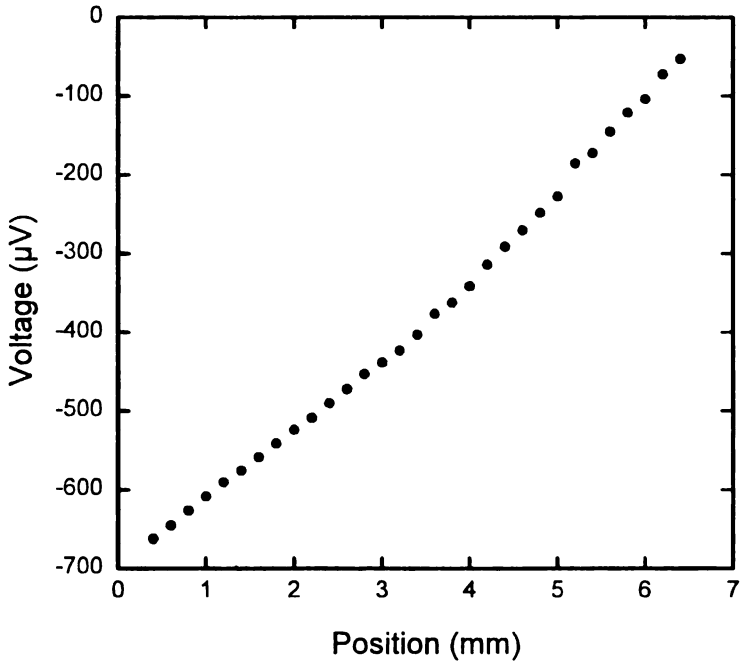

Figure 23: ETN207_1_423 room temperature scan after anneal at 423°C.

Sample ETN207_2_423 showed a large crack about 4.5mm into the sample. Below is a plot of the room temperature scan.

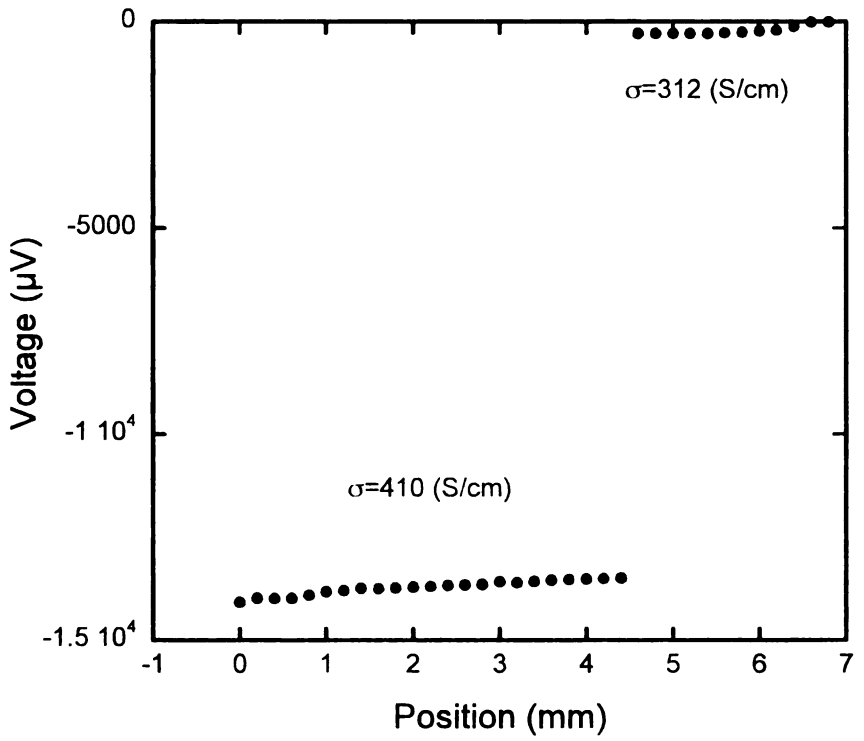

Figure 24: Room temperature electrical conductivity scan of ETN207_2_423. The conductivities of each side of material are shown.

Sample ETN207_3_423 had a room temperature electrical conductivity of 429.24 (S/cm) after the anneal at 423°C.

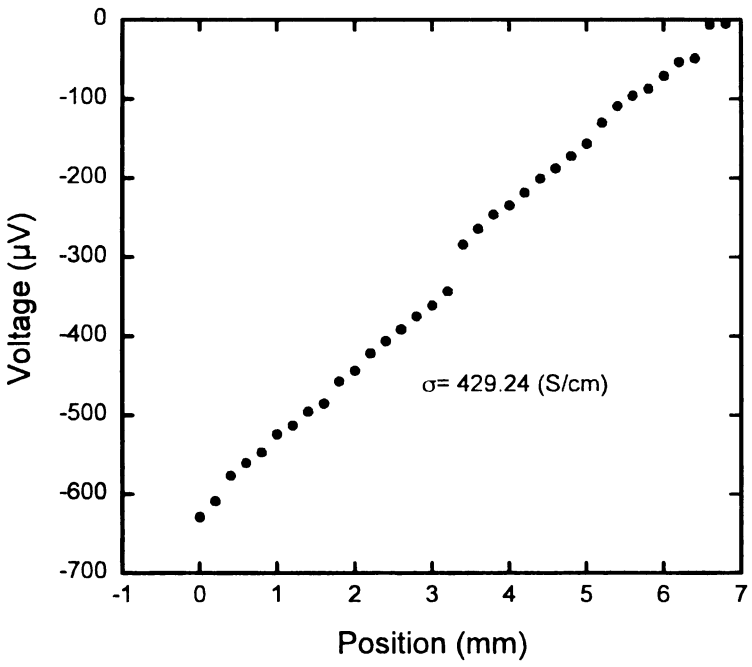

Figure 25: ETN207_3_423 room temperature scan.

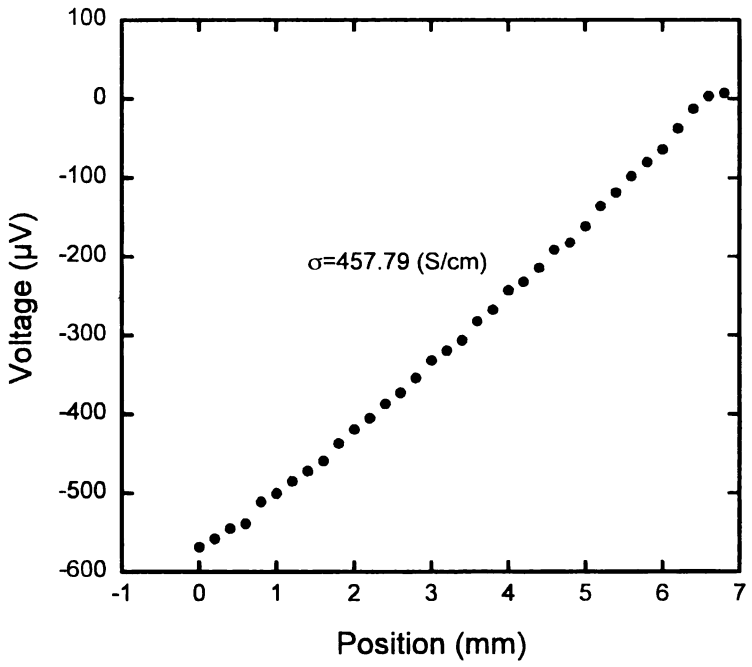

Figure 26: ETN207_4_423.

A second cast sample (ETN207_5_Cast) was measured at room temperature for its electrical conductivity, ETN207_5_CAST.

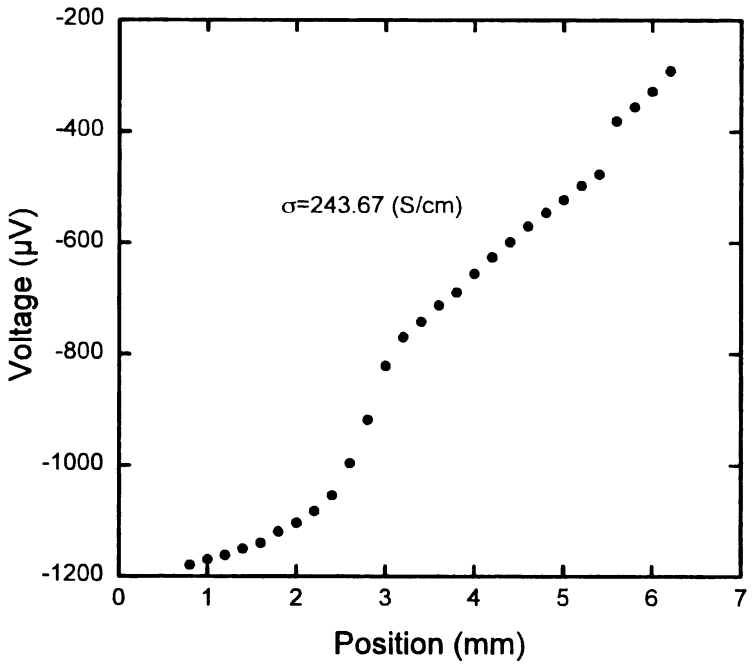

Figure 27: Room temperature scan of ETN207 as cast.

The "as cast" ETN207 had conductivities ranging from 147 to 243 (S/cm). The conductivities of the annealed samples are all around 400 (S/cm).

3.4 Ingot Uniformity

To test the uniformity of an ingot, samples were measured in each "coin" of an ingot. A typical 200-gram ingot is 22mm in diameter and 56mm tall. Seven-millimeter coins were cut from the ingot, and labeled A to D with the A coin corresponding to the top of the vertically cooled ingot. Samples from each coin were measured in the UHT system.

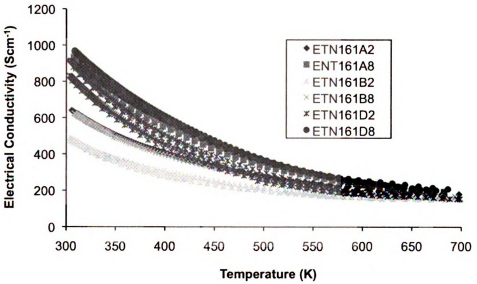

Figure 28: Plot of electrical conductivities of samples measured from each coin.

These samples may have differing compositions or may exhibit cracks. If the compositions were different, the thermopower should also be different. Cracks would show less of a change in the thermopower.

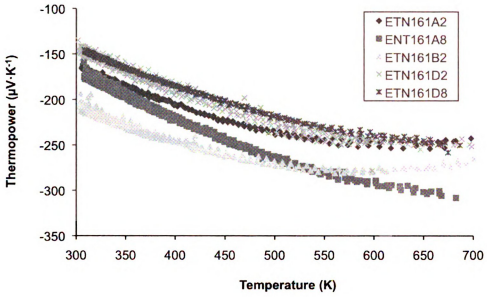

Figure 29: Plot of thermopowers measured from samples of each coin.

ETN161B2 from the B coin has the highest room temperature thermopower. ETN161A8 has the highest thermopower at 700K. Higher thermopower can result from an increase in nanostructuring in this sample, and/or from the doping level in this sample resulting in a Fermi level located in a more rapidly changing portion of the density of states (DOS). For example, a Fermi level located at a peak in the DOS results in a small thermopower since the density of states is symmetrical about the Fermi level, however slightly off from the DOS peak leads to a larger thermopower. This sample may contain nanostructuring that would improve thermopower. As mentioned earlier, nanostructuring would give a low dimensionality energy dependence of the density of states, which in turn leads to a larger thermopower.

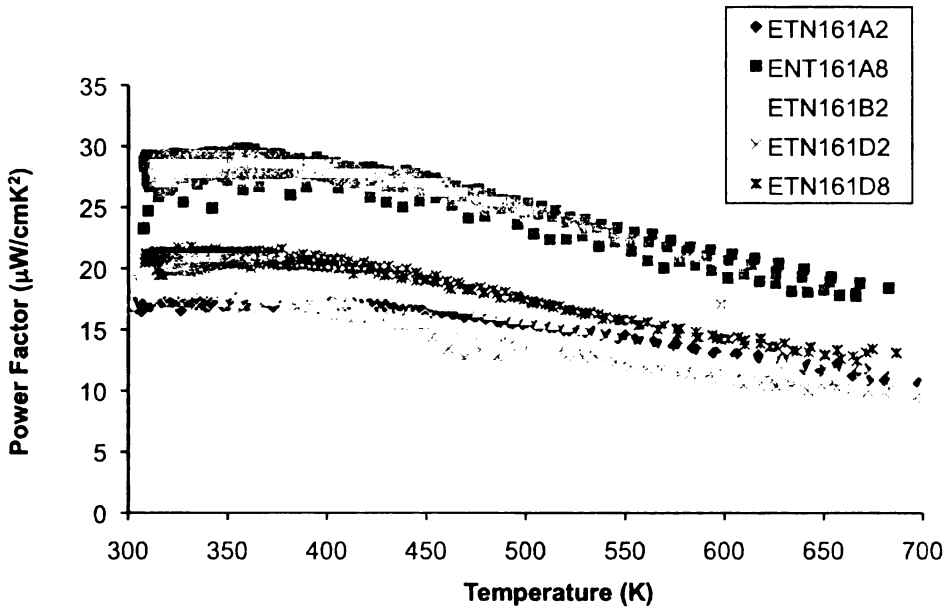

Figure 30: Plot of power factors measured from samples of each coin.

Overall, ETN161A8 has the largest power factor. The rest of the samples lie from 16-20 ($\mu W/cm \cdot K^2$) at 300K and around 10 ($\mu W/cm \cdot K^2$) at 700K. The cast LAST materials show to have similar properties throughout the ingot with one sample having above average properties.

3.5 Hot Pressed UHT Results

A hot pressed material labeled, MSUHP12, was measured in the UHT and exhibited interesting properties with pressure. During pumping, the electrical conductivity of the material increased and when the pressure returns to atmosphere the electrical conductivity returned to a value that was close to its original value.

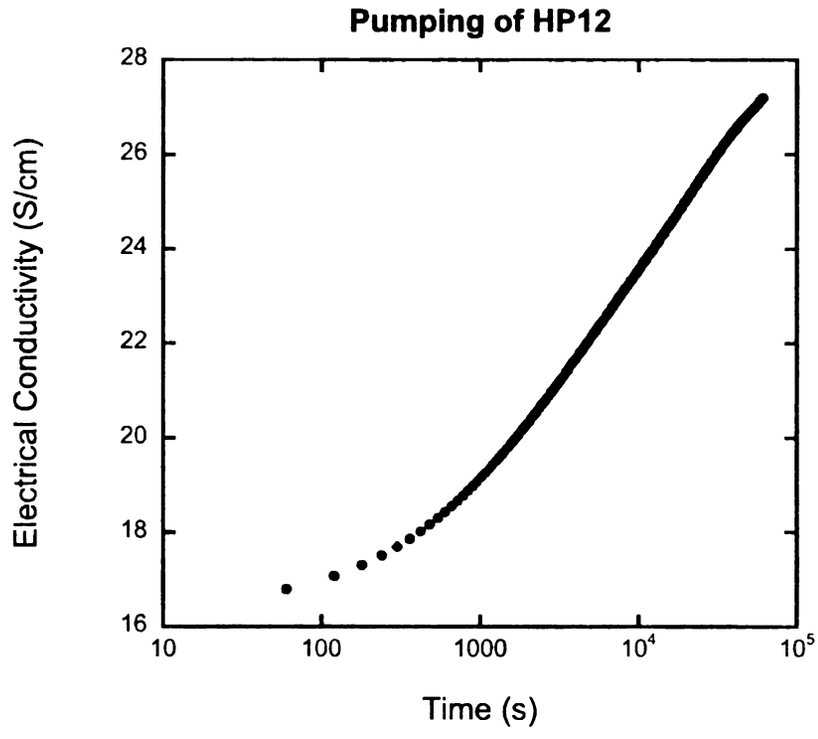

Figure 31: The change in electrical conductivity while pumping down atmosphere.

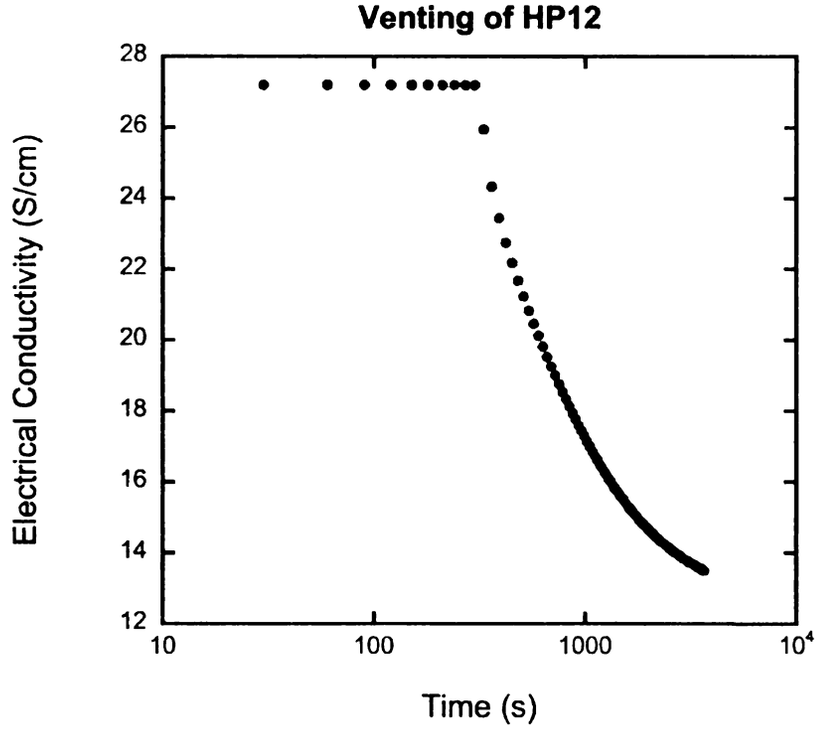

Figure 32: Change in electrical conductivity of HP12 during venting of system.

It is thought that the moisture content may be affecting the electrical properties of the material [52], however other hot pressed samples did not exhibit this pressure dependent effect.

3.6 CAST to Hot Pressed Property Comparison

To compare the properties of a cast sample with the properties of a hot pressed sample, an ingot (ETN191) was measured for its electrical conductivity and thermopower prior to crushing it into powder. It was then hot pressed and both ETN191 and its corresponding pressed MSUHP32-N sample were measured to see how the properties changed before and after pressing.

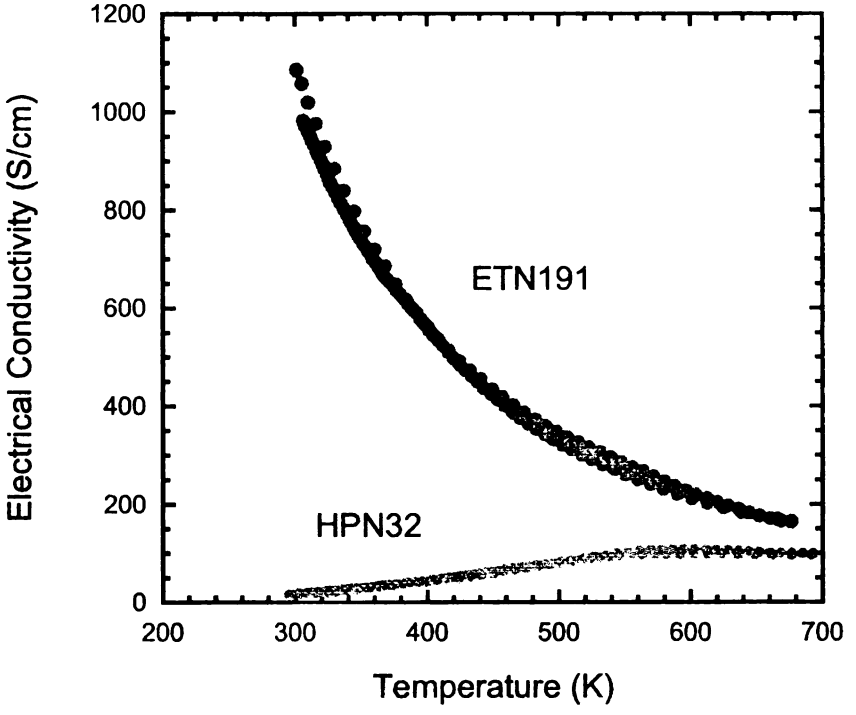

Figure 33: Comparison of electrical conductivity of cast and hot pressed material.

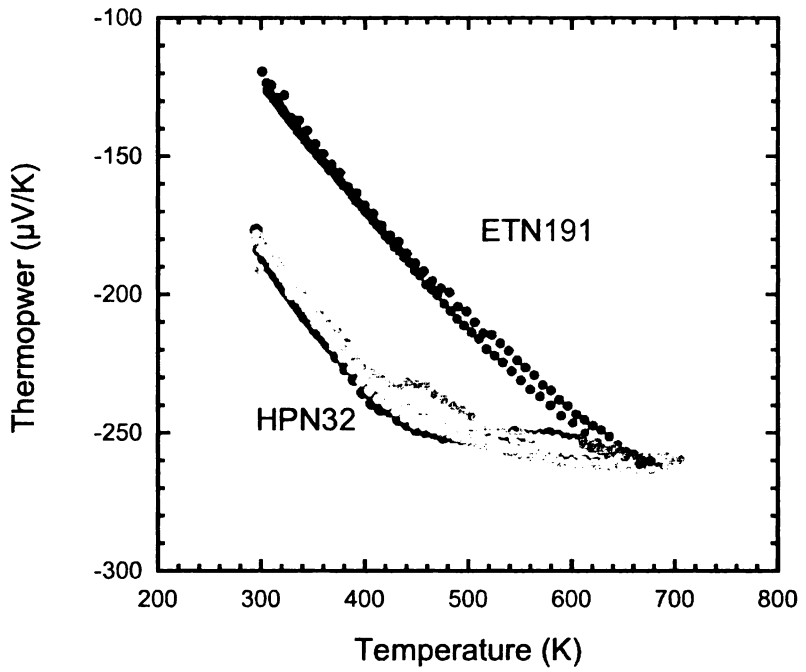

Figure 34: Comparison of thermopower of cast and hot pressed material.

It is typical that the hot pressed materials have a lower room temperature electrical conductivity than the cast materials. The room temperature thermopower did increase for the hot pressed material but then matches the cast material at 700K. The hot pressed material has an overall lower electrical conductivity. The hot pressed materials nearly match the electrical properties of the cast materials at 700K. These results suggest the powder processing steps effectively remove carriers from the LAST material. Defects and/or oxides on the surfaces of the powder particles may cause this. The hot pressed legs may be cascaded with cast materials or hot pressed Bi_2Te_3 for an efficient thermoelectric leg from room

temperature to 700K. As discussed earlier, the hot pressed materials have a higher strength than the LAST and are more uniform in composition.

4.0 Diffusion Bonding

4.1 Diffusion Bonding Introduction

Diffusion bonding is a method of bonding two similar or dissimilar metals, alloys, or nonmetals. This is achieved by pressing together the two materials to be bonded either in vacuum, an inert gas, or a reducing atmosphere, and increasing the temperature until atomic diffusion across the interface bonds the two materials together. Diffusion bonding experiments typically yield the best results in an atmosphere with the least amount of oxygen present. This helps to reduce the amount of oxides present at the interface of the two materials, which tend to degrade the bond. There are many control parameters investigated in these diffusion bonding including; temperature, time, and pressure. The bonding temperature should be 50-80% of the melting point of the more fusible metal [53]. Tamman's rule states that the importance of diffusion is made evident at temperatures about 80 to 90 percent of the absolute melting point of the material considered [54]. (Depending on the physical process that you are considering, diffusion can be very significant at 0.6 of the melting temperature). The temperature aids in the inter-diffusion of the atoms across the interface of the two materials and the deformation of the interface surfaces. The bonding pressure fills voids and pushes out any oxides that may reside on either of the two surfaces. Bonding times are found experimentally and can range from minutes to hours. Some of the criteria for choosing a metal interconnect is one that has a low electrical conductivity, a high thermal conductance, and a well matched coefficient of thermal

expansion to LAST and LASTT. To minimize the stresses induced by bonding, contact materials have been chosen with comparable coefficients of thermal expansion (CTE). Most solid materials expand upon heating.

$$\frac{\Delta l}{l_0} = \alpha_l \Delta T, \tag{29}$$

$$\frac{\Delta V}{V_0} = \alpha_V \Delta T, \tag{30}$$

Equations (29) and (30) show the linear relationship between the CTE, α, and the change in either length or the entire volume of a material [55]. Thermal expansion is the increase in the average distance between atoms. LAST has a coefficient of thermal expansion around 21ppm/K. Choosing a contact material with a similar CTE helps reduce thermal stresses associated with the bonding process.

Many considerations must be taken into account when designing a thermoelectric module, including the strength of the materials used. For cast LAST materials, a fracture strength of ~ 15 MPa has been reported [56]. To increase the strength of these materials a separate group at MSU are investigating powder processing and hot pressing of LAST. Through these processes, the grain sizes within the hot pressed samples can be made much smaller (~ 5μm) than in the cast samples (~500μm). This helps to increase the strength of the samples to ultimately make a more robust module [57]. Diffusion along grain boundary paths is the dominant diffusion channels, thus through powder processing the diffusion bonding to the LAST materials is expected to improve. Materials that are placed in environments at elevated temperatures and exposed to static mechanical stresses would undergo a plastic deformation process known as creep [58].

$$\varepsilon = \frac{\Delta l}{l_o} \tag{31}$$

$$\dot{\varepsilon} = \frac{d\varepsilon}{dt} \tag{32}$$

$$\dot{\varepsilon}_s = k\frac{\sigma^n}{GS^b}\exp\left(\frac{-Q_c}{RT}\right) \tag{33}$$

Equation (31) is the definition of creep strain. Equation (32) gives the creep strain rate. Equation (33) gives the relationship gives the relationship of applied stress σ, temperature T and grain size GS to the steady-state creep rate $\dot{\varepsilon}_s$. The values of k and b are material dependent constants. The value of b is typically 2 to 3, and n is between 1 and 6 depending on the creep mechanism. Q_C is the creep activation energy, and T is temperature. Equation (33) shows that the smaller the grain size, the higher the creep strain rate. Higher creep rates mean the interface surfaces will deform more during bonding allowing better interdiffusion of material across that interface [59].

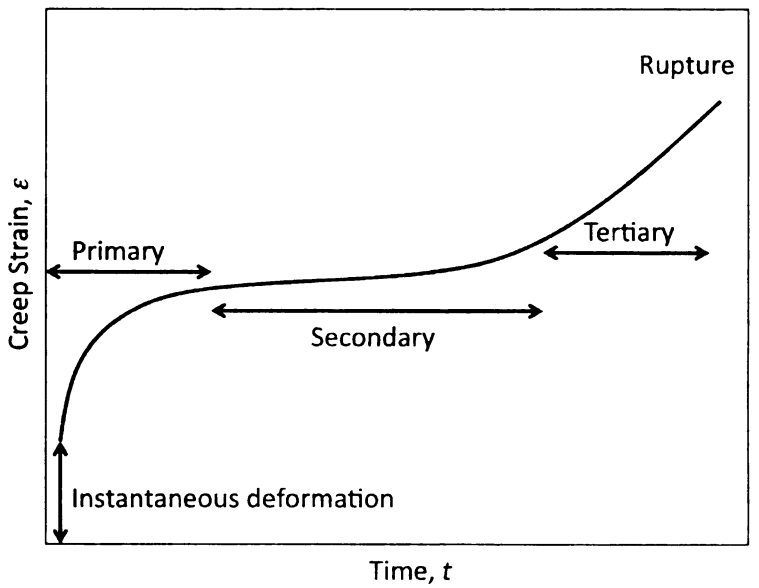

Figure 35: A schematic depiction of a Creep Curve of strain versus time at a constant stress, t_r is the total time to rupture [60].

In Figure 35 is a curve of creep strain vs. time [60]. Primary or transient creep occurs first followed by secondary creep or also termed steady-state creep rate is constant where the slope of the curve tends toward zero. This is when the material retains its ability to deform. The tertiary creep is the materials structural failure. This is normally termed as rupture.

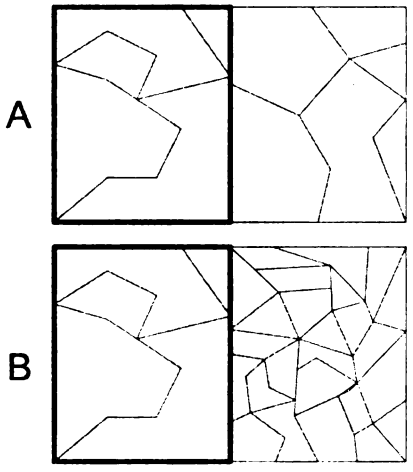

Figure 36: Diffusion bond B will have better interface or contact resistance due to the reduction of the size of the grains in the material.

Figure 36 is a schematic that illustrates a reduction of grain size in the thermoelectric material. With the smaller grain sizes, interdiffusion of material at the interface occurs more readily along the grain boundaries. The reason for the high diffusivity along grain boundaries is the high concentration of defects, especially vacancies, at the grain boundaries. The problem with interdiffusion is that contact material may migrate into the thermoelectric material and change its thermoelectric properties.

Similar thermoelectric materials, such as lead telluride have been extensively investigated. Studies have focused on the poisoning of PbTe from different metals as contacts [61]. Initial studies on lead telluride based modules showed degradation of the power generation capabilities over time and Eiss [61] believed it to be associated with failure of the bond between the lead telluride and the metal shoes used as electrical contacts. He studied the poisoning of the thermoelectric legs by

inter-diffusion of contact material between the lead telluride and the braze zone or shoes, and the cracking that would result from stresses generated during the bonding process. He observed the effects were inversely proportional to the melting temperature of the metal contact. The studies were conducted by measuring electrical conductivity and thermopower changes to the materials before and after bonding. Also measurements were done after thermal cycling to see if more changes to the lead telluride properties have occurred. He noted the changes in these properties and documented which elements changed, or "poisoned" the thermoelectric material more. Shown in Table 4 is an example of how PbTe's thermoelectric properties changed with the addition of a contact metal.

Table 4: Changes in thermoelectric properties of PbTe from brazed materials[61].

Material	Temp °C	Thermopower % Change	Electrical Conductivity % Change
n-PbTe to Cu	106	-56	-52
	164	-50	
p-PbTe to Cu	104	-100	164
	154	-100	
n-PbTe to Fe	97	6	-5
	158	7	
p-PbTe to Fe	99	94	
	152	73	261
	96	68	
	149	91	

Stress can arise from the differences in thermal expansion of the contact metal and the thermoelectric material. Eiss considered a bond by brazing, and it was apparent that below the brazing temperature the component having the higher coefficient of expansion would be in tension and that the stress level will continually increase as the bond temperature is lowered [61]. In addition it was shown that the lowest electrical contact was formed when the braze layer was heated to a softening

state where significant deformation occurs. If the interdiffusion of the contact material into the LAST degrades its properties, diffusion barriers will be needed.

Interdiffusion can also be a source of stress at the contact [62]. The stress generates if the total vacancy flux occurs due to a difference of the intrinsic diffusion coefficients, also known as the Kirkendall Effect [63].

Diffusion barriers are used to aid in stopping migration of contact atoms into the bulk material [64,65]. Long term studies of the contacts will be undertaken to ascertain the stability of the contacts and to help determine if poisoning of the samples is occurring. In Ono's paper, a study was done on six different elements as diffusion barriers of copper into silicon. Copper has been of great interest as a interconnect material because of its lower resistivity and higher electromigration resistance than aluminum [64]. Titanium, chromium, niobium, molybdenum, tantalum, and tungsten were investigated as the diffusion barrier layers. These elements are listed in Figure 37 in the order of self-diffusion coefficients in transition metals between 400-600°C [66].

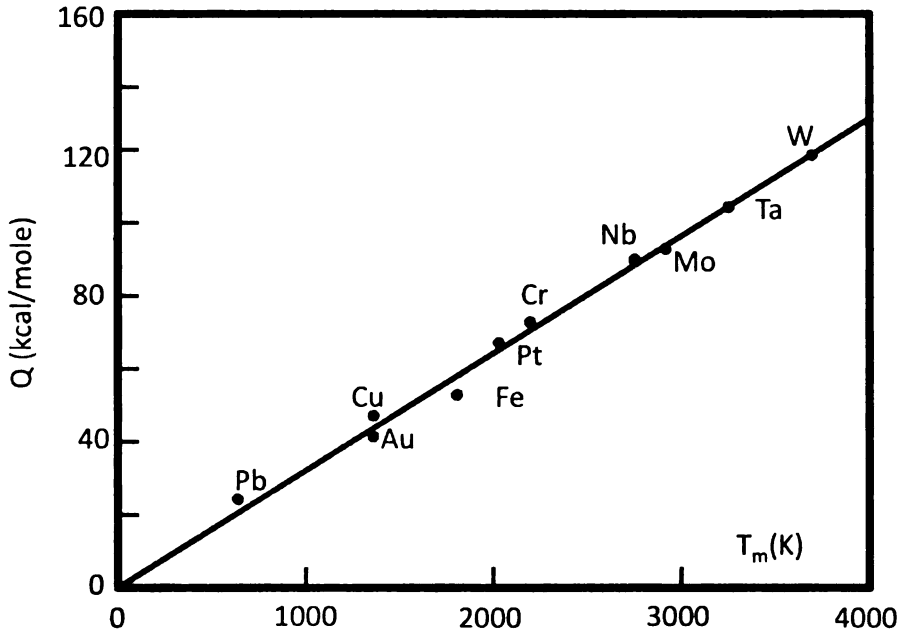

Figure 37: Self-diffusion activation energy as a function of the melting temperature[67].

$$D = D_o \exp\left(\frac{-Q}{kT}\right) \tag{34}$$

$$\vec{J} = -D \cdot \nabla C \tag{35}$$

Equation (34) shows the exponential dependence of diffusivity D for elements as a function of the self diffusion activation energy Q. According to Figure 37; tungsten, tantalum, molybdenum, and niobium have the highest values of Q which yields the lowest values of diffusivity. Equation (35) gives the relationship between mass diffusion flux, J as a function of the diffusivity. The lower the diffusivity, the less mass flux will be. Therefore, tungsten and tantalum are candidates for diffusion barriers. In Ono's paper, the diffusion metal was deposited on a silicon wafer by sputtering, followed by a layer of copper. By studying the resistance changes after

annealing, they concluded that tantalum and tungsten were the two best diffusion barriers of copper into the silicon.

4.2 Diffusion Furnace

A three zone diffusion furnace was designed and assembled for an operating temperature up to approximately 1000°C with a controlled atmosphere (typically vacuum or an argon hydrogen mixture). For full operating procedures, see reference [68].

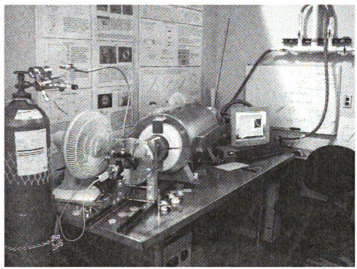

Figure 38: Diffusion bonding furnace.

The furnace interior temperature is measured by a thermocouple that is placed into the center zone of the furnace, and the Ar/H_2 gas mixture 95/5 is used as a forming gas to help remove surface oxides that could degrade the quality of the bonds.

Temperature control of the diffusion furnace is accomplished with temperature controllers for each of the three zones of the furnace.

A pressure controller was added to the diffusion furnace to create a flow of the argon-hydrogen through the system. The gas would flow at around 1 liter per minute while maintaining a total pressure of 800 Torr in the system at all times. This would replenish the reducing gas during the entire bonding run.

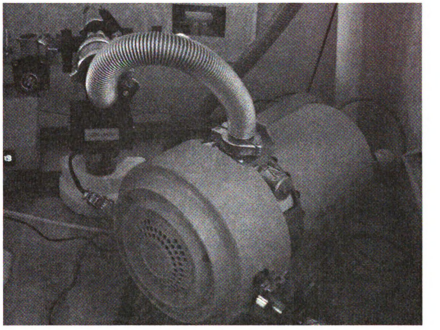

Figure 39: Diffusion furnace pumping system with computer controlled pressure mechanism.

Diffusion bonding experiments were labeled with letters. The first experiment was labeled with A and then the second B and so on.

4.3 304 Stainless Steel Diffusion Bonds to LAST and LASTT Material

Table 5: Stainless steel properties.

Stainless Steel	Composition	CTE (K^{-1})	Melting Point (°C)	Room Temperature Electrical Conductivity (S/cm)	Thermal Conductivity (W/m•K)
304	$FeCr_{18}Ni_{10}$	18.0	1400-1455	14,000	16.3
316	$FeCr_{18}Ni_{10}Mo_3$	16-18	1370-1400	13,000-14,000	16.3
410	$FeCr_{12}$	10-12	1480-1530	14,000-18,000	18-24

The above table shows the different stainless steels and their corresponding properties. These stainless steels were chosen for their CTE's being approximately to that of LAST and LASTT.

4.3.1 First Bond Experiment

A bonding experiment of 304 stainless steel to LAST and LASTT was done. The bonding temperature was 700°C for 4 hours. Thirteen unicouples were placed in the boat initially and only 8 bonded, for a bonding yield of better than 50%.

The first bonding experiment of LAST and LASTT to 304 stainless steel showed promising results, so a second bond was attempted. The bond was done at 700°C with a 4 hour ramp and 4 hour soak. Only 5 out of the 13 unicouples bonded.

4.3.2 Unicouple Fabrication with 304 Stainless Steel

For unicouple run A, ETN133 and ETP16 were bonded to 304 stainless steel using a 4 hour soak at 700°C. Below are results for this bonding run.

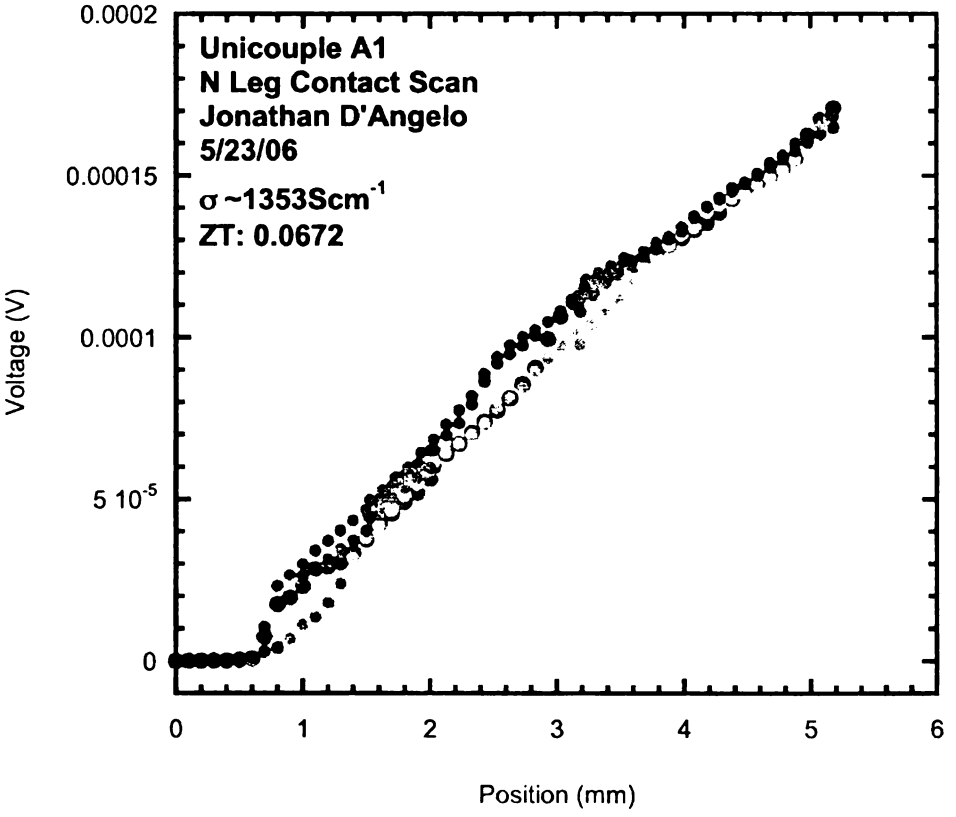

Figure 40: Unicouple A1 N leg scan.

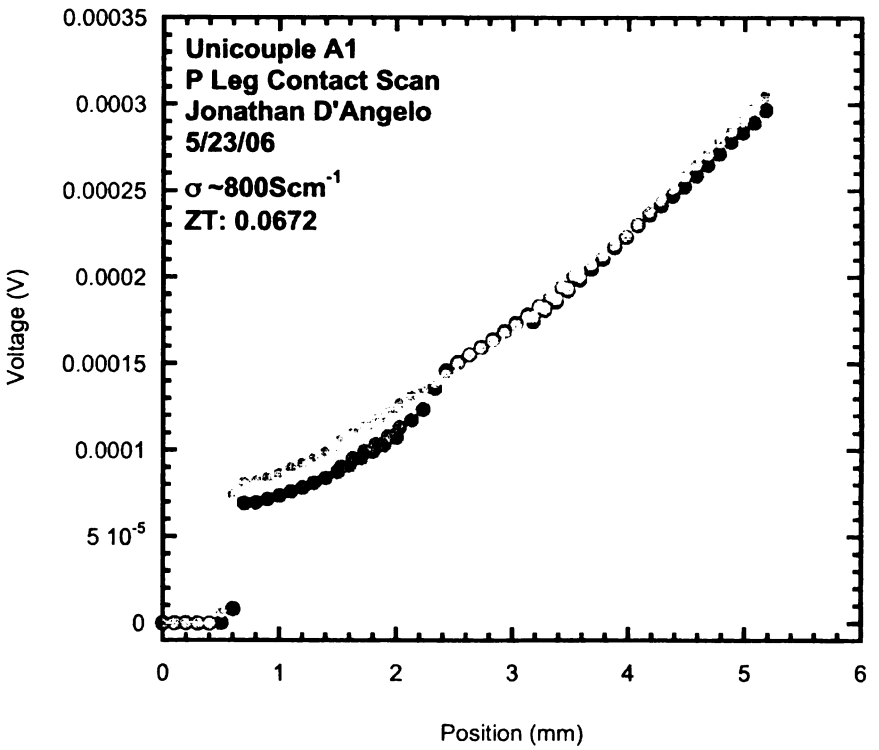

Figure 41: Unicouple A1 P leg scan.

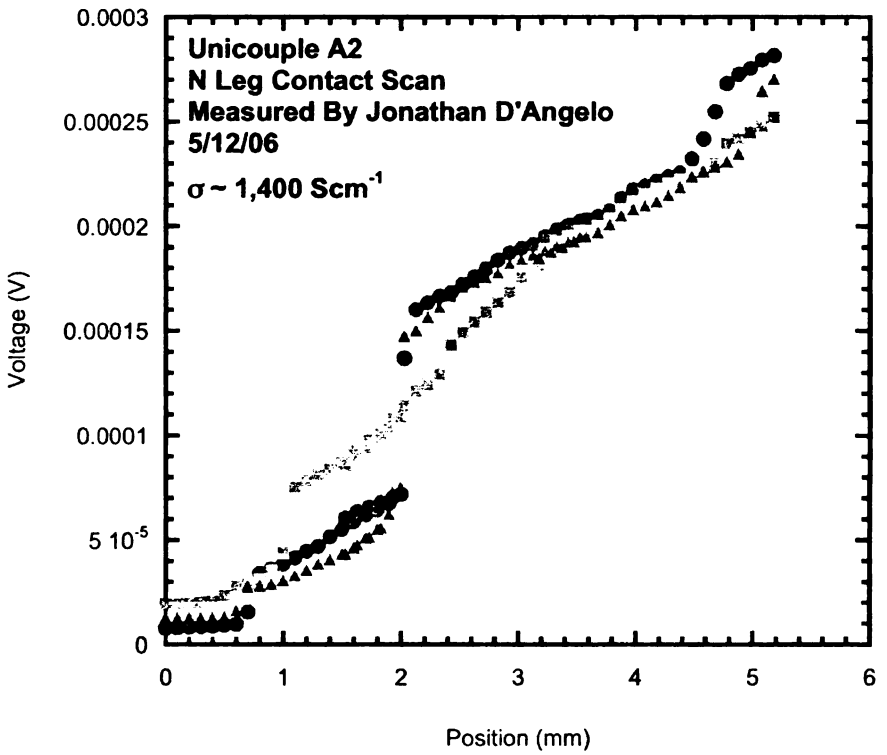

Figure 42: Unicouple A2 N leg scan.

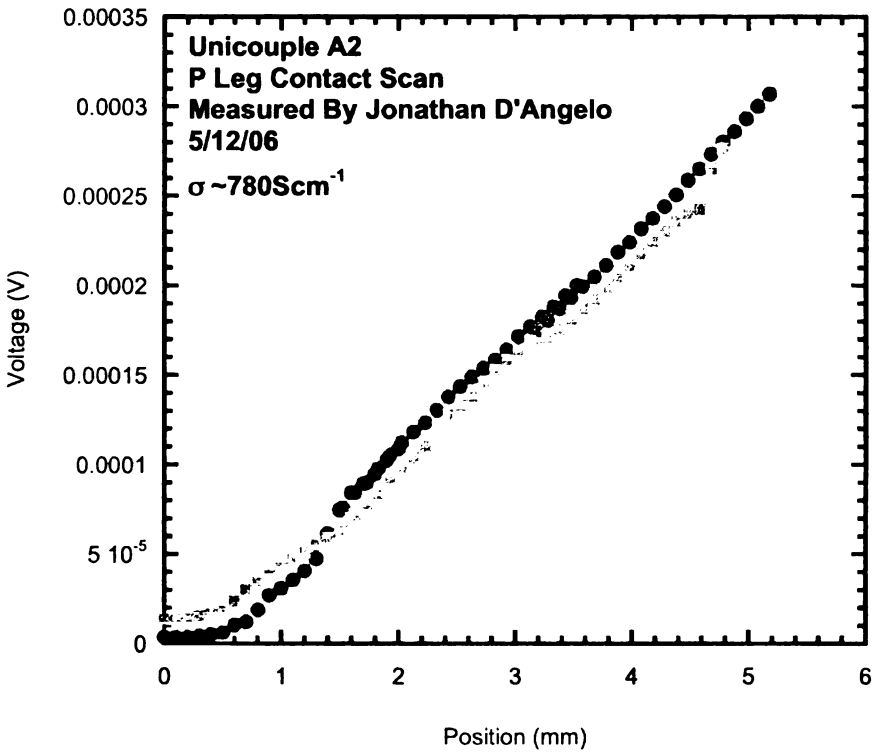

Figure 43: Unicouple A2 p leg scan.

The room temperature ZT for unicouple A2 was measured to be 0.015. The expected value was approximately 0.3.

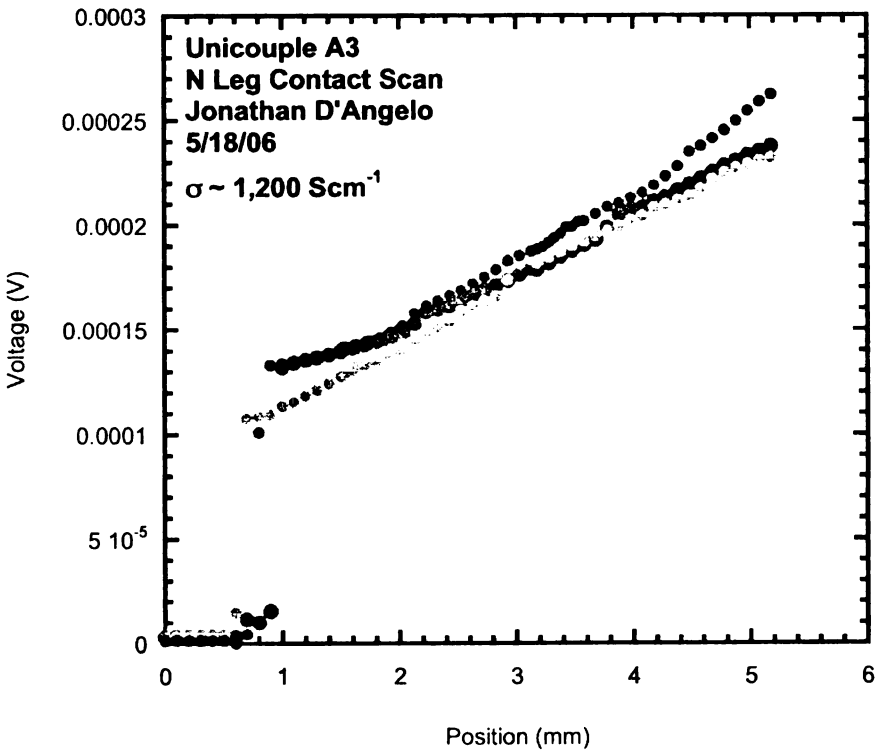

Figure 44: Unicouple A3 N leg scan.

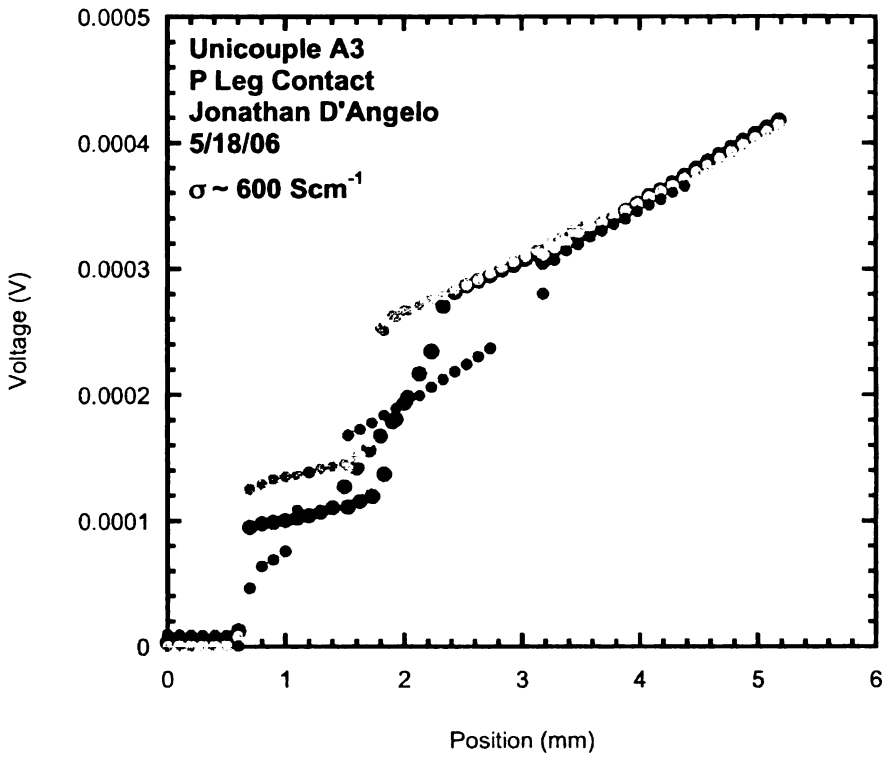

Figure 45: Unicouple A3 P leg scan.

Unicouple A3 has a room temperature ZT of 0.08. A lead-tin solder was added to the top of the electrode in an attempt to lower to unicouple's resistance. This decreased the module resistance 2mΩ. This however, did not significantly change the ZT for the module giving a new ZT of 0.079 after adding the solder bridge.

A second experiment was done to decrease the resistance from the metal electrode by soldering a copper wire down to the 304 stainless steel and the ZT was tested again.

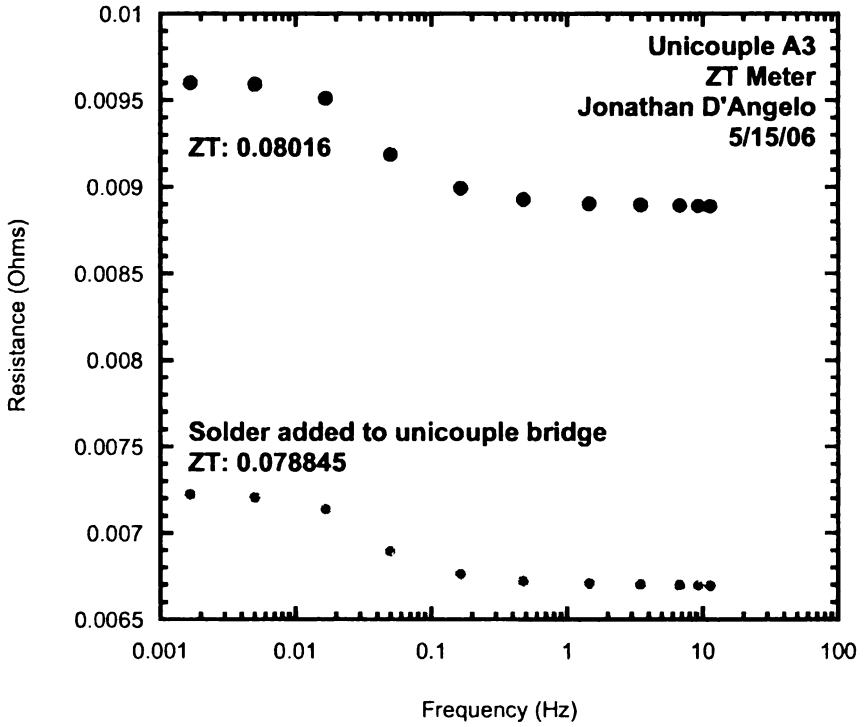

Figure 46: ZT measurement with and without solder.

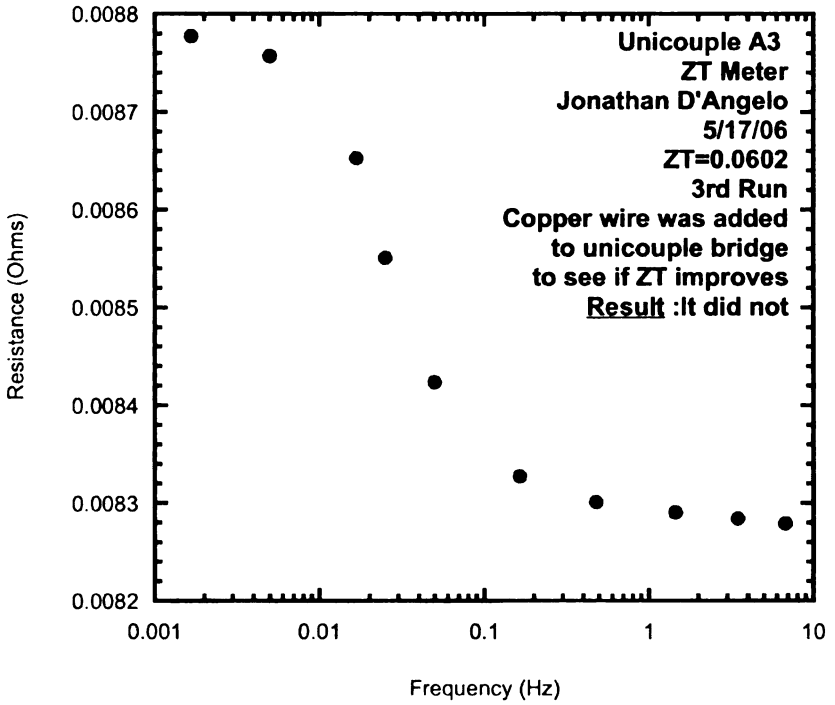

Figure 47: ZT measurement with copper wire added. ZT dropped down to 0.0602 even though overall resistance of the unicouple was improved.

As shown in Figure 47 the ZT does not improve with the lowering of the electrode resistance through this technique. This may have been caused by the module resistance being dominated by contact resistance.

When the forming gas was not used, and a lower pressure was used during bonding (30 minute ramp to 700°C and 4 hour soak at 700°C), no bonds were formed between 304 stainless steel and LAST.

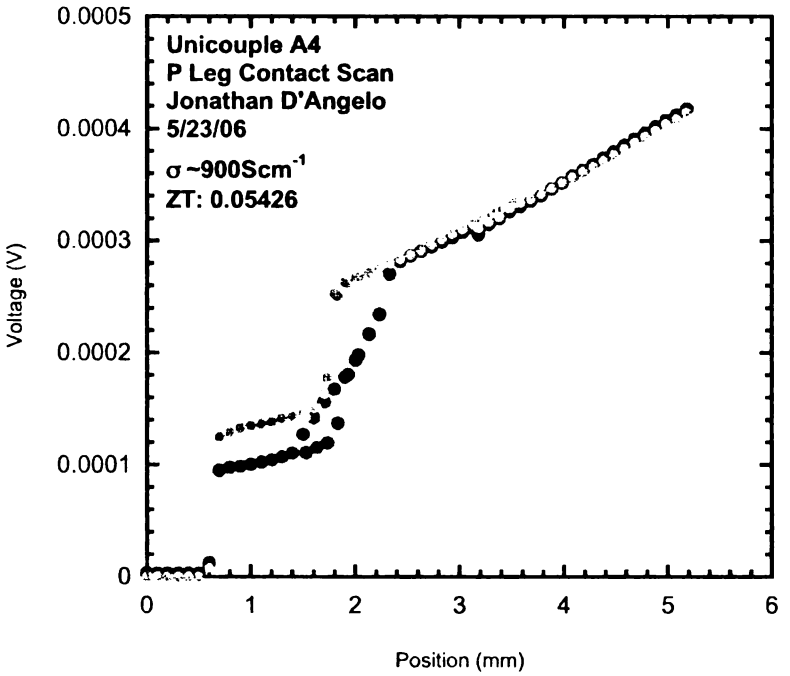

Figure 48: Unicouple A4 P leg scan, there are visible cracks along the length of the sample.

For unicouple bonding run A, most of the contacts show a low contact resistance, however most of the thermoelectric legs did show signs of cracks in the voltage scans. The cracks in the legs increase the resistance of the unicouple and decrease the strength. For module construction, unicouples based on LAST and LASTT should have room temperature ZTs of approximately 0.3 and have no cracks in the legs of the material.

Unicouple run I was a two stage bond of ETN137 and ETP25 to 304 stainless steel. The two stage run has a 30 minute ramp for the n-type bond and 4 hour ramp for the p-type material. Both bonds have soak times of 4 hours at 700°C. Only 6 of

20 unicouples were fabricated from this run. The reason for the low bonding yield was not clear, so another bonding attempt was made.

Unicouple run U is a bond of ETN142 and ETP26 to stainless steel 304. The coefficient of thermal expansion of 304 stainless steel, 18ppm, is a closer match the LAST and LASTT, ~21ppm than that of stainless steel 410, which has a CTE of 10ppm.

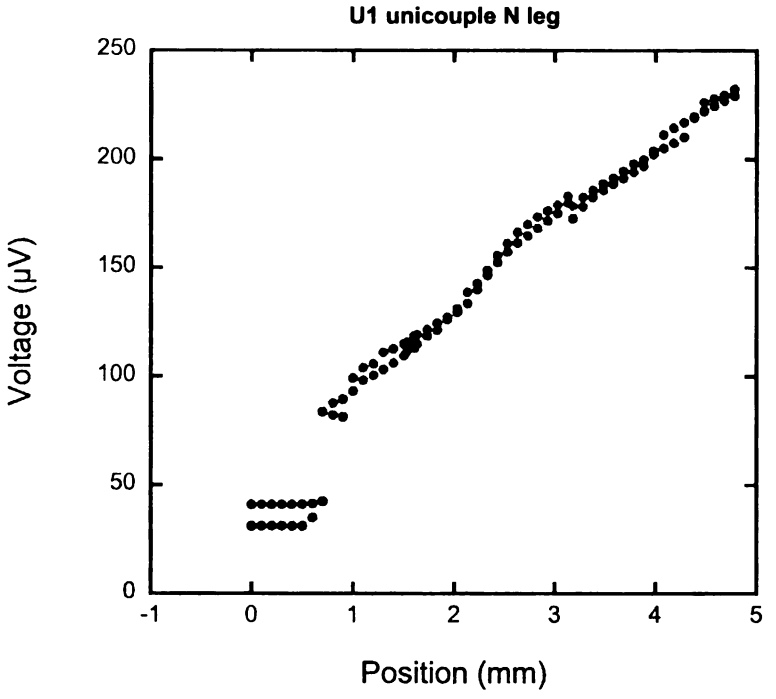

Figure 49: Unicouple run U N leg scan.

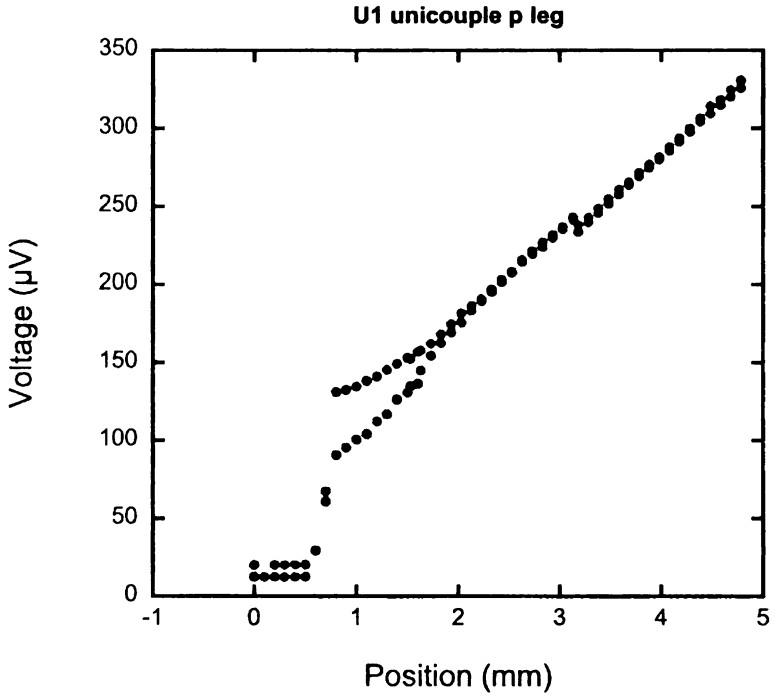

Figure 50: Unicouple run U P leg scan.

The bonding of LAST and LASTT to 316 shows a relatively low contact resistance below $50\mu\Omega cm^2$, and the material has fewer cracks after bonding. This suggests the CTE mismatch may cause cracks in the material rather than the pre-bond thermoelectric material having indigenous cracks.

Furnace run V and W were done simultaneously. One boat was a bond of ETN149 and ETP24 to stainless steel 410 and the other boat was a bond to 304 stainless. The bonding run was only done in one thermal treatment stage consisting of a 4 hour ramp and a 5 hour soak at 700°C. The 304 stainless steel interconnects bonded 4 unicouples of 4 put in the furnace while none of the 410 stainless steel

electrodes based unicouples bonded. The 304 stainless bonds well with only a one stage bond.

Furnace run X was a bond of ETN149 and ETP33 to 304 stainless steel. A one thermal treatment stage bond consisting of a 4 hour ramp and a 5 hour soak was used. Nine out of 15 unicouples were bonded, however a significant contact resistance was found at the LAST to stainless steel 304 bond as indicated in Figure 51: Scan of N leg from unicouple run X. This shows a high contact resistance of the n-type material to the 304 stainless steel Figure 51.

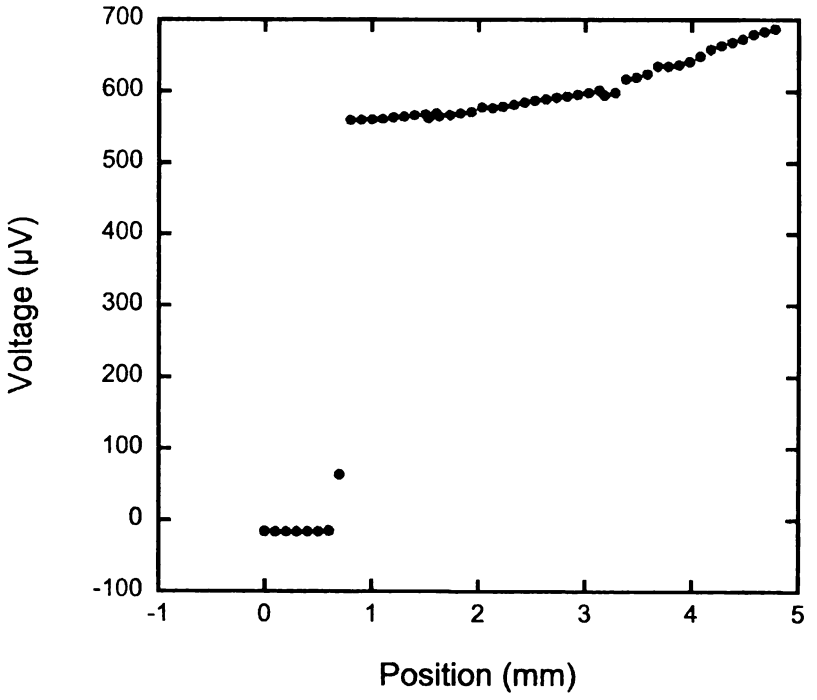

Figure 51: Scan of N leg from unicouple run X. This shows a high contact resistance of the n-type material to the 304 stainless steel.

4.4 410 Stainless Steel Diffusion Bonds to LAST and LASTT Material

As indicated in the last sectionm bonding of stainless steel to the LAST material has shown promising results. Development of a module with diffusion bonded contacts to stainless steel 410 was done using a 30 minute ramp time to 700°C and a soak time of 4 hours at 700°C. The total soak time was 4 hours. The furnace was filled with argon to a pressure of 350Torr and then sealed off. During the rise in temperature the furnace would reach a pressure of near atmosphere to inhibit outgassing of the thermoelectric material at such high temperatures.

For this experiment a four leg mold of R300 was built to cast the module legs before bonding.

Figure 52: Module Legs Cast in R300.

The R300 is a thermal insulator primarily used in furnace insulation. The purpose of the R300 is two fold. First is to keep the legs from outgassing during operation, and second is for mechanical support. Figure 52 shows a picture of the legs cast into

the R300. All of the electrical connections were to be diffusion bonded at one time. Figure 53 shows how the module was setup to be bonded.

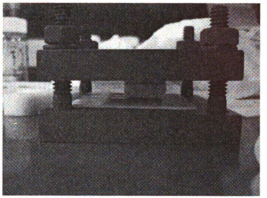

Figure 53: R300 module bonding setup.

Figure 54: Completed module, top view.

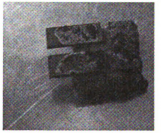

Figure 55: Completed module, bottom view.

All eight connects of the module were successfully bonded. Figure 54 and Figure 55 show pictures of both the hot side and cold side interconnects. Unfortunately no

measurements were done on this module, because the contacts on the hot side fell off during the polish of its surface. This experiment was an example of bonding a complete module in one step. This can speed up the fabrication process, however it also requires that all contacts must bond to complete a module. Bonding individual unicouples and then fabricating an entire module would prove to be a superior method.

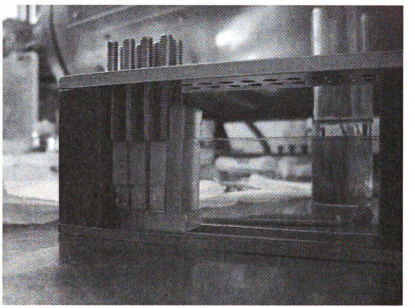

Figure 56: This diffusion boat has a set screw for both n and p legs for during diffusion bonding.

The first bonding experiment done with this diffusion boat shown in Figure 56 used a 30 minute ramp time to 700°C, and a 5 hour soak time. The starting pressure of the furnace was 332 Torr of argon. All four unicouples in the experiment bonded, but the p-type material showed signs of degradation. At low atmospheric pressure and the bonding temperature used, the thermoelectric legs are known to outgas

during bonding, therefore another experiment was run using an intial pressure of approximately 420 Torr.

The soak temperature, ramp time, and soak time remained the same as before. The unicouples formed at the higher pressure showed less degradation at the interfaces as shown in Figure 57.

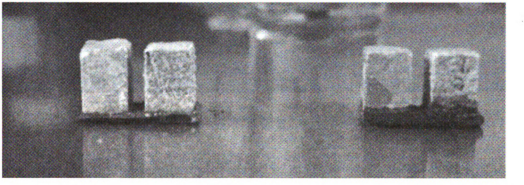

Figure 57: The unicouple on the left had the starting pressure of 420 Torr, and the unicouple on the right had a starting pressure of 332 Torr.

The room temperature ZTs of the unicouples were measured using a direct ZT measurement technique [69] and showed a ZT of 0.2. The stainless steel used was 410, ($FeCr_{12.5}$). The 410 stainless steel has a electrical conductivity of 17,857 S/cm. A calculation of the resistance of the metal interconnects shows that its resistance should be 337μΩ. Resistance in the micro-ohms is the threshold for metal interconnects. The bonding of the 13 unicouples was done using a 30 minute ramp to 700°C followed by a 4 hour soak at 700°C, and a starting pressure of 414 Torr of argon. Only 6 of the 13 unicouples bonded. Also 5 of the six bonded show signs of outgassing. The unicouples that did not bond did not have adequate

mechanical pressure applied to the legs to allow for bonding. The next bonding run, less unicouples were attempted at bonding, and a higher starting pressure was used.

A follow up bond of seven unicouples was done with the same conditions attempted to bond the 13 unicouples, but with a higher starting pressure of around 450 Torr of argon.

Figure 58: Unicouples built with starting pressure of 450 Torr.

The measured ZT on these unicouples was 0.16 at room temperature, and a 12 leg module was built from them as shown in Figure 59.

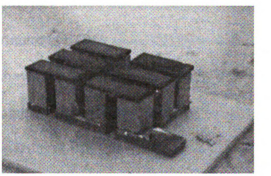

Figure 59: Side view of a 12 leg module.

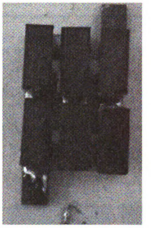

Figure 60: Top view of 12 leg module.

A bond run of 7 unicouples was done at 700°C, ramp of 30 minutes, soak of 4 hours, and a starting pressure of 420 Torr of argon. Five of the 7 unicouples bonded. The material used for this experiment showed visible surface cracks. Such cracks at the bonding interface inhibit the diffusion bonding process [70].

A bonding experiment of ETP19 and ETN126 to 410 stainless steel was carried out. Figure 61shows the power factor for ETN126 which peaks at 15 at around 500K and the sample exhibited signs of evaporation or sublimation after the measurement. The properties of ETP19 were not measured.

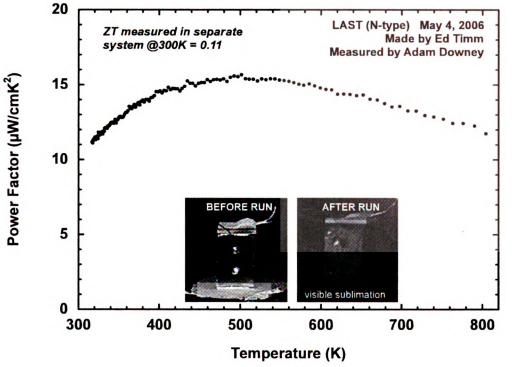

Figure 61: Power Factor for ETN126.

Eighteen unicouples were loaded and 14 bonded successfully. The four unicouples that did not bond did have bonds between the p-type material and the metal electrode, however the n-type material to metal electrode did not bond.

Figure 62: shows the 14 unicouples bonded at 700°C for 4 hours.

Unicouple run B was a bond of n-type LAST and p-type LASTT to 410 stainless steel. The bonding temperature was 700°C for 4 hours with a 30 minute ramp.

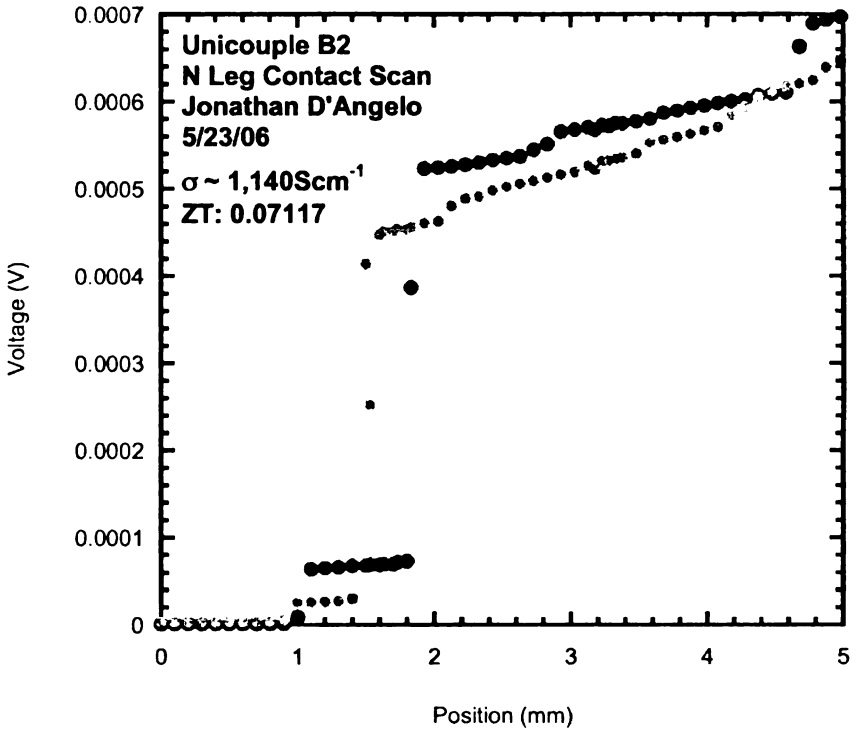

Figure 63: Unicouple B2 voltage scan of the N leg contact.

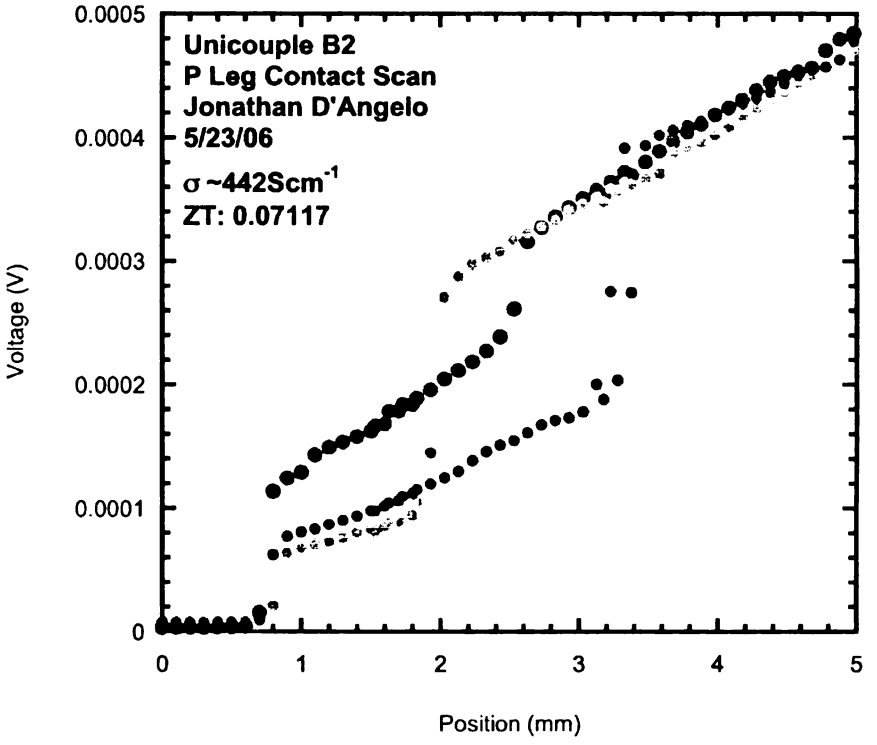

Figure 64: Unicouple B2 P leg scan.

Unicouple B2 resistance is 11.8mΩ and the room temperature ZT is 0.071 which is higher than other unicouples with resistance above 10mΩ. The higher ZT in this case may be contributed to better thermopower or lower thermal conductivity. The measured ZTs of the other unicouples in bonding run B were as follows; B3-0.077, B4-0.057, B5-0.062, and B6-0.076. The ZTs are still lower than what is needed for good module performance, but repeatability is also of great importance.

Unicouple run C used the same material as run B, but a 4 hour ramp was used instead of 30 minutes. Only the p-type bonded to the 410 stainless steel. Thus experiments using two stages during the bonding were investigated.

For unicouple run D the first stage of the bonding the n-type material (ETN134) was bonded to the 410 stainless steel using a a 30 minute ramp time followed by 4 hours of annealing at 700°C. After stage 1 of this bonding experiment, the samples were removed from the furnace and inspected. Seven of the eight legs were found to have bonded to the 410 stainless steel as shown in Figure 66. The stainless steel was then lightly polished and the p-type material (ETP32) configured on the electrodes. The unicouples were then placed back in the furnace for stage 2 of the bonding using a 4 hour ramp time followed by 4 hours of annealing at 700°C.

Figure 65: Stage 1 of bond run D.

Figure 66: Run D final unicouples.

Run D finished with 7 completed unicouples as shown in Figure 67. Large voltage drops in the scans shown for the n-type and p-type legs of the unicouples as shown in Figures 68 and 69 indicate significant contact resistance and cracking of the samples.

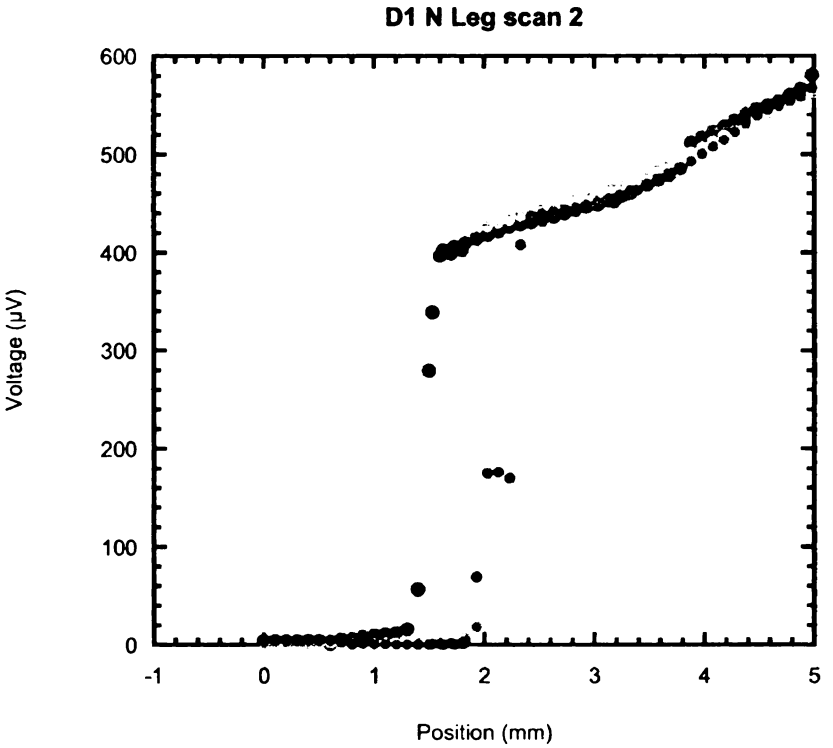

Figure 67: Unicouple D1 n leg scan.

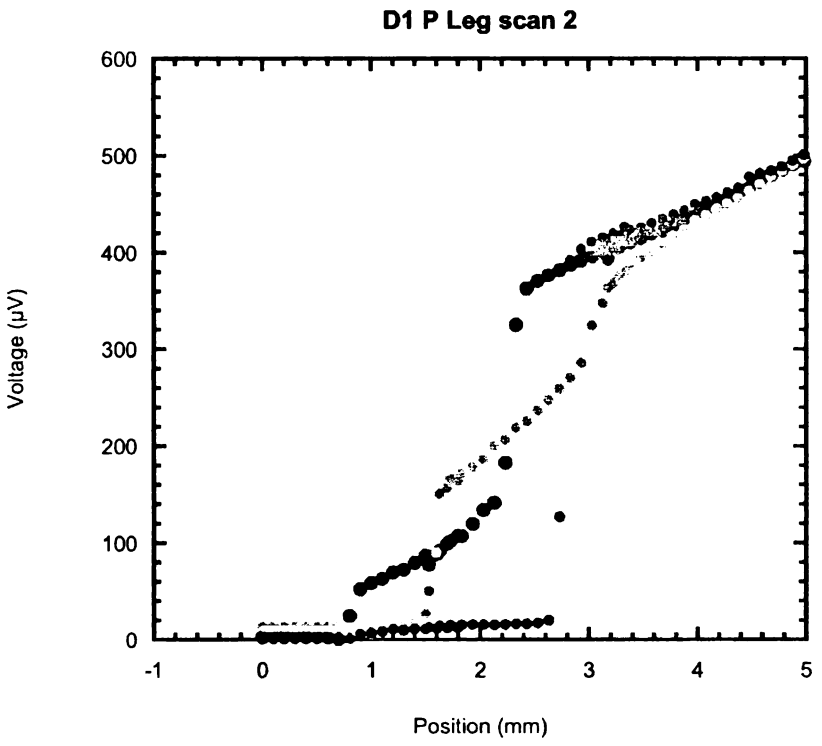

Figure 68: Unicouple D1 p leg scan.

The ZT of the D1 unicouple was 0.077 and for unicouple D3 the ZT was 0.12. The resistance of this D3 unicouple was 15mΩ, which was significantly lower than the other unicouples in this experiment. ZT measurement for unicouples D4 and D5 were 0.078 and 0.099 respectively.

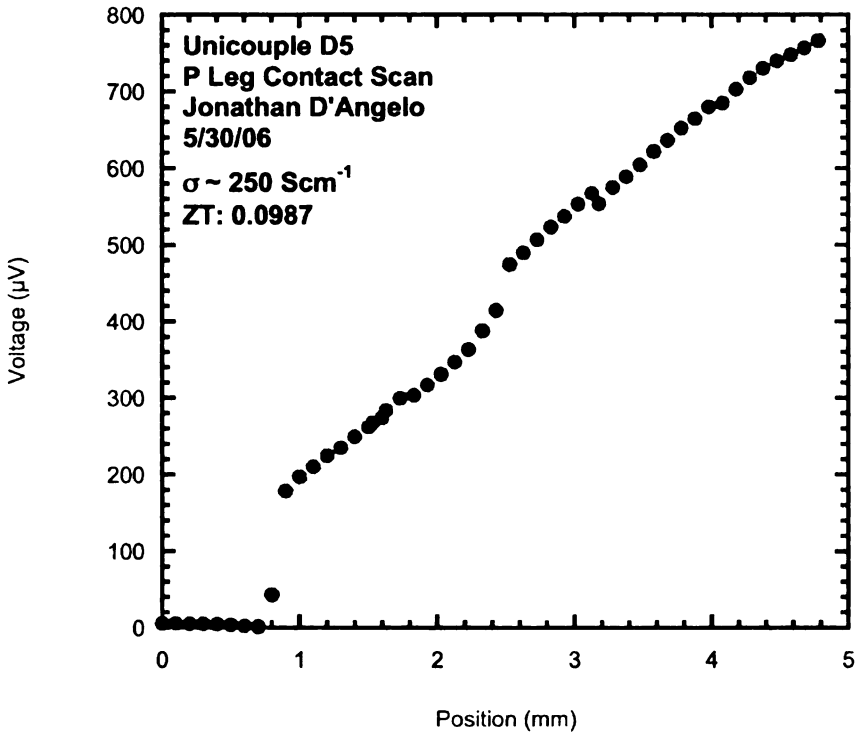

Figure 69: Unicouple D5 p leg scan.

D5 shows a good example of material that does not exhibit significant cracking along the length of the leg. The contact resistance is approximately 500 $\mu\Omega\cdot cm^2$ and the ZT is close to 0.1.

Unicouple run G started with a tellurium deposition onto the n-type legs. The bond was done with a 30 minute ramp and a 4 hour soak at 700°C. For this initial bonding stage, all of the bonds were successful as shown in Figure 71.

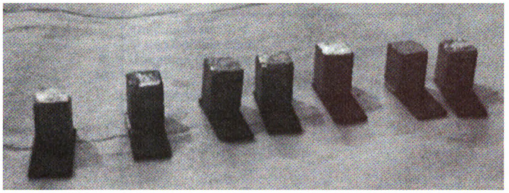

Figure 70: Unicouple run G stage 1 results.

The second stage of bonding was also had 100% success as shown in Figure 72.

Figure 71. Unicouple run G final results. The dot on the material marks the p-type material.

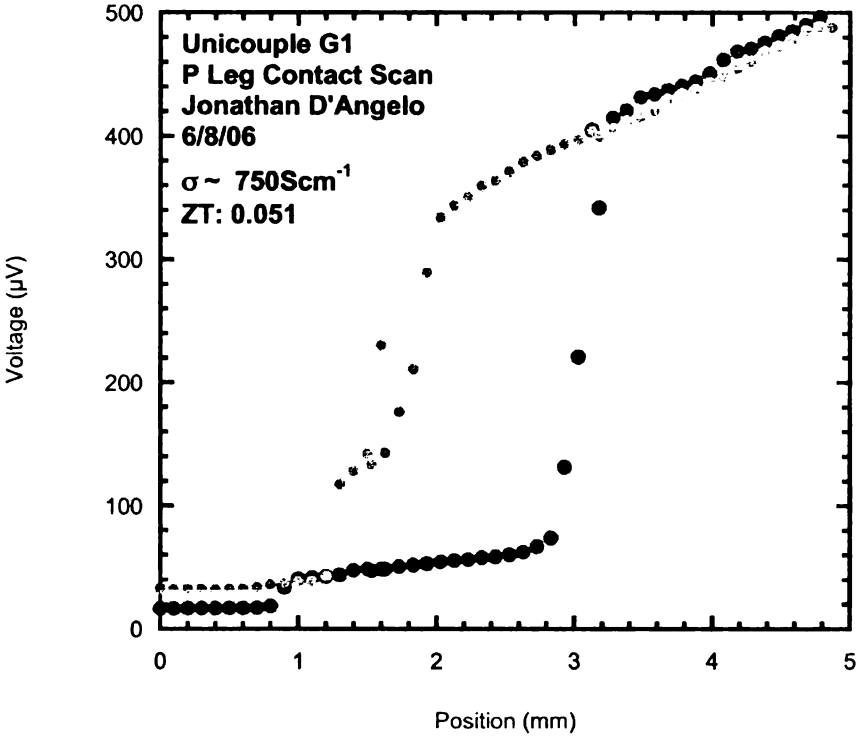

Figure 72: Unicouple G1 contact scan of the p-type leg.

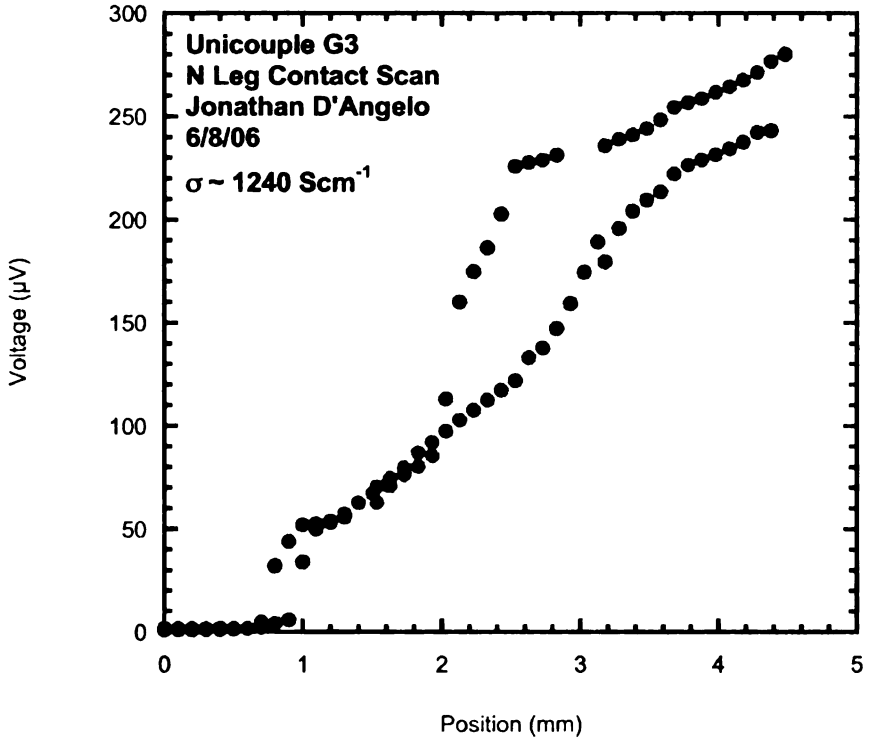

Figure 73: Unicouple G3 N leg contact scan. The ZT for this unicouple was 0.08.

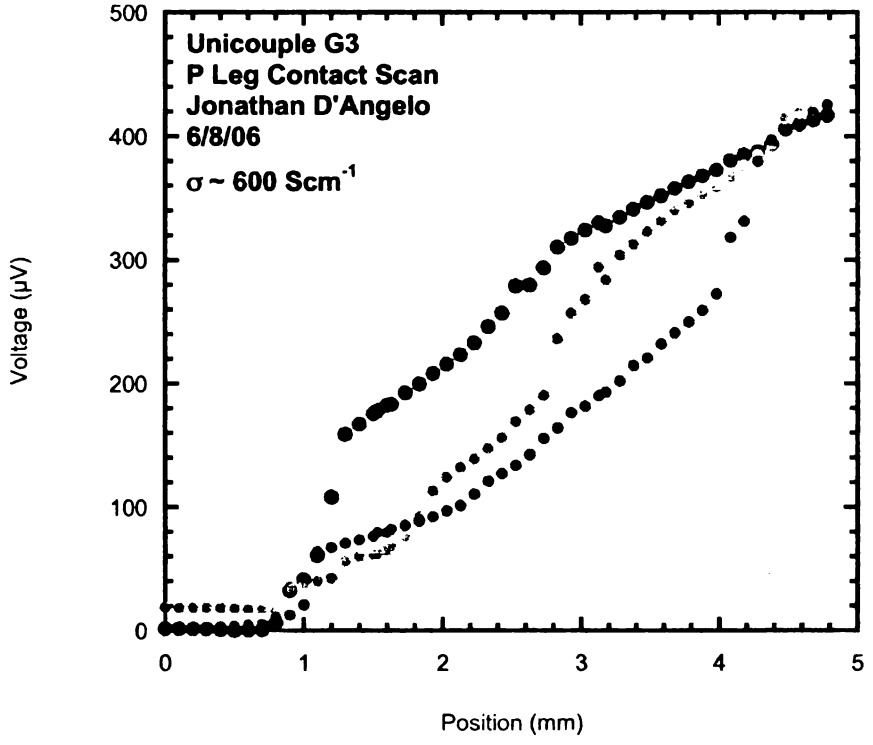

Figure 74: Unicouple G3 P leg contact scan.

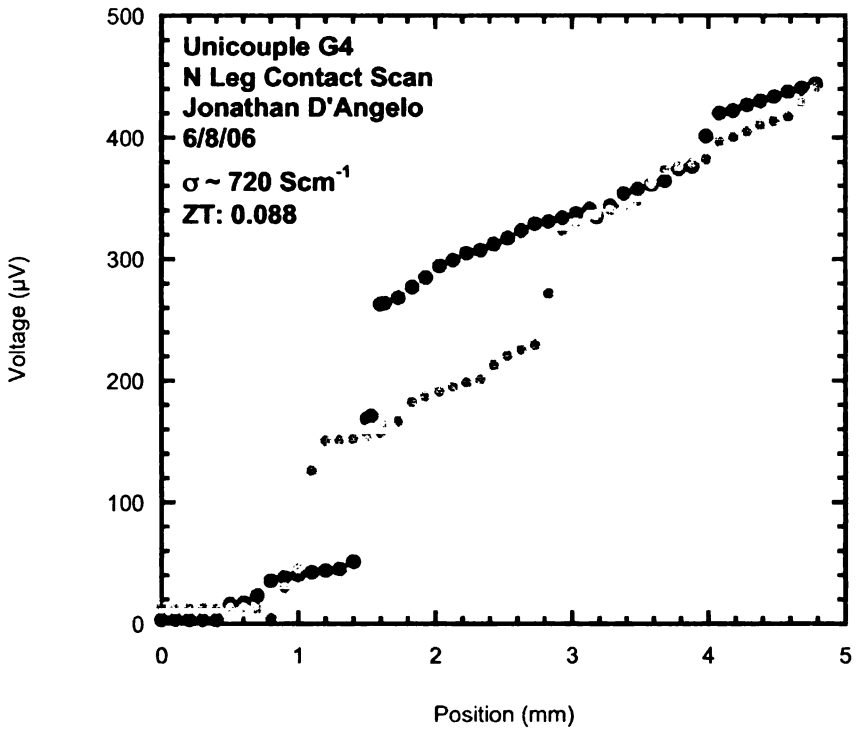

Figure 75: Unicouple G4 N leg contact scan.

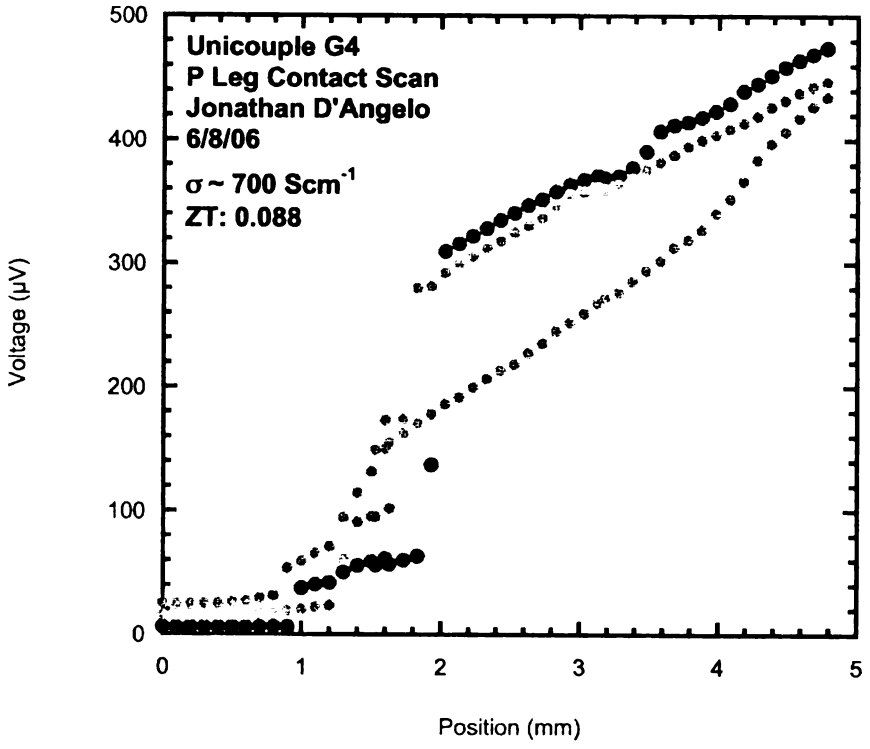

Figure 76: Unicouple G4 P leg contact scan.

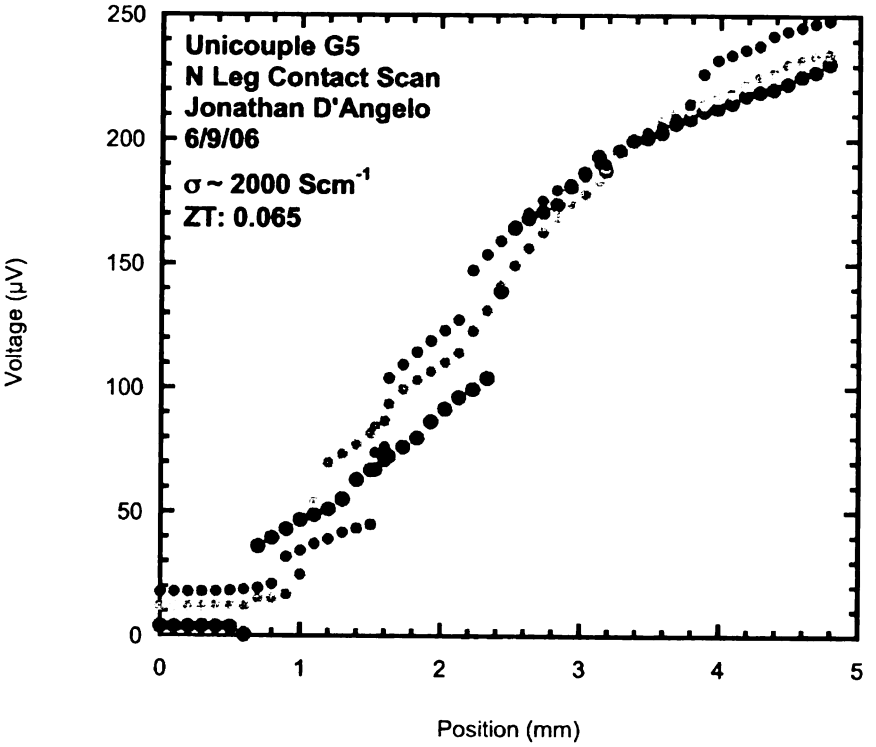

Figure 77: Unicouple G5 N leg contact scan.

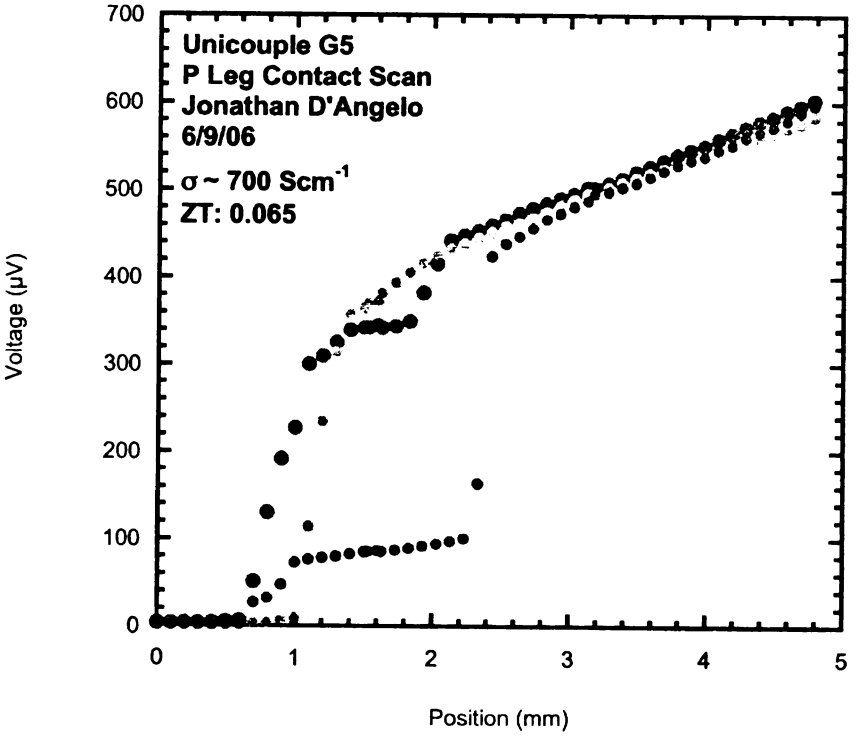

Figure 78: Unicouple G5 P leg scan.

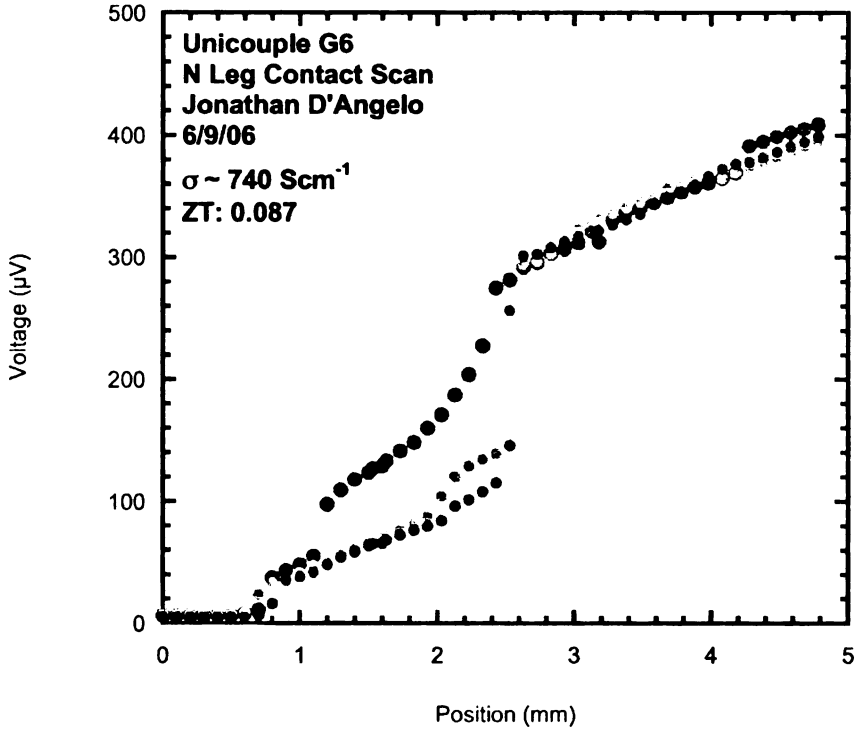

Figure 79: Unicouple G6 N leg contact scan.

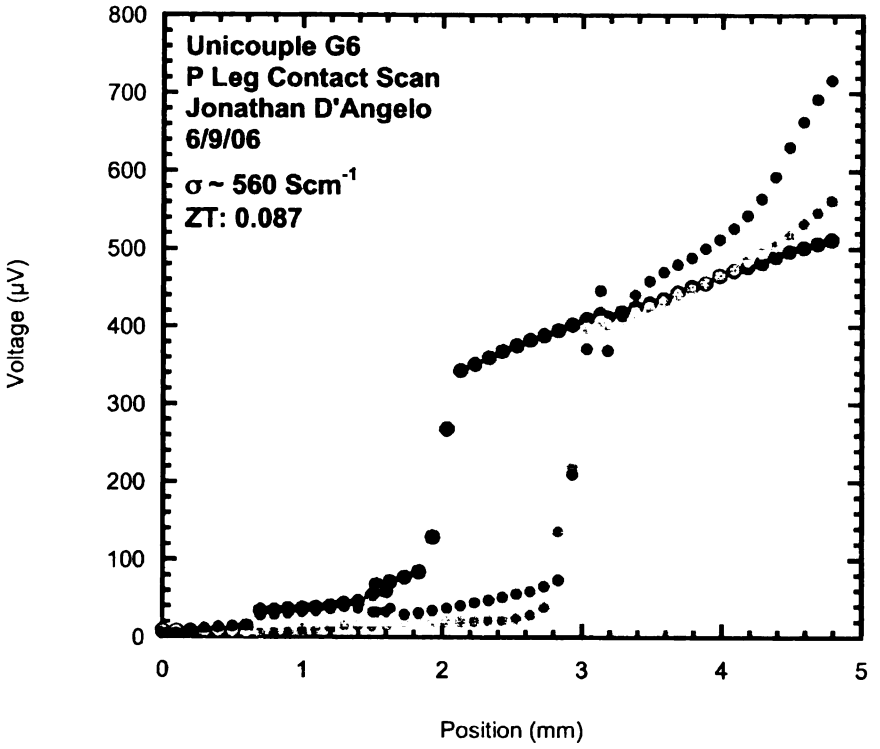

Figure 80: Unicouple G6 P leg contact scan.

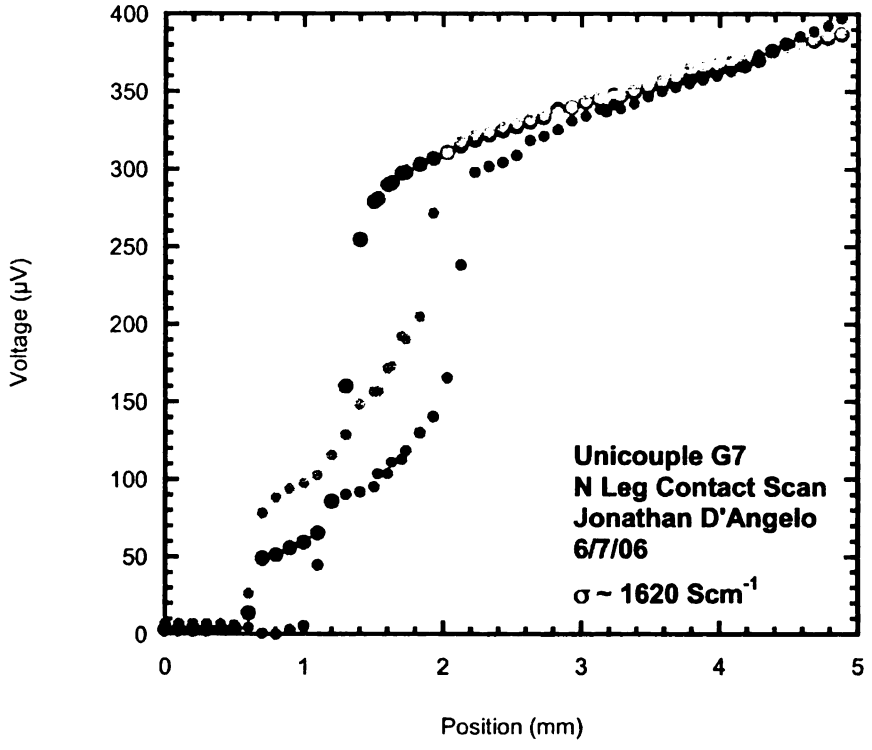

Figure 81: Unicouple G7 N leg contact scan.

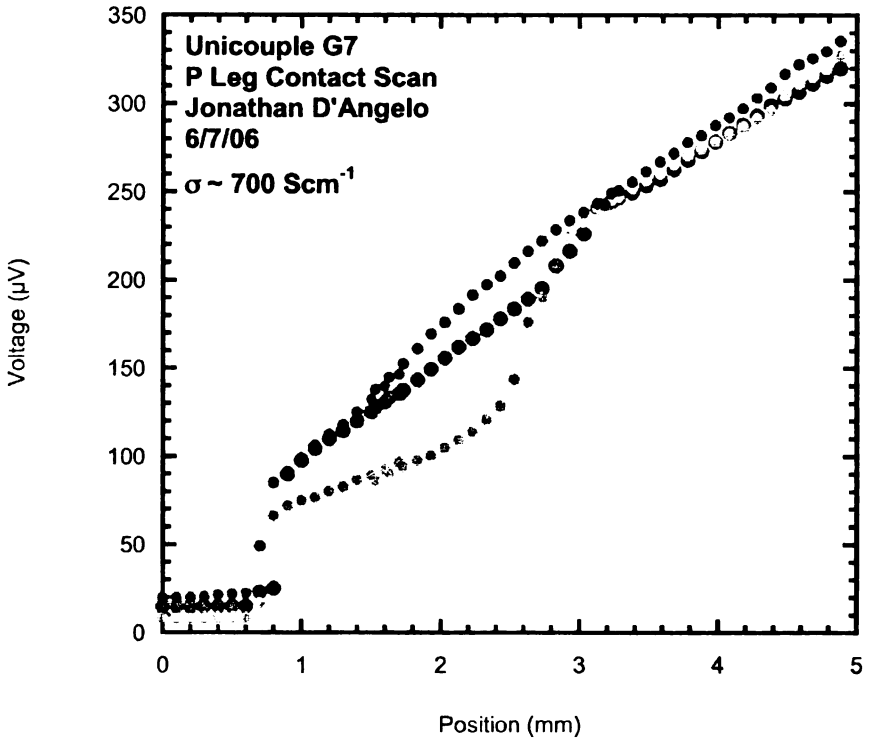

Figure 82: Unicouple G7 contact scan for the p-type leg. The measured ZT for this unicouple was 0.04

Furnace run H was a 2 stage run of ETN137 and ETP25 to 410 stainless steel. Out of 20 initially put in the diffusion furnace to be bonded, 15 unicouples were completed.

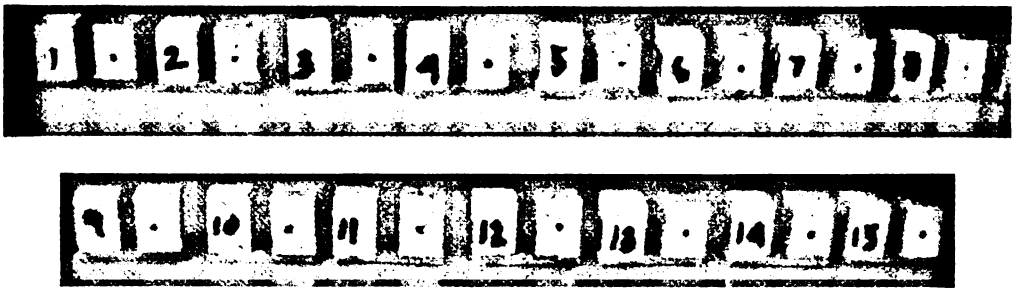

Figure 83: Unicouples fabricated from run H.

Unicouple run J was a two stage bonding to form a unicouple of ETN140 and ETP25 to 410 stainless steel. Twenty two unicouples were fabricated from this runand then used to fabricate modules as will be discussed later.

Unicouple run K was the bonding of ETN141 and ETP25 to 410 stainless steel. With the use of the two stage bonding technique 19 total unicouples were fabricated. Two consecutive bonding runs have shown results of good bonds with different ingot materials. Unicouples from both bonding runs of J and K were used in modules.

Unicouple run L was the bonding of ETN141 and ETP26 to 410 stainless steel again. This time each 410 stainless steel was polished before bonding. The final results of the experiment were no bonds of either the LAST or LASTT material to the polished 410 stainless steel. Thus either the rough surfaces of the 410 stainless steel assisted in the bonding process, or there were contaminants introduced during the polishing process.

With unicouple run M a five hour soak was used. The extra hour was added to possibly aid in annealing of the material along with diffusion bonding the contact. ETN141 and ETP26 to 410 stainless steel and the two stage bonding technique was used. Only 5 out 18 unicouples showed bonding. This low yield may have been caused by a low furnace pressure, which in the past showed poor bonding results. Also the bolts on the bonding device were not double checked to make sure they were tightened down before bonding.

Unicouple run N was a bond of the same material as unicouple run M. This time each bolt was well tightened on the bonding device and the two stage run was used. Ten out of 13 unicouples successfully bonded.

Unicouple run O was a bond of slow cooled ETN143 to 410 stainless steel. A 30 minute ramp with a 5 hour soak at 700°C was used. Only 3 of the 9 legs bonded to the 410 stainless. To investigate the influence of the mechanical pressure on the bonding process, the was redone with all bolts further tightened increasing the torque from 6 to 7 inch pounds. Four unicouples were bonded from this run. One of the goals from unicouple run O was to see if slow cooled material (ETN143 was a slow cooled ingot) would exhibit less cracks throughout ingots. Slow cooled ingots have shown less cracking throughout the ingot.

Unicouple run P was a bond of ETN142 and ETP26 to 410 stainless steel. The bonding surfaces were cleaned with acetone and methanol before loading into the diffusion boat. Only 7 out of 14 unicouples bonded suggesting that surface contaminants are not the cause of poor bonding yield.

Unicouple run Z was a bond of ETN151 and ETP33 to 410 stainless steel. A two stage bond was used with a 30 minute ramp for the n-type bond and 4 hour ramp for the p-type bond. Both used a 5 hour soak at 700°C.

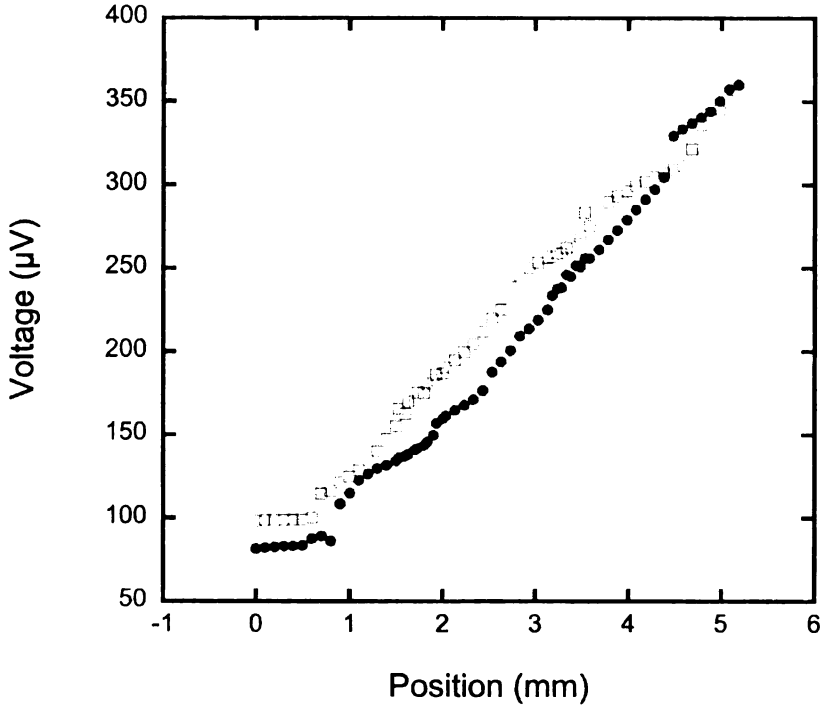

Figure 84: Unicouple run Z, N leg scan.

The scan in Figure 84 shows a low contact resistance, but the bonding yield for this run was below 50%. The best conclusion would be that there was not enough mechanical pressure on each unicouple to allow bonding.

Unicouple run AU was the first run to use the new background gas pressure control system in the diffusion furnace. The run was a bond of ETN173 and ETP40 to 410 stainless steel. The 410 stainless was being tried again because it has a higher electrical conductivity than the 316, but the CTE is around 12ppm which is lower than the CTE for 410 stainless steel. Only one of the legs came out bonded, however none of the legs exhibited signs of outgassing. This showed that a flow of

the argon-hydrogen forming gas could be used during bonding runs to minimize evaporation of the thermoelectric materials.

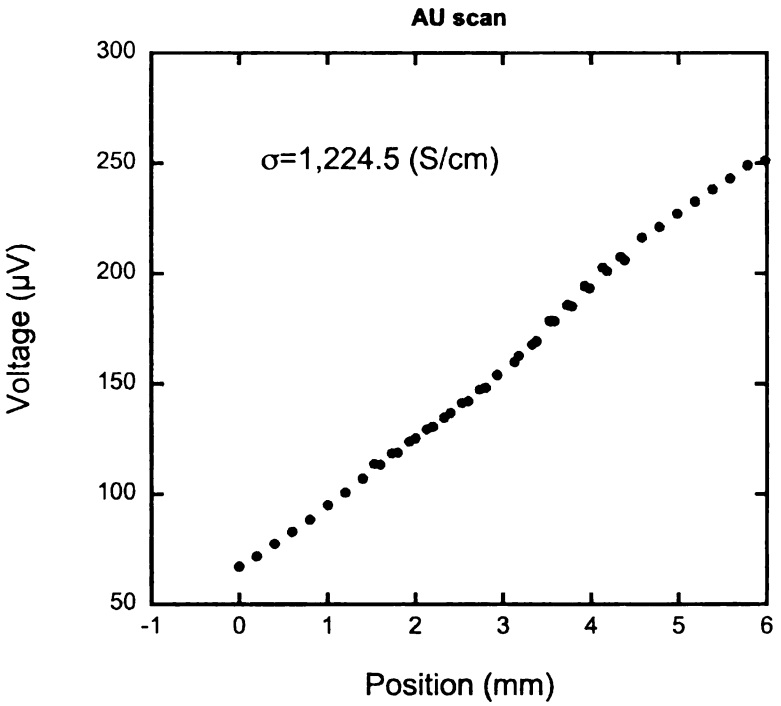

Figure 85: Scan of N leg from run AU.

Figure 85 shows a scan of a n-type leg that was part of bonding run AU. This confirms no change in the electrical properties of the material. Samples in the past have outgassed if the pressure was too low. A visual inspection showed no change in the physical properties.

4.5 Diffusion Bonds of $Sn_{0.3}Fe_{0.3}Te$ to LAST and LASTT Materials

An alloy of tin, iron and tellurium was made, $Sn_{0.3}Fe_{0.3}Te$, and used at the interface between stainless steel and the thermoelectric materials during a bond at 700°C with a 4 hour soak.

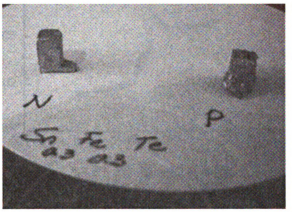

Figure 86: Bonding results of LAST and LASTT to Sn-Fe-Te alloy.

Since the p-type material deformed during the bonding process a room temperature scan of the contact was not possible. The n-type leg and contact was scanned for its room temperature contact resistance shown below.

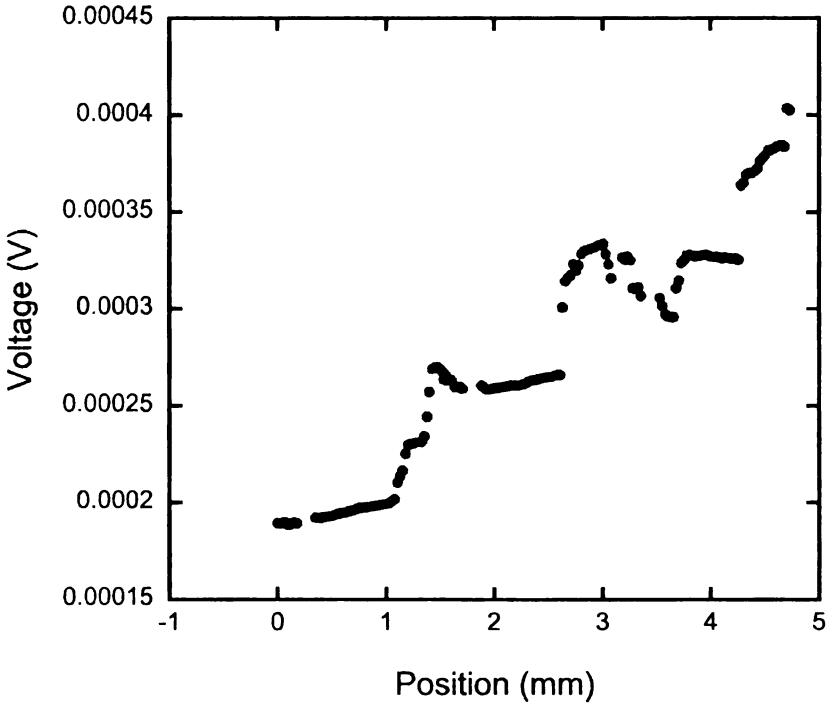

Figure 87: Voltage scan of LAST bonded to a SnFeTe alloy.

As shown in Figure 87 the LAST material properties have changed. During the bonding process, the iron, tin, and tellurium may have diffused and/or reacted with the thermoelectric material causing the electrical properties to change [71].

4.6 Diffusion Bonds of Bi_2Te_3 to LAST and LASTT Materials

For higher efficiency devices, segmentation of the LAST and LASTT material with Bi_2Te_3 can be used. A direct bonding attempt of LAST to Bi_2Te_3 was investigated using a ramp time of 30 minutes and a soak time of 4 hours at a temperature of 450°C. The furnace pressure was set to 400 Torr of an Ar/H_2

atmosphere. The result of the experiment showed the LAST did not bond to the Bi_2Te_3. This may be due to CTE mismatch between the two materials, not enough bonding time, or not high enough bonding temperature or some combination of these. The bonding temperature is limited to the melting point of the Bi_2Te_3, which is approximately 300°C lower than the melting point of LAST material.

A colleague in our laboratory, Dr. Chun-I Wu also investigated a solder bond between LAST material and Bi_2Te_3 using a lead-tin solder. Both the LAST and Bi_2Te_3 were nickel plated before soldering, and an excellent bond was formed as shown by the voltage scan in Figure 88. The room temperature ZT of the segmented leg was 0.144. Similarly, an excellent solder bond between Bi_2Te_3 and LASTT could be formed with the same process as shown in Figure 89.

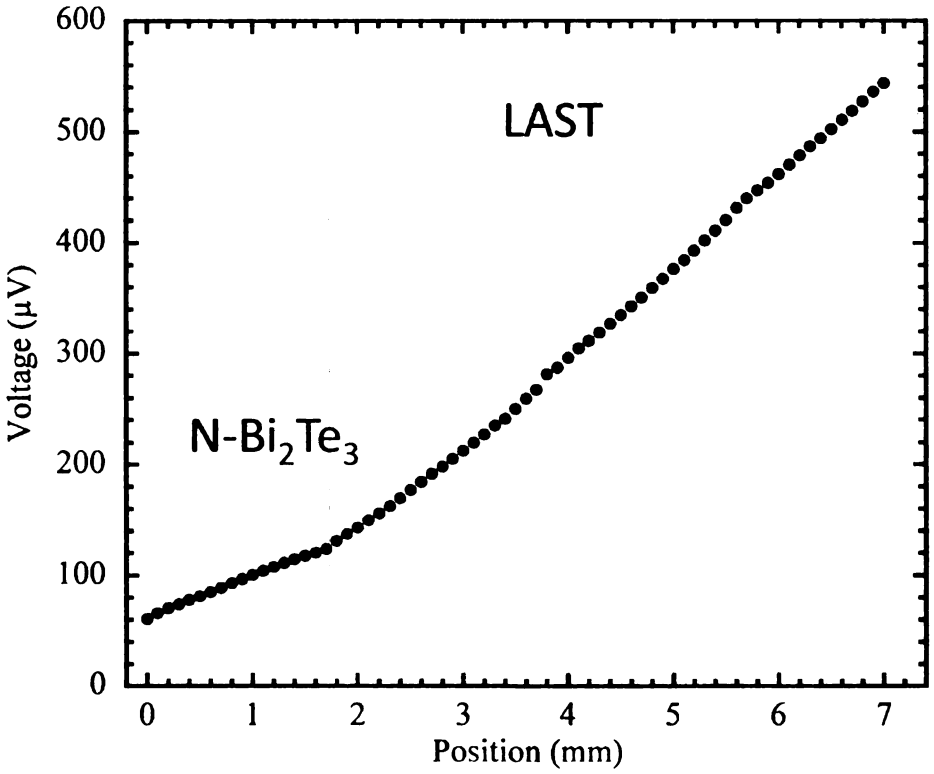

Figure 88: Segmented leg of LAST and Bi_2Te_3, measurement and data prepared by Dr. Chun-I Wu.

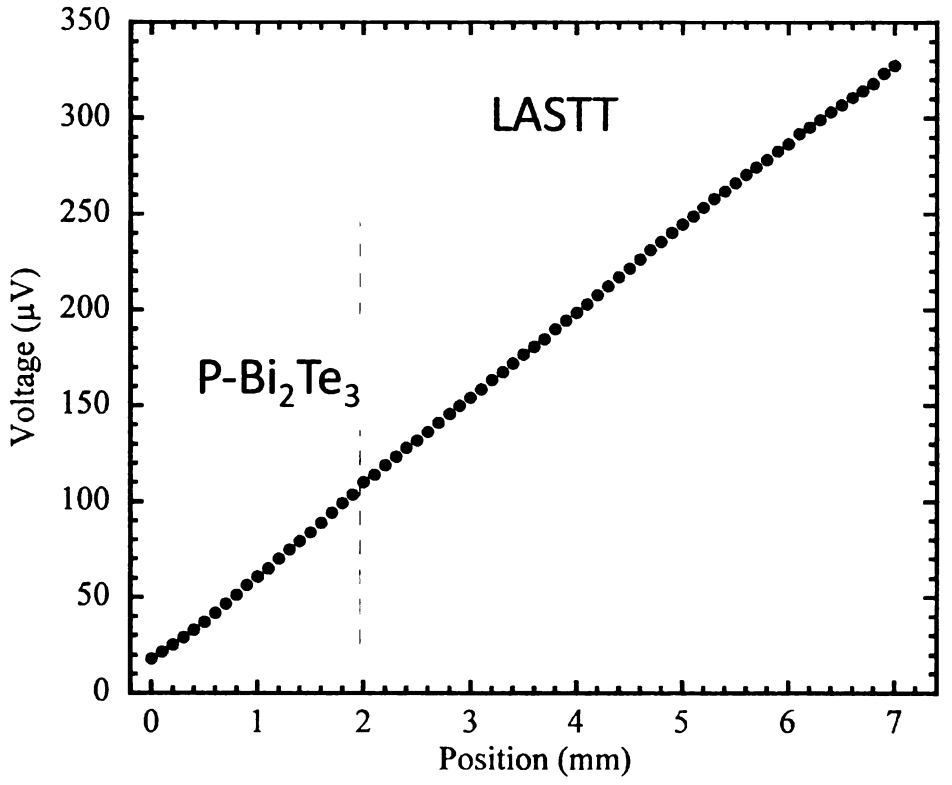

Figure 89: Segmented leg of LASTT and Bi2Te3, measurement and data prepared by Dr. Chun-I Wu.

The length of the Bi2Te3 in this case is only 2mm. The ideal length of the material is dependent on its properties and ZT may be maximized with adjusting the relative geometry of either the Bi2Te3 or the LAST.

A second attempt to bond Bi2Te3 to LAST at 450°C for 4 hours again resulted in no direct bonds as shown in Figure 90.

Figure 90: Picture of failed bonds of Bi_2Te_3 to the LAST material.

4.7 Diffusion Bonds of Chromium, Iron and Indium Layers Between Nickel and LAST and LASTT

This section describes bonding studies using pre-deposited layers of chromium and iron between the thermoelectric materials and a nickel metal electrode. A unicouple bonding run was done with a pre-deposition of chromium-iron onto n-type material. The bonding was done in two separate stages. Stage one bonding of the n-type material showed strong bonds. One of the samples exhibited melting indicating the formation of some eutectic during the bond. A contact scan of the LAST to the nickel is shown below.

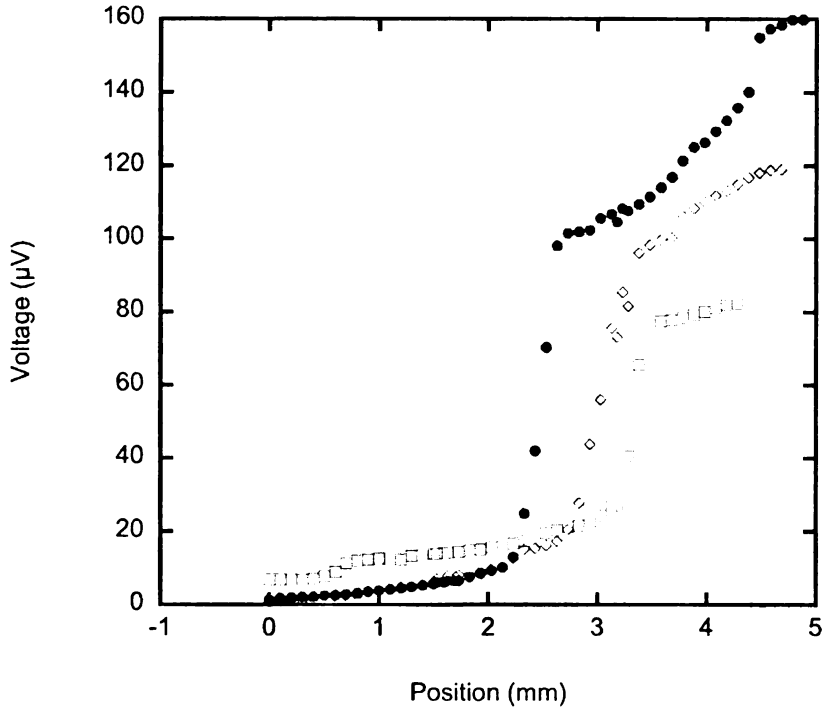

Figure 91: Nickel to LAST bond with a thin film of chromium-iron.

The contact scan shows a high contact resistance as seen in Figure 91 but also a change in the electrical conductivity of the LAST. Some of the chromium-iron film may have diffused into the LAST material causing a doping change of the material. The p-type material bonded well, but there was some deformation of the material. Room temperature ZT measurements gave values of 0.08, 0.05, and 0.05.

Unicouple run Q was a bond of ETP31 and ETN147 to an indium coated nickel electrode. The bond was done at 639°C for 10 minutes with a 2 hour ramp. Only the n-type material bonded.

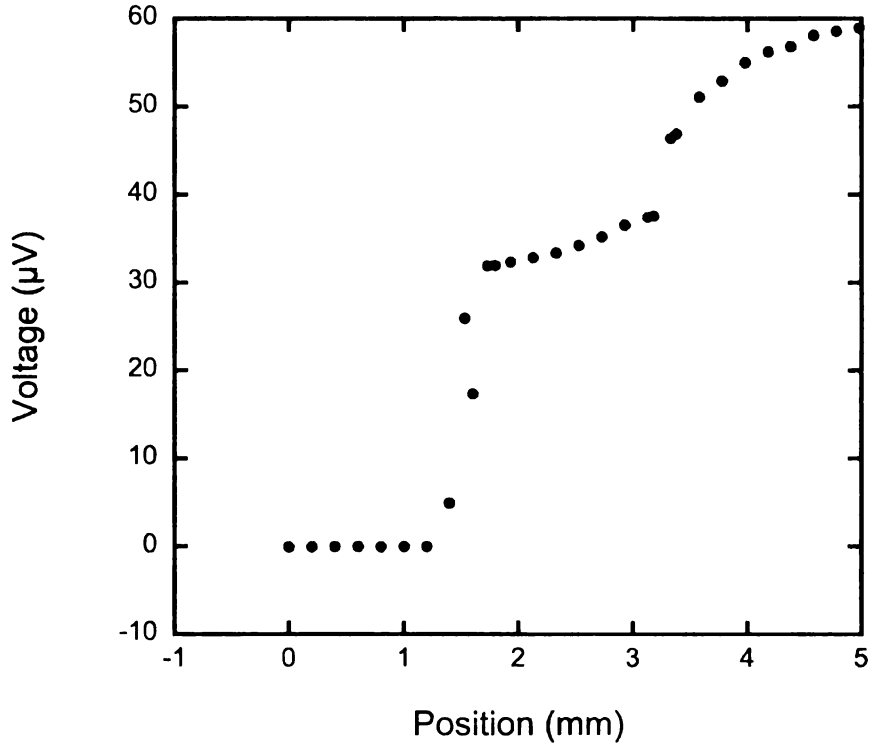

Figure 92: Contact scan of unicouple run Q.

Unicouple run R was a bond of p-type material directly to nickel. The bond was done at 725°C with a 4 hour ramp and a 4 hour soak. Only one of the legs bonded with a contact scan shown in Figure 93.

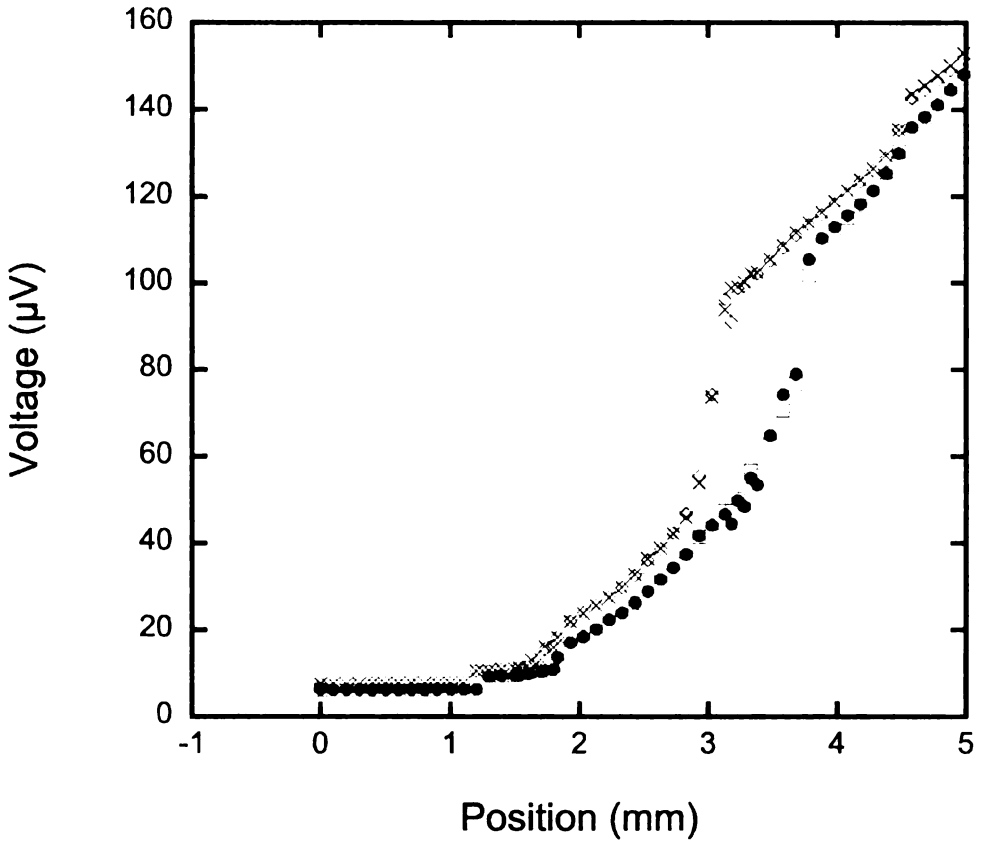

Figure 93: Unicouple run R contact scan.

Furnace run S was a repeat of run R, but with a 6 hour soak and the bonding temperature was 725°C. All of the legs bonded, but showed significant contact resistances as indicated in the scans shown in Figure 94.

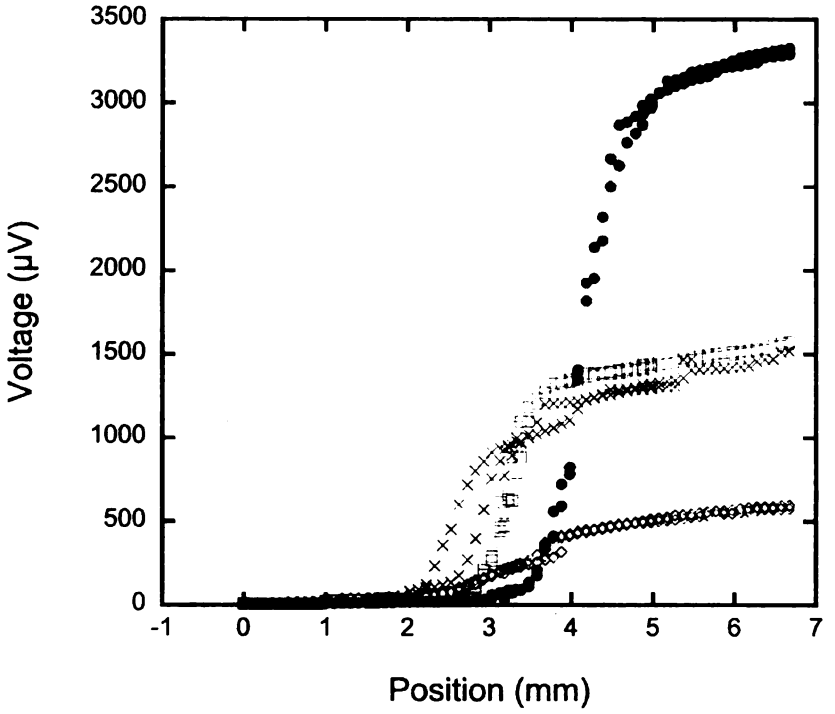

Figure 94: Scans of LASTT bonded directly to nickel.

The high bonding temperature combined with the long soak time may have allowed nickel to diffuse into the bulk material. The diffusion of nickel would change the properties of the LASTT material. The bond may be a mechanical success but does not work electrically.

Furnace run T was a bond of ETP26 directly to nickel but with a lower bonding temperature. The bond was done at 700°C with a 5 hour soak and a 4 hour ramp. Below shows the room temperature scan of the contact and there is some change in the electrical properties of the thermoelectric material in the first ~ 1.5mm near the junction. This could result from diffusion of nickel into the

thermoelectric material causing a doping effect, or causing a mechanical change in the material that results in significant cracking near the junction.

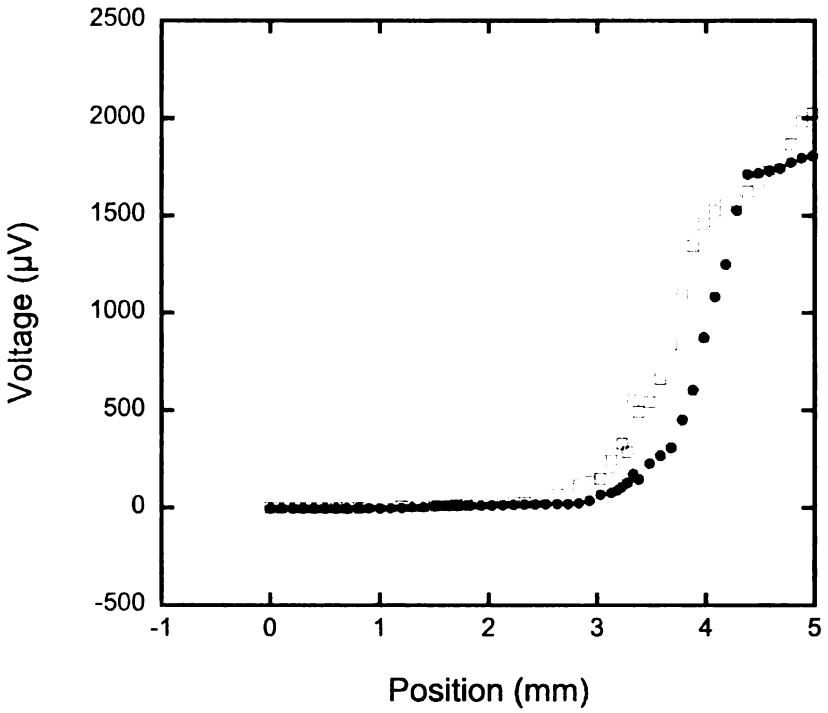

Figure 95: Contact scan of a bond from unicouple run T.

An experiment was done with an indium and gold deposition onto nickel to help prevent oxidization of the nickel before bonding runs. For this experiment ETN149 and ETP33 were used and 500nm of In and 150nm of gold was deposited onto the nickel. A 4 hour ramp and a 1 hour soak at 640°C was used. The experiment yielded no bonds. To test if the gold layer was inhibiting the bonding process, another experiment was done at a similar bonding temperature.

Unicouple run BD was a bonding run with a film of indium to bond the LAST to nickel in the configuration shown in Figure 96. The ramp time was 2.5 hours

with a soak temperature of 628°C for 1.5 hours. Both n-type and p-type materials were bonded in the same run.

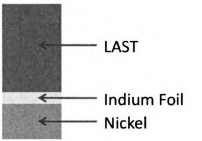

Figure 96: Experimental setup for bonding LAST/LASTT to nickel with an indium foil.

Unicouple run BE was a bond like before with ETN179 to nickel with an indium foil just like what is shown in Figure 96. The bond was done with a 30 minute ramp and a 1.5 hour soak at 628°C. Unicouples were fabricated and the contact resistance is shown below.

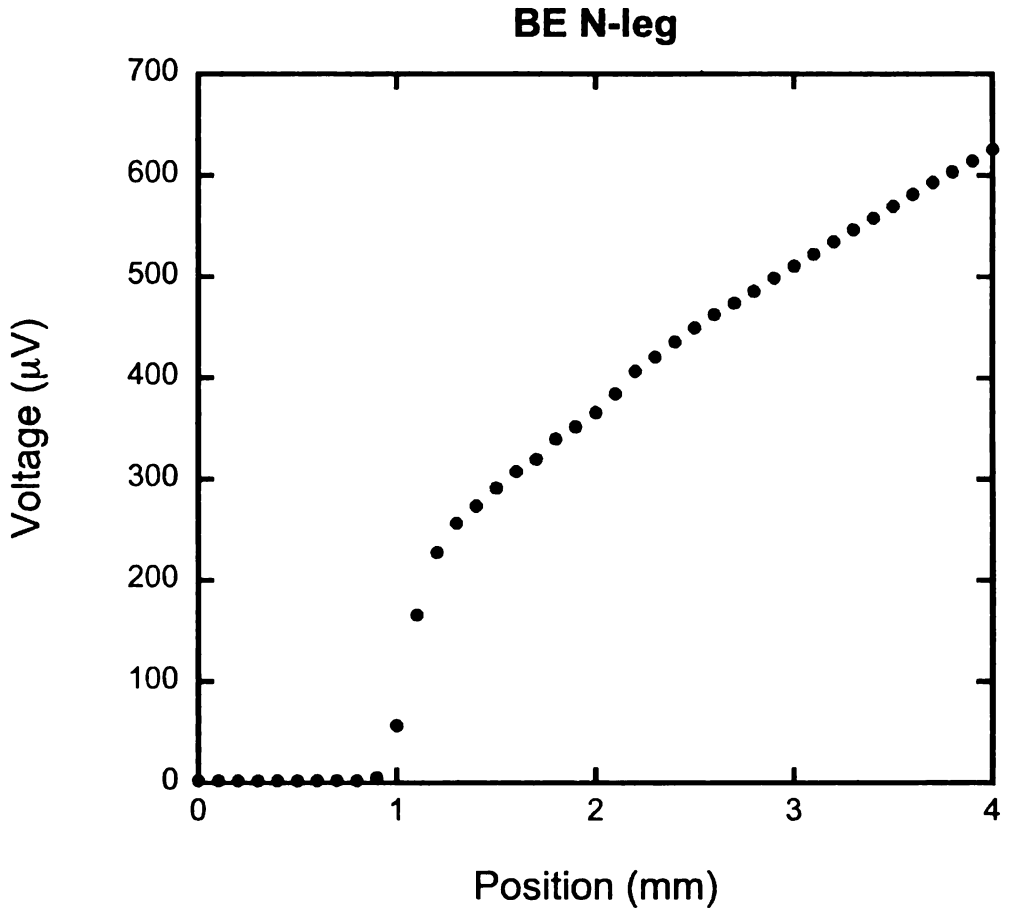

Figure 97: Contact scan of the n-type leg from unicouple run BE.

After trying to measure the module all of the bonds failed after several temperature cycles.

A bond of an iron-chromium alloy to ETN151 and ETP33 along with another nickel indium bond was done. One boat had 4 unicouples to be bonded with the iron-chromium alloy and the other boat had 4 unicouples to be bonded with indium to nickel. The bond was done with a 4 hour ramp and 4 hour soak at 700°C. Only one p-type leg bonded with the indium to the nickel, and only one bond with the iron-chromium alloy.

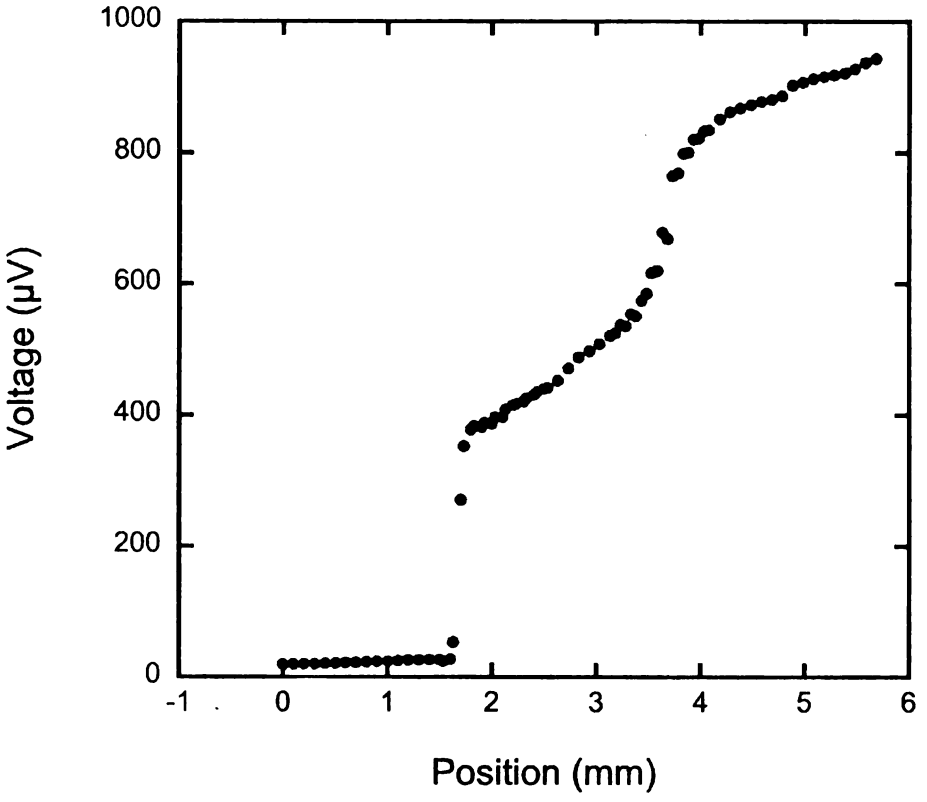

Figure 98: Voltage scan of the n-type leg to an iron-chromium alloy.

The bond between the iron-chromium has a high contact resistance and the scan shown in Figure 98 shows some non-linear regions possibly indicating cracks which are not parallel to the interface, or a distribution to the impurity concentration throughout the material.

Unicouple run AM was a bond of ETN171 to pure iron. Four samples were used and the bonding was done with a 30 minute ramp and 4 hour soak at 700°C. Unicouple run AM showed that the LAST material does not bond directly to pure iron under these conditions. There may have been an oxide layer on the iron that prevented bonding.

4.8 Diffusion Bonds of Copper Beryllium to LAST and LASTT Materials

Unicouple run Y was a bond of ETN149 and ETP33 to a copper beryllium alloy. The bond was done with a 4 hour ramp and a 5 hour soak at 700°C. During the bonding run the LAST and LASTT formed a eutectic with the copper beryllium and everything melted as shown in Figure 99.

Figure 99: Photo of the failed diffusion bond of LAST and LASTT to a copper beryllium alloy.

The use of a copper beryllium alloy for the electrode is attractive because of the relatively low electrical conductivity, relatively close matching of the coefficient of thermal expansion with LAST and LASTT, and the availability of such alloys. The use of copper beryllium alloys however, would require a suitable diffusion barrier to prevent the eutectic formation. To that end, an electron beam deposition of 75.1nm of tungsten followed by 60nm of gold on the copper beryllium interconnects was studied. A quartz crystal monitor was used to monitor film thickness during the deposition process.

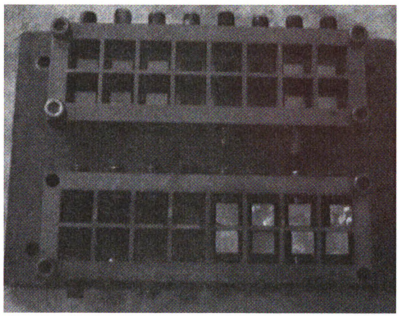

Figure 100: Setup of the legs before the deposition of W and Au.

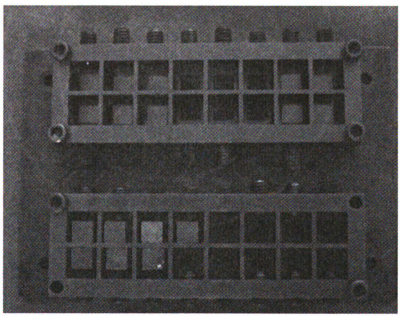

Figure 101: Picture of setup after deposition with gold coating.

The bond was done at 700°C with a 4 hour ramp and 2 hour soak. A comparison of Figure 99and Figure 102 does show a reduction in the melting of the samples with the diffusion barrier, however it was not sufficient for the prevention of the eutectic formation.

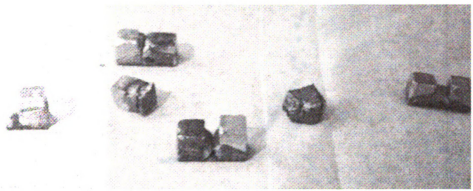

Figure 102: Results of bonding experiment after adding gold and tungsten to the copper beryllium alloy.

4.9 Diffusion Bonds of 316 Stainless Steel to LAST and LASTT Materials

Unicouple run AA was a bond of ETN151 and ETP28 to 316 stainless steel. The 316 stainless used has a thickness of 0.18" to reduce the resistance of the interconnect. The bond was done in two stages; 30 minute ramp for the n-type bond and a 4 hour ramp for the p-type bond. Both stages had a soak time of 5 hours at 700°C and 4 out of 5 unicouples bonded. The room temperature ZT of one of the unicouples was 0.104 with a room temperature resistance below 5mΩ. These results were among the highest ZT and lowest resistance of any unicouple studied in this research.

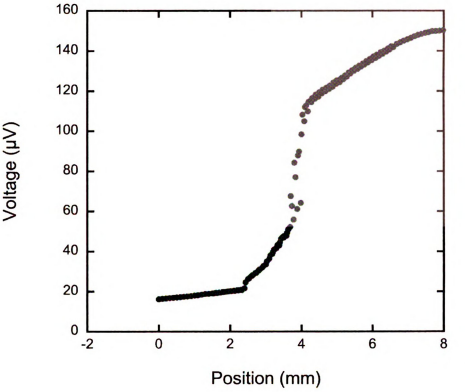

Figure 103: Unicouple run AA N leg scan.

As shown in Figure 103 the n-type leg looks to have a crack in the center of the leg, but still the overall unicouple resistance was below 5mΩ.

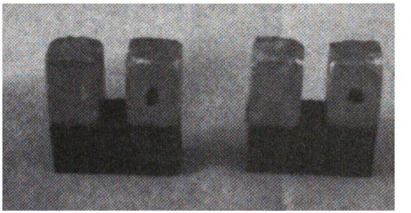

Figure 104: Unicouples for run AA.

Unicouple run AB was a bond of ETN153 and ETP28 to 316 stainless steel and was done to investigate the repeatability of the results from unicouple run AA.

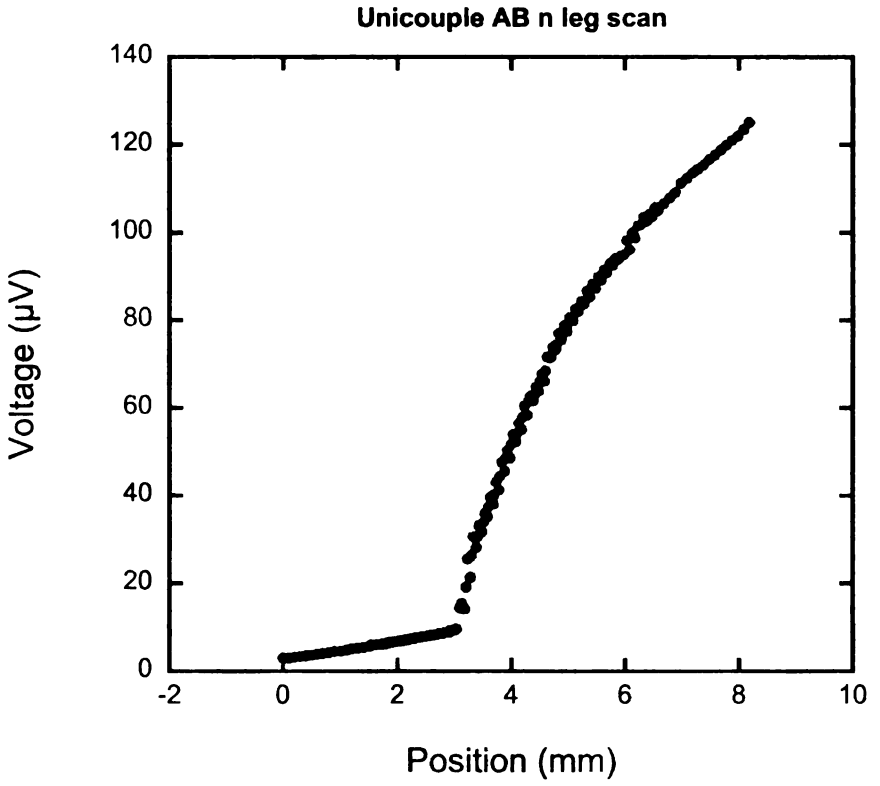

Figure 105: Unicouple run AB N leg scan.

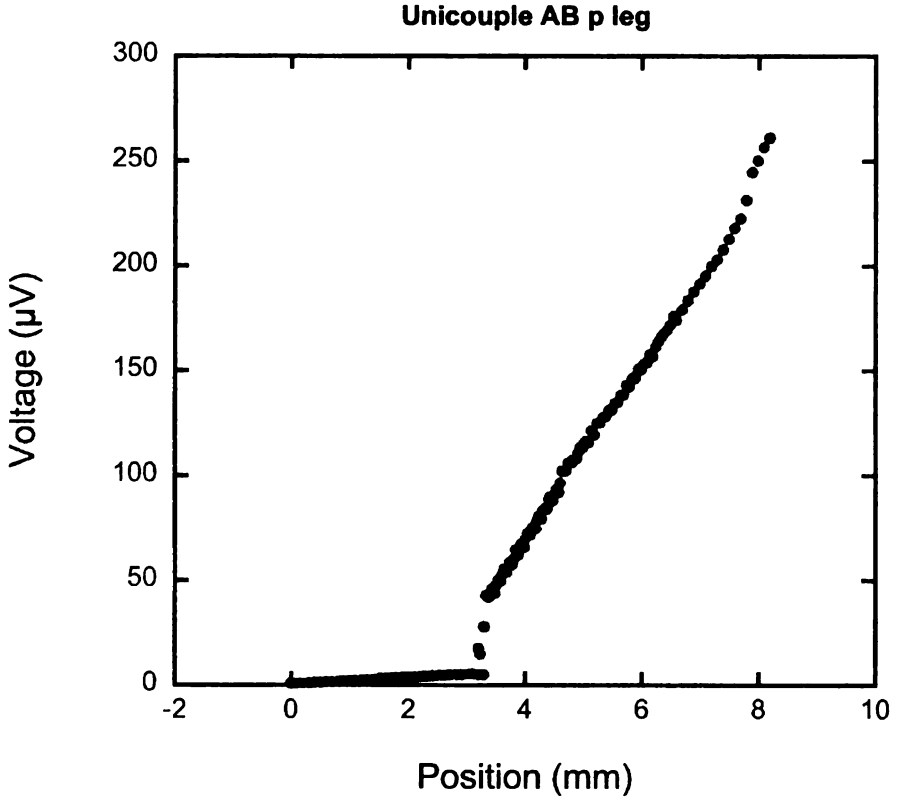

Figure 106: Unicouple AB P leg scan.

The scans shown in Figure 105 and Figure 106 show low contact resistances once again for the bonding of LAST and LASTT to 316 stainless steel.

Unicouple run AC was a bond of ETN153 and ETP28 to 316 stainless steel. The two stage run was used as before but this time the soak time was 6 hours at a temperature of 700°C. The experiment was used to see how a longer soak time would affect bonding results.

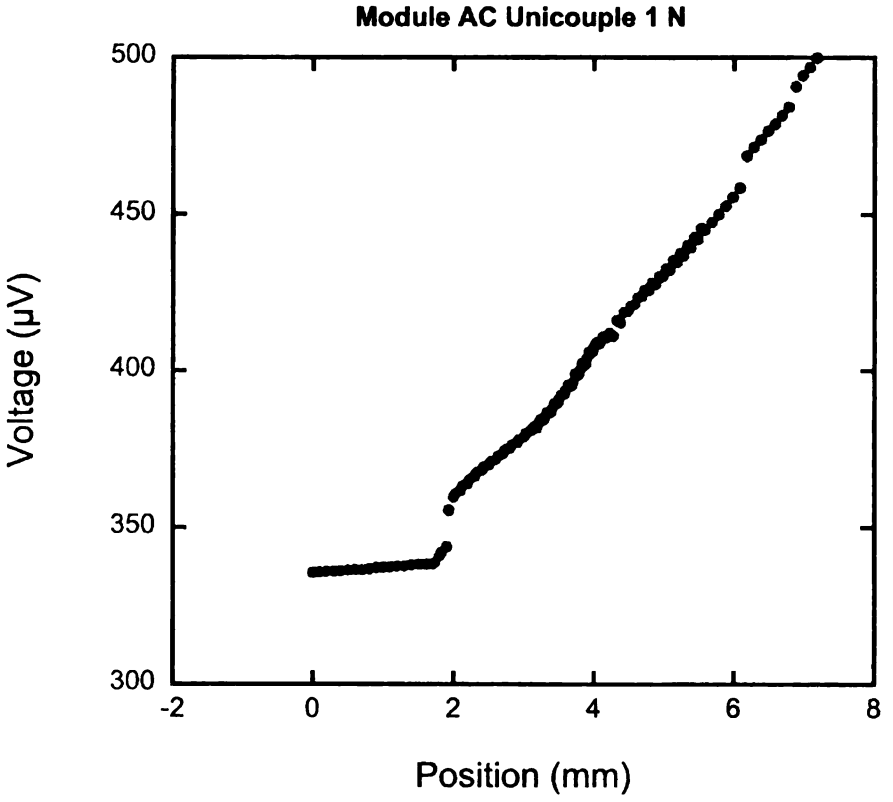

Figure 107: Unicouple Run AC N leg scan.

Figure 107 shows a contact scan of the n-type leg of one of the unicouples from bonding run AC. The contact resistance is below $20\mu\Omega cm^2$, and there are no cracks along the length of the sample. Below is a scan of a p-type leg from the same unicouple which shows a contact resistance near zero and the leg has no cracks.

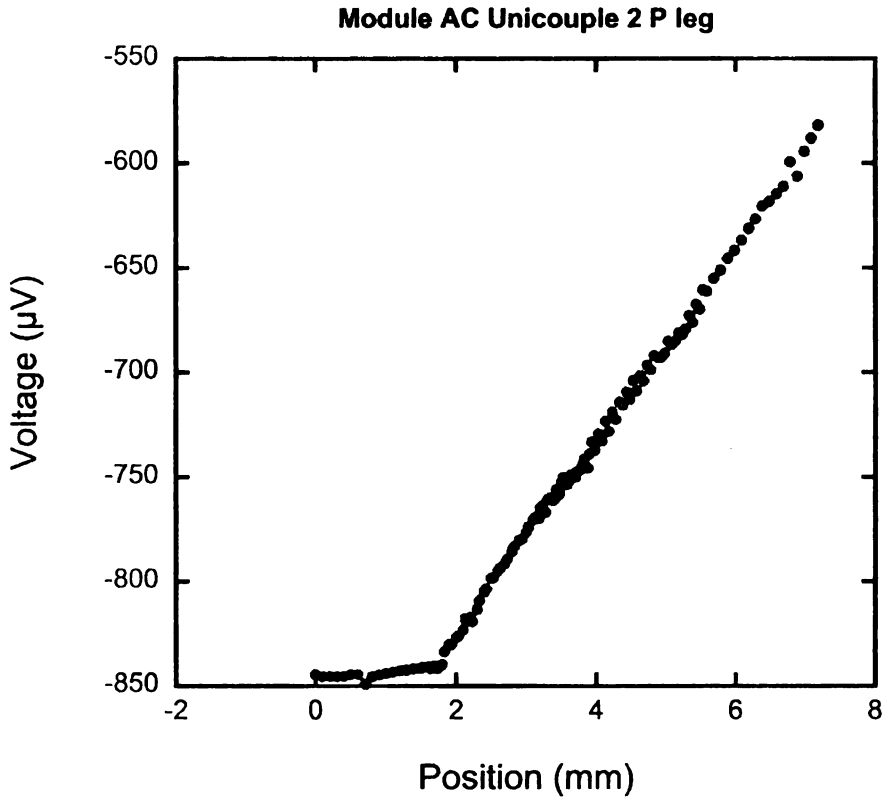

Figure 108: Unicouple AC P leg scan.

Two unicouples from run AC were put into a 4 leg module. The room temperature ZT of the four leg module was 0.039. The individual unicouple ZT's were not measured.

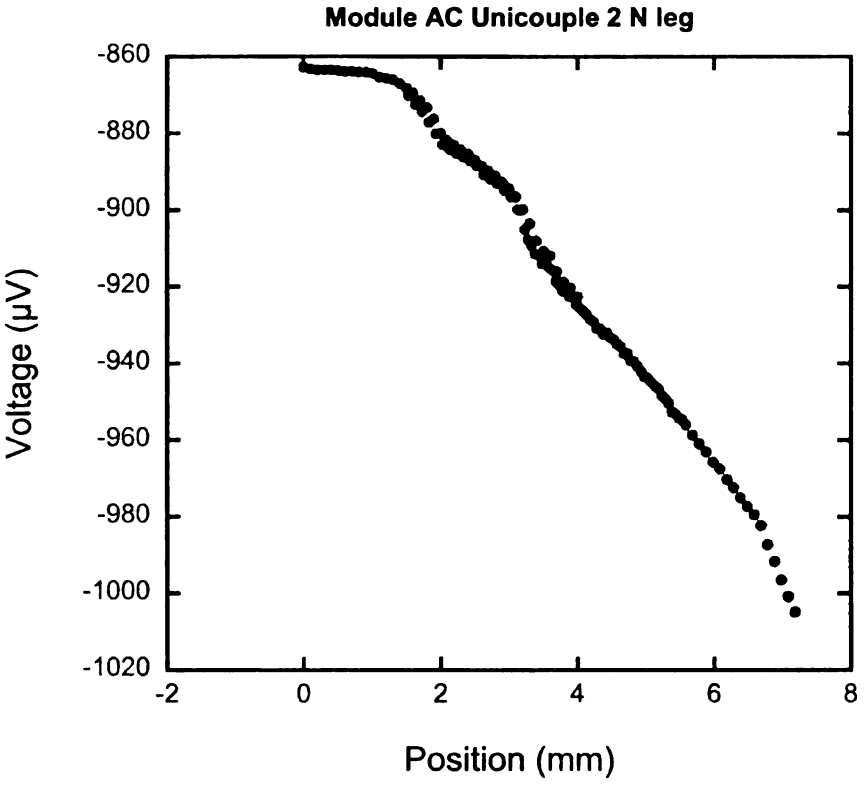

Figure 109: Unicouple 2 from AC run N leg scan.

Unicouple AC-2 had a room temperature ZT of 0.06.

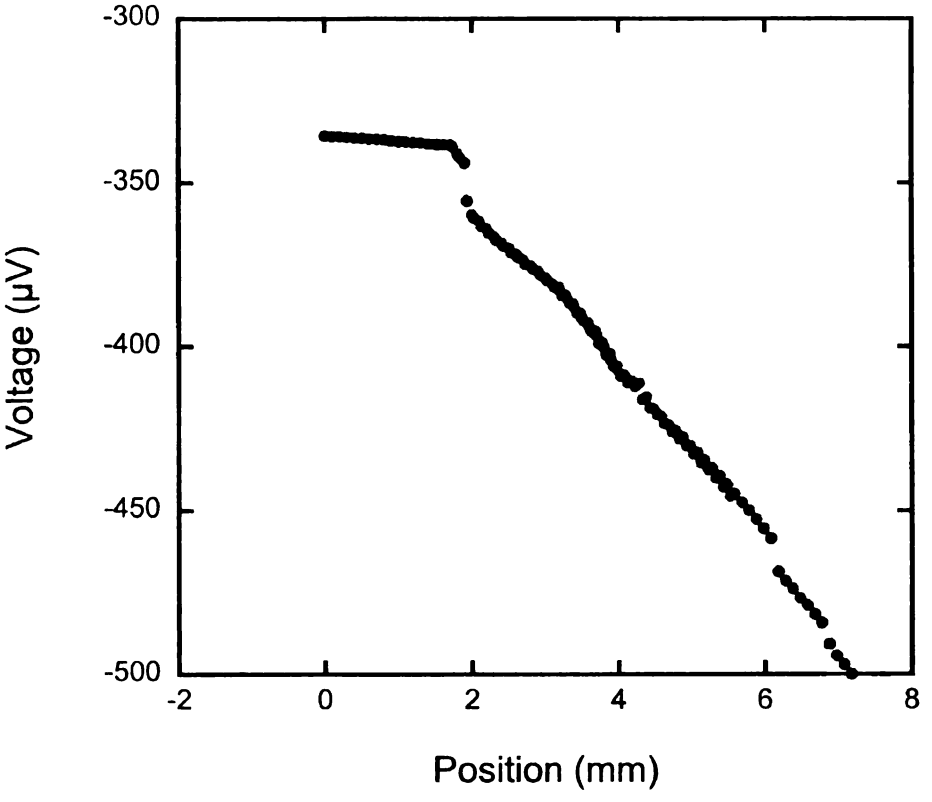

Figure 110: N leg scan from a unicouple run AC.

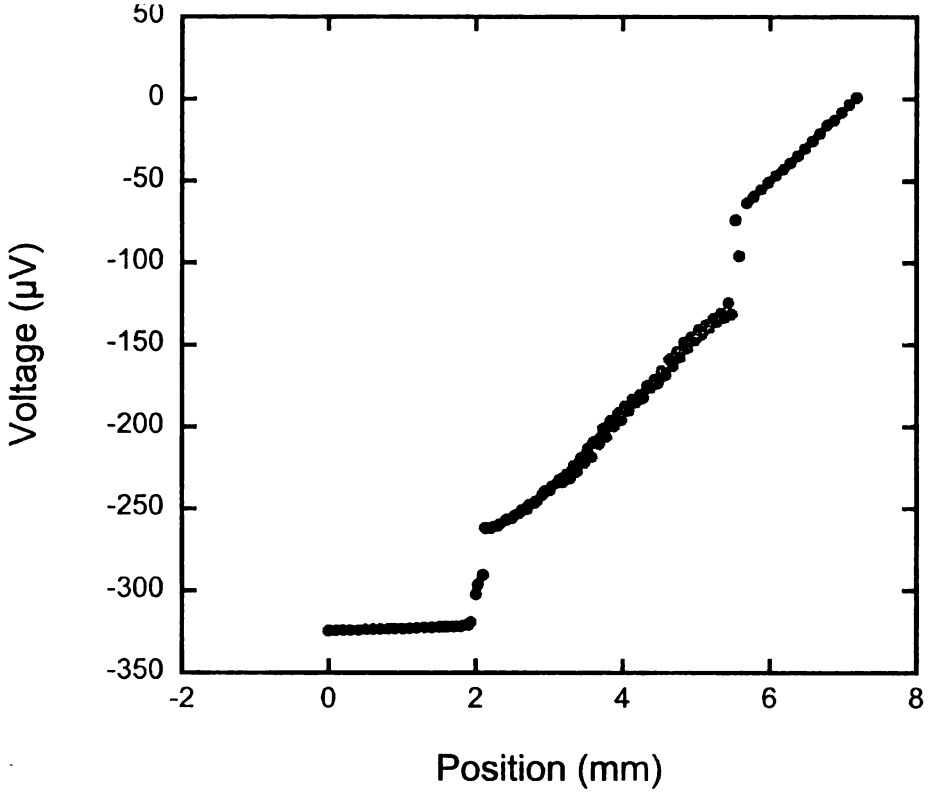

Figure 111: P leg scan from unicouple run AC.

Figure 111 is a scan of a p leg from a unicouple made in run AC. As shown in the contact scans, many of the legs from this bonding run did exhibit cracks.

Unicouple run AD was a bond of ETN156, slow cooled material, to 316 stainless steel. A two stage run was used with a soak time of 700°C for 6 hours.

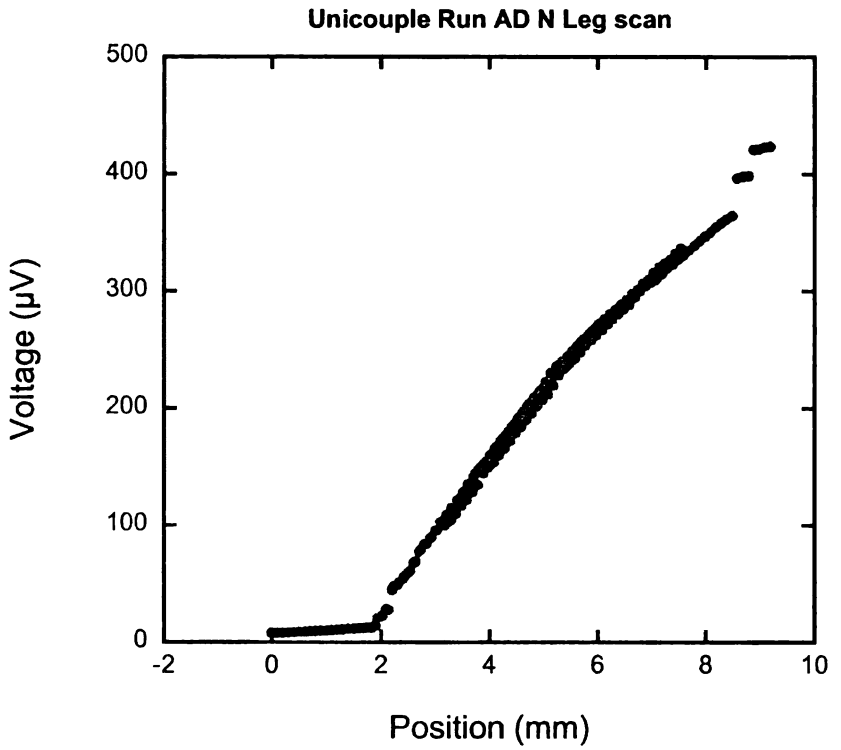

Figure 112: Unicouple run AD N leg scan.

This result shows the slow cooled material bonds well to the 316 stainless steel.

Unicouple run AE was a bond of ETN153 and ETP28 to 316 stainless steel. The stainless steel strips were cut to 1mm thick. The bond was a two stage bond at 700°C for 6 hours, however only one unicouple bonded.

For a more intimate interface between the stainless steel and the thermoelectric material, 500 nm of 316 stainless steel was sputtered onto LAST and LASTT.

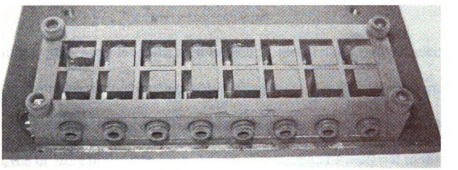

Figure 113: Module legs after a sputtering deposition of 316 stainless steel.

The sputtering of the stainless steel was done for 30 minutes. One of these legs was then soldered to copper to test the contact resistance as shown in Figure 114.

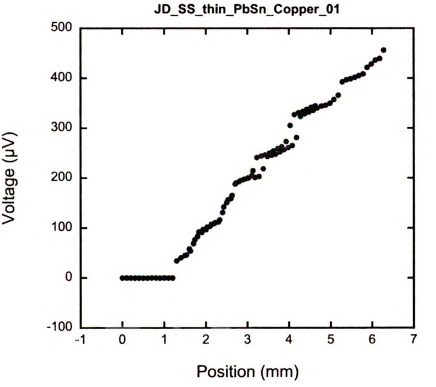

Figure 114: Scan of copper soldered to LAST with a thin film of 316 sputtered to the LAST.

These stainless steel samples were then brazed to nickel plated copper electrodes, however the samples melted during the brazing process. A XXX nm thick stainless steel layer (5 hour sputtering of 316 stainless steel) was also investigated , however as before, the brazing of the legs caused the LAST and LASTT material to melt. In addition, some of the XXX nm 316 stainless steel coated legs were first annealed at 700°C for six hours and then brazed to the nickel plated copper. Once again all of the samples melted during the brazing process.

Unicouple run AF was a bond of ENT154 to a 0.02" thick 316 stainless steel foil. A 30 minute ramp and a 6 hour soak at 700°C was used. Stage one of the bond was a success. A 200μm layer of braze was placed on top of the stainless steel layer and then bonded to nickel at 700°C for 90 minutes. The nickel brazed to the stainless steel without forming a eutectic with the LAST. Below is a scan of the nickel-316 stainless-LAST bond.

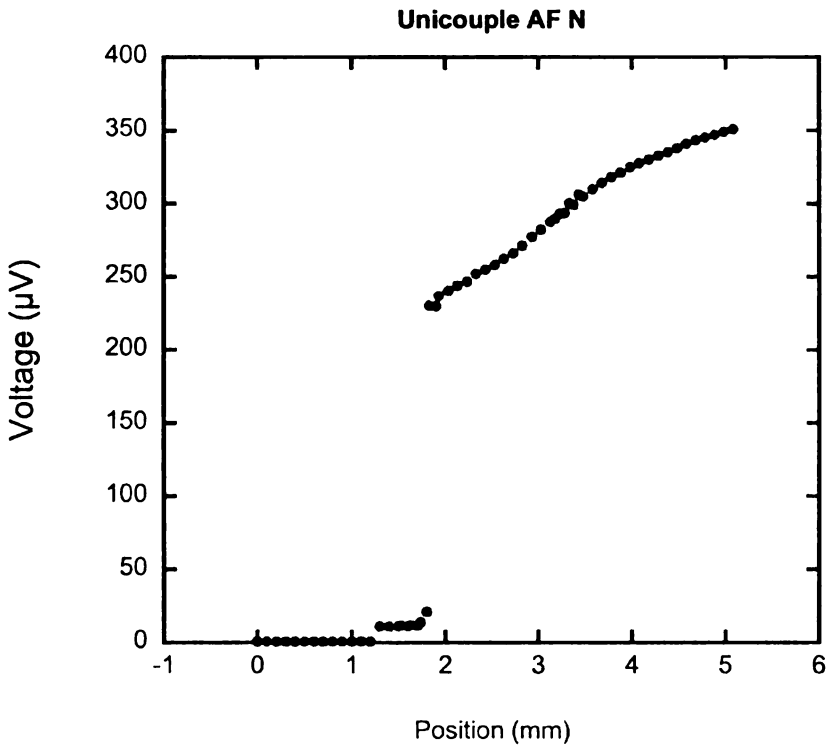

Figure 115: Scan of Ni-316-LAST bond.

As shown in Figure 115 there is significant contact resistance between the stainless steel and the LAST material. This may have occurred after the brazing of the nickel to the stainless steel, possibly caused by CTE mismatches among the materials used..

The bonding conditions for unicouple AG were a repeat of those used in run AF and 8 out of 8 unicouples bonded.

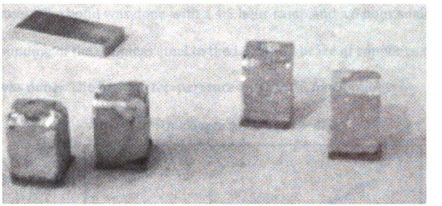

Figure 116: Bonds of 0.02" thick 316 stainless steel to LAST material.

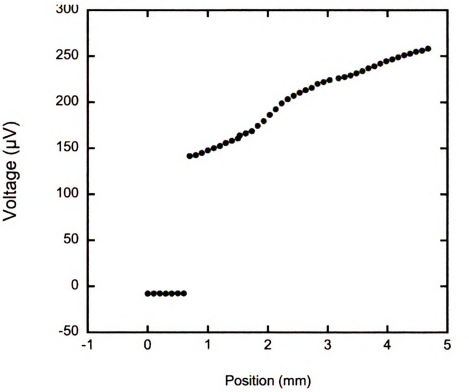

Figure 117: Scan of unicouple run AG N leg to 316.

Once again the large voltage discontinuity is shown between the LAST and 316 stainless steel. Thus the large contact resistance was not caused by cracking during the brazing step. Unicouple run AH was a bond of 6 p-types to 0.02" thick 316

stainless steel. The bond was done with a 4.5 hour ramp and a 6 hour soak at 700°C. After the bonding of the stainless steel to the LAST and braze of copper to the 316 stainless was done. The brazing temperature was 700°C for 90minutes.

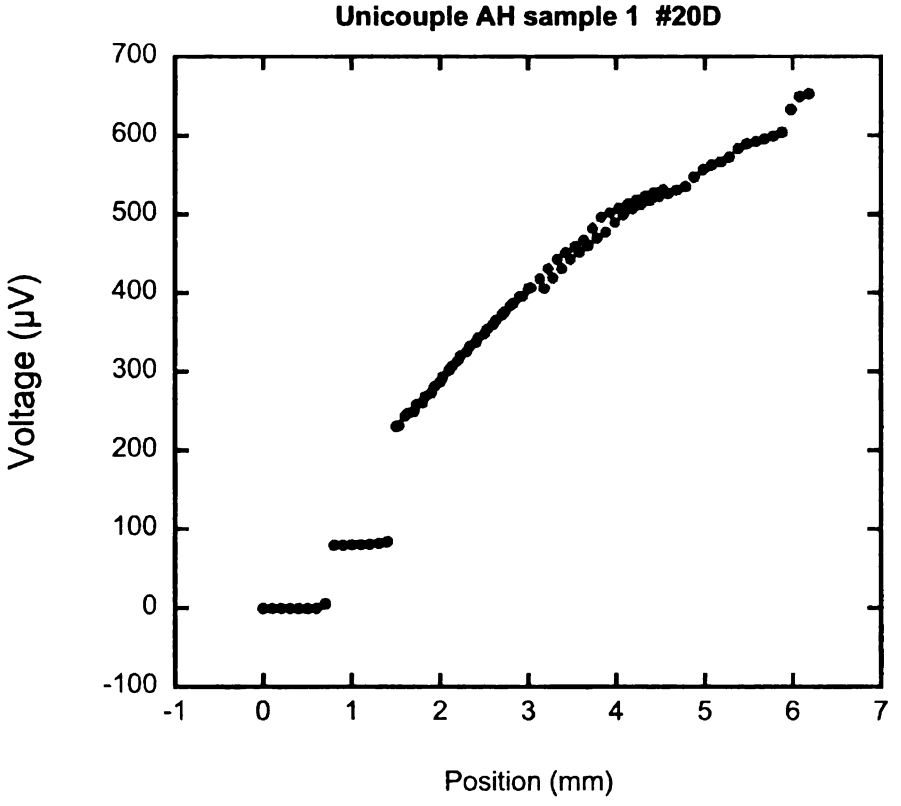

Figure 118 Scan of Cu-316-LASTT bond

After the scan was finished, the LASTT cracked off of the 316 stainless. Also shown from the contact scan in Figure 118 the contact resistance is high. The 0.02" stainless steel is not a good contact to either LAST or LASTT.

Unicouple run AI was a bond of 0.02" thick 316 stainless steel to n-type LAST. The 316 surface was roughened before bonding to create more bonding surface area. The samples bonded to the rough surfaces, but after brazing all of the samples melted.

Since previous experiments (name the unicouple runs) showed low contact resistances, the processing conditions for fabrication of 316 stainless steel foil versus 316 stainless steel bulk materials was questioned. The 0.5mm 316 stainless steel may not be formed the same way as the thicker, 4.6mm, stainless steel. The different casting techniques of the stainless may change the properties of the diffusion bonded LAST to 316.Unicouple run AJ was a bond of 4.6mm thick 316 stainless steel to a hot pressed sample made from powder of ETN154. A 30 minute ramp and 6.5 hour soak at 700°C was used. All bonds attempted were successful.

Scans of legs before bonding were done and then the legs were placed into the furnace for bonding and then scanned again. The bond was done with a 30 minute ramp and 6.5 hour soak at 700°C.

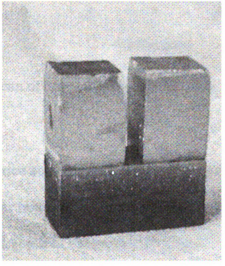

Figure 119: Picture of bonded hot pressed module.

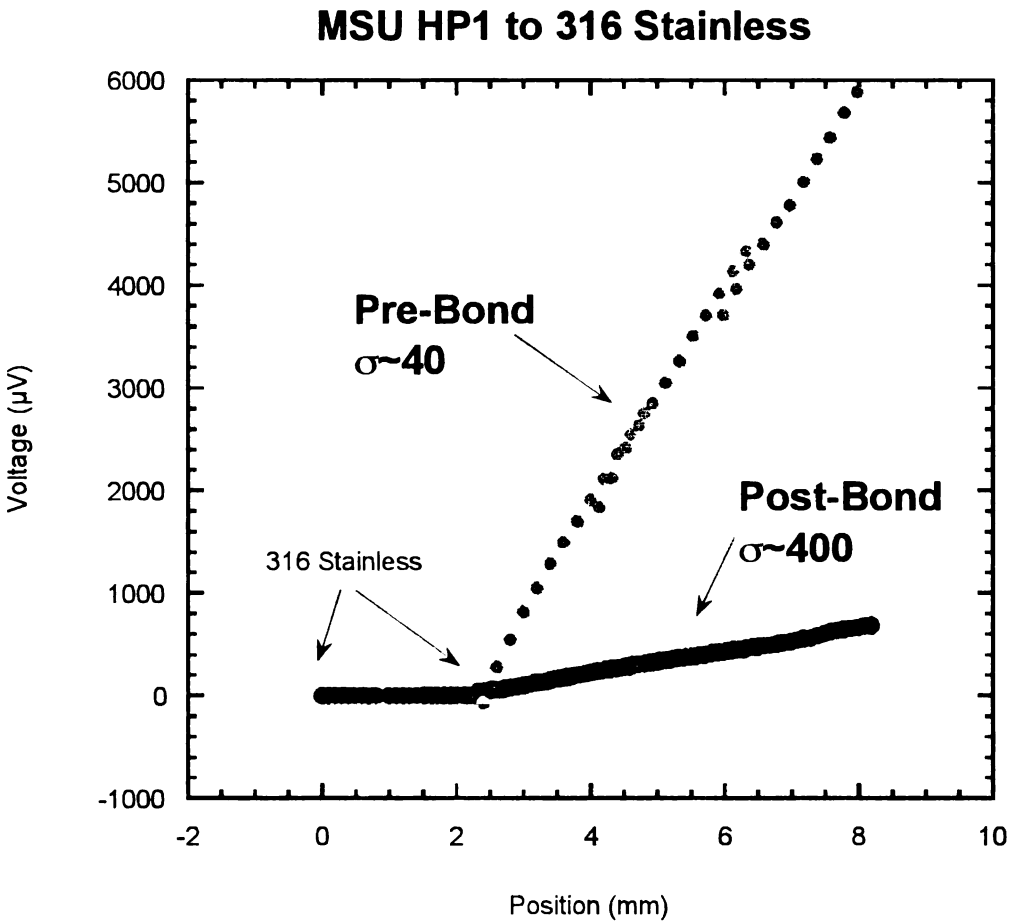

Figure 120: Scan of hot pressed leg before and after bonding.

Figure 120**Error! Reference source not found.** shows how the conductivity increased by 10 times after bonding. After scanning the sample it was broken intentionally to test the strength of the mechanical bond.

Figure 121: Fractured legs bonded to 316 stainless steel.

Breaking of the bonds was not easy, in-fact the leg fractured before the bond. After the leg fractured approximately 80% of the bonded contact remained on the stainless steel for the p-type leg, and approximately 30% of the n-type leg remained bonded to the stainless steel.

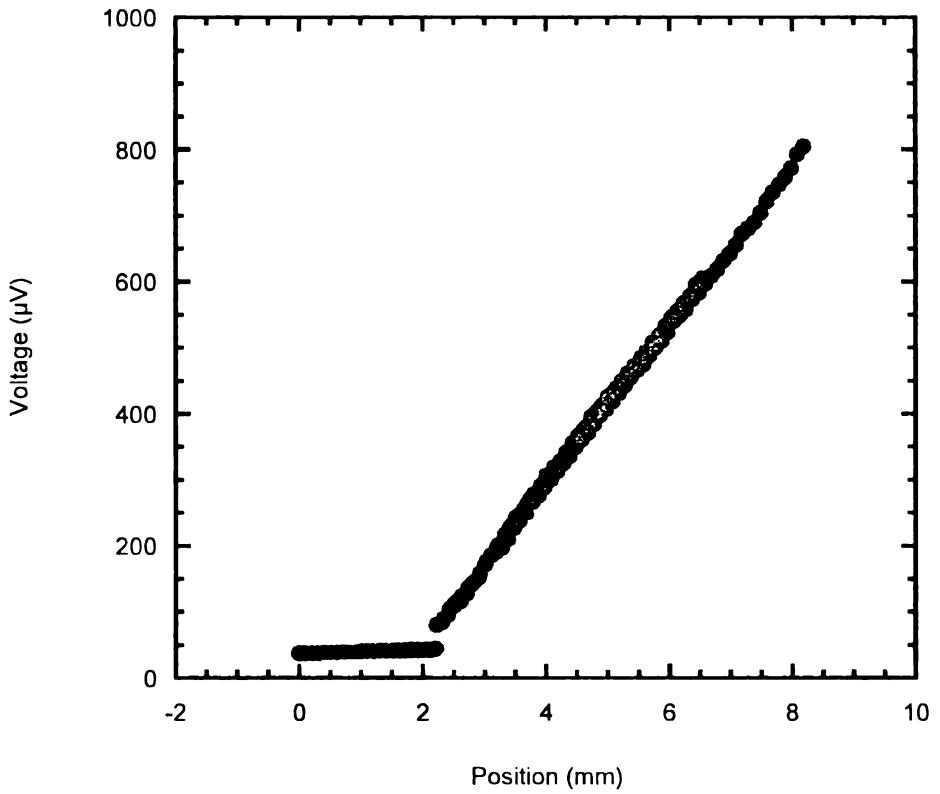

Figure 122: Scan of P leg contact to 316 stainless steel.

The contact resistance in Figure 122 is approximately 19μΩcm^2. This was a scan from the p-type leg before it was cracked off in the bond strength test. A second unicouple was scanned and had a higher contact resistance, 87μΩcm^2. When it was cracked only about 40% of the material remained bonded as shown in Figure 124.

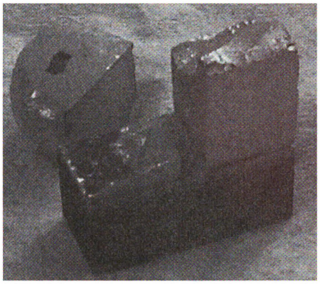

Figure 123: Crack of leg with high contact resistance.

Unicouple run AK was a bond of ETN164, EETP38, and 0.18" thick 316 stainless steel. This was done in a two stage bond. Stage 1 was a 30 minute ramp, and 6.5 hour soak at 700°C for bonding the n-type leg to the stainless steel. Stage 2 added the p-type leg using a 4 hour ramp and 6 hour soak at 700°C. Only 3 modules bonded. This could be a direct result of non-uniform mechanical pressure on the individual legs during bonding.

Run AL was a bond of MSUHP4, p-type hot pressed material, to 316 stainless steel. A 4 hour ramp, 6 hour soak at 700°C was used. The bond results showed that the p-type hot pressed material bloated about 10-15% larger than their original volume, but still bonded. Below is a scan of the contact resistance.

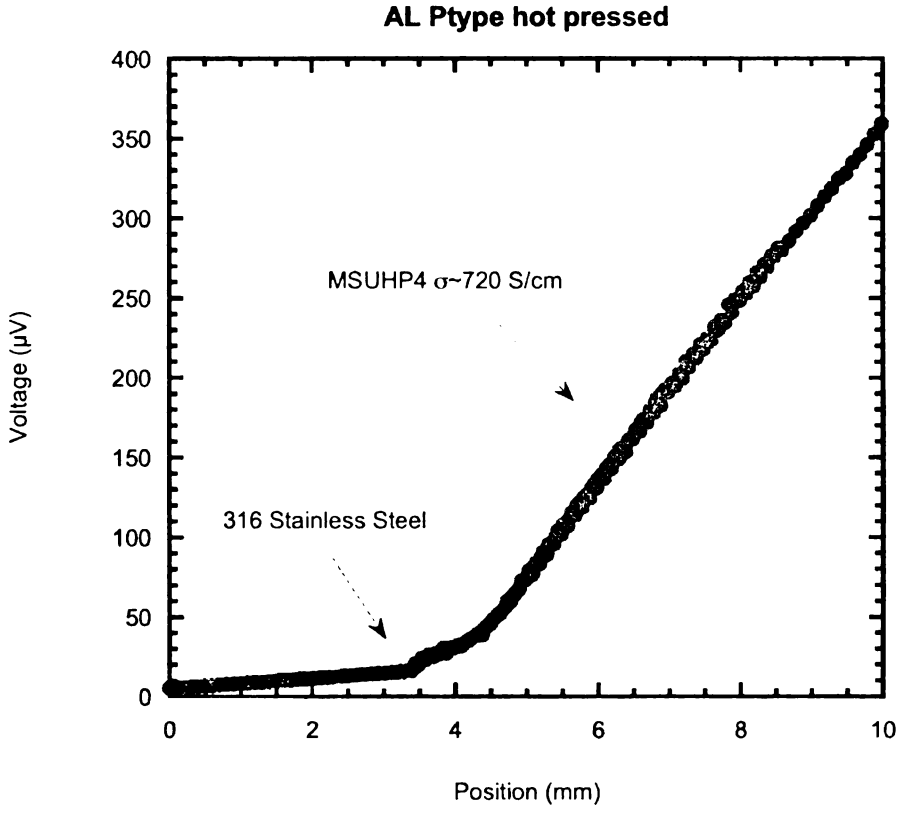

Figure 124: Scan of p-type hot pressed material bonded to 316 stainless steel.

Figure 124 shows that the p-type hot pressed material makes a good contact to the 316 stainless steel.

Run AN was a bond of tin-tellurium coated 316 stainless steel to ETN171. A 30 minute ramp and 6 hour soak at 700°C was used. 2 out of 4 samples bonded. The two that bonded were strong mechanical bonds.

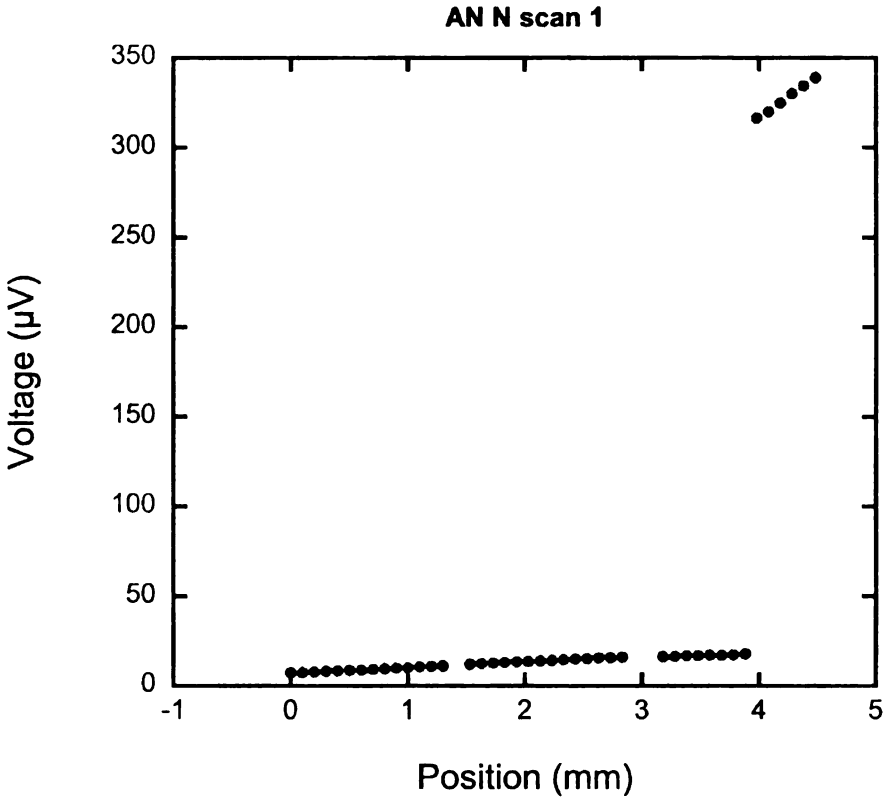

Figure 125: Scan of N leg bond to tin-tellurium coated 316 stainless steel.

The 316-LAST contact scan is shown in Figure 125 has a voltage jump over 275μV which is a contact resistance well above $20\mu\Omega\cdot cm^2$. This shows with an addition of tin-tellurium to the contact surface increases the contact resistance.

Unicouple run AO was a bond of MSUHP-2 to 0.02" thick 316 stainless steel. The bond was done with a 30 minute ramp and 6.5 hour soak at 700°C. The results of the run were bloated hot pressed legs and high contact resistance.

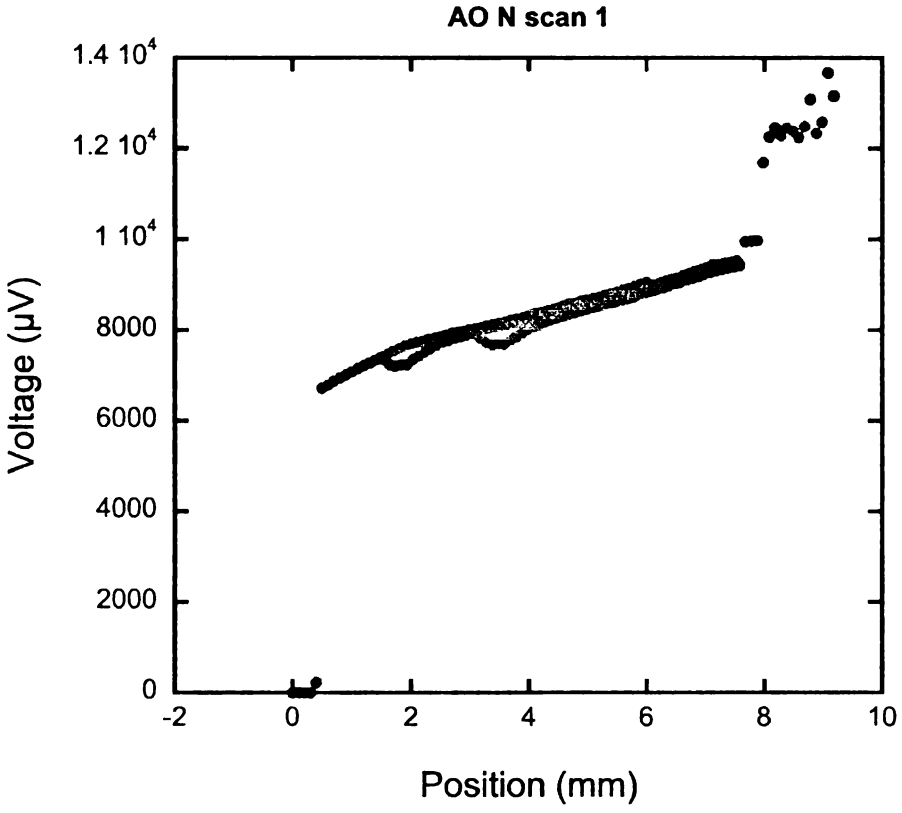

Figure 126: Scan of MSUHP-2 to 316 stainless steel.

Unicouple run AP was a bond of ETP38 to 0.02" thick 316 stainless steel. A 4 hour ramp with a 6.5 hour soak at 700°C was used. Two out of the 2 samples bonded, but exhibited high contact resistance as shown in Figure 126.

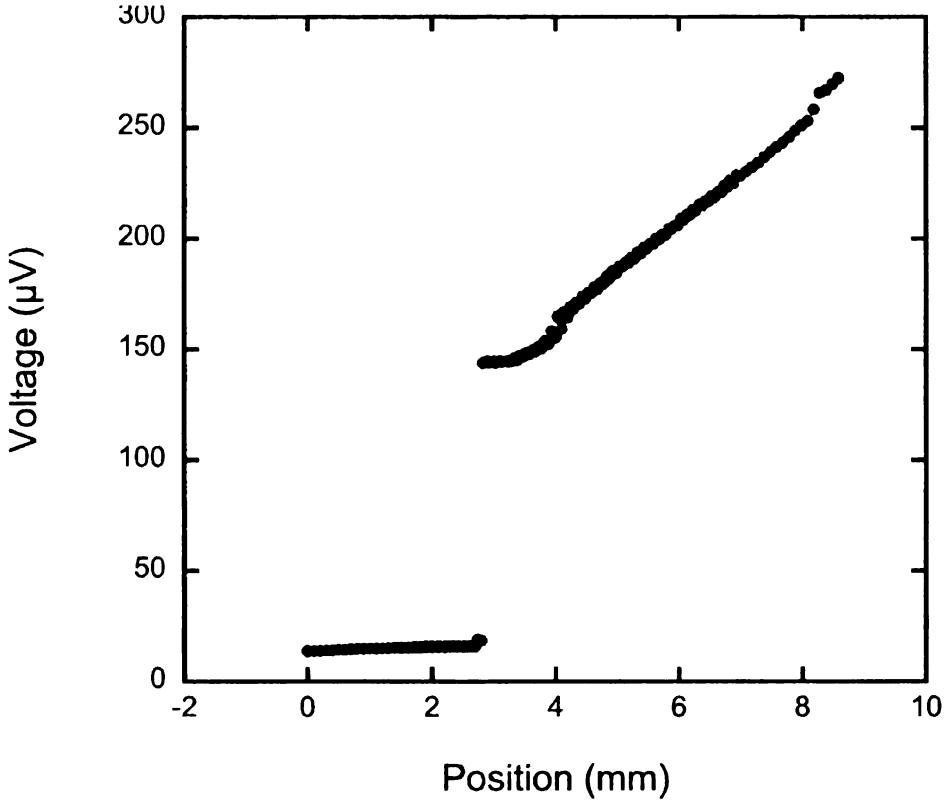

Figure 127: Contact scan of P leg to 0.02" stainless steel.

The contact resistance of the p-type LASTT to thin 316 stainless is around $200\mu\Omega\cdot cm^2$. This is too high for an efficient thermoelectric device.

Several results have shown that all of the bonds do not come out successful when other bonds from the same run do. This may be due to the fact that the individual mechanical bonding pressure from unicouple to unicouple may not be constant. A new bonding device was developed to individually monitor the mechanical pressure of each leg.

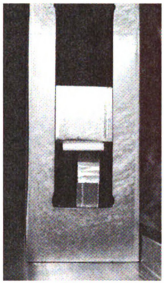

Figure 128: Photograph of new bonding device.

This bonding device bonds one leg at a time. A torque wrench was used to maintain better uniformity in the mechanical pressure used from leg to leg.

Unicouple run AQ was the first bonding run to use the new bonding device. The bond was ETP38 to 316 stainless steel. The bond was done with a 4 hour ramp and 6.5 hour soak at 700°C. The contact scan of the bond shows that it was a low resistance contact as seen in Figure 129.

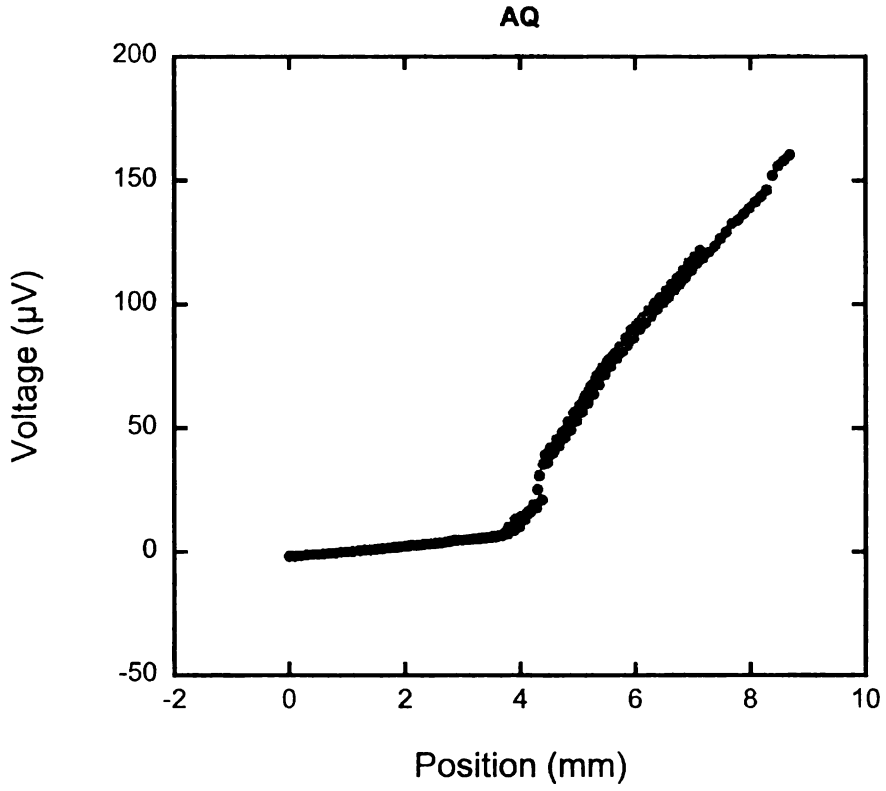

Figure 129: Scan of P leg bonded to 316 stainless steel with new bonding device.

The bonding procedure was repeated in unicouple run AT to fabricate many unicouples using the new bonding device. The two stage bonding technique was used and 26 total unicouples were bonded from the two runs.

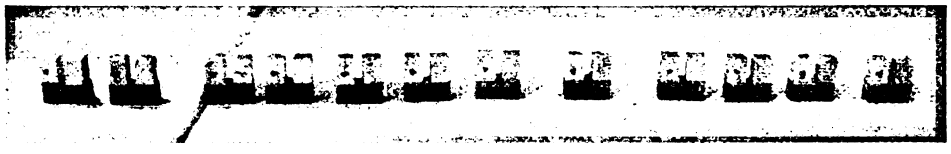

Figure 130: Unicouples bonded from runs AT and AS.

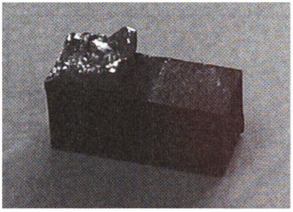

Figure 131: Fractured sample from run AT.

In Figure 131 is a picture of a fractured unicouple. The p-type leg fractured leaving material bonded to the stainless, however the n-type leg cracked off without leaving LAST material behind. The diffusion of the LAST may be slower than the LASTT and a longer bonding time may be necessary. To reduce the total resistance of the metal interconnect, unicouples from run AT were machined to have most of the stainless steel cut off, followed by a brazing of nickel plated copper to the electrode. Unfortunately all of the unicouples were destroyed during the machining step. The cut was done too close to the contact.

Unicouple run AV was a bond of 9 ETN174 samples to 316 stainless steel. The argon-hydrogen gas was flowing at 1 liter per minute with a chamber pressure of 770 Torr. A 30 minute ramp and 6.5 hour soak at 700°C was used. Below is a contact scan of a sample bonded in the run.

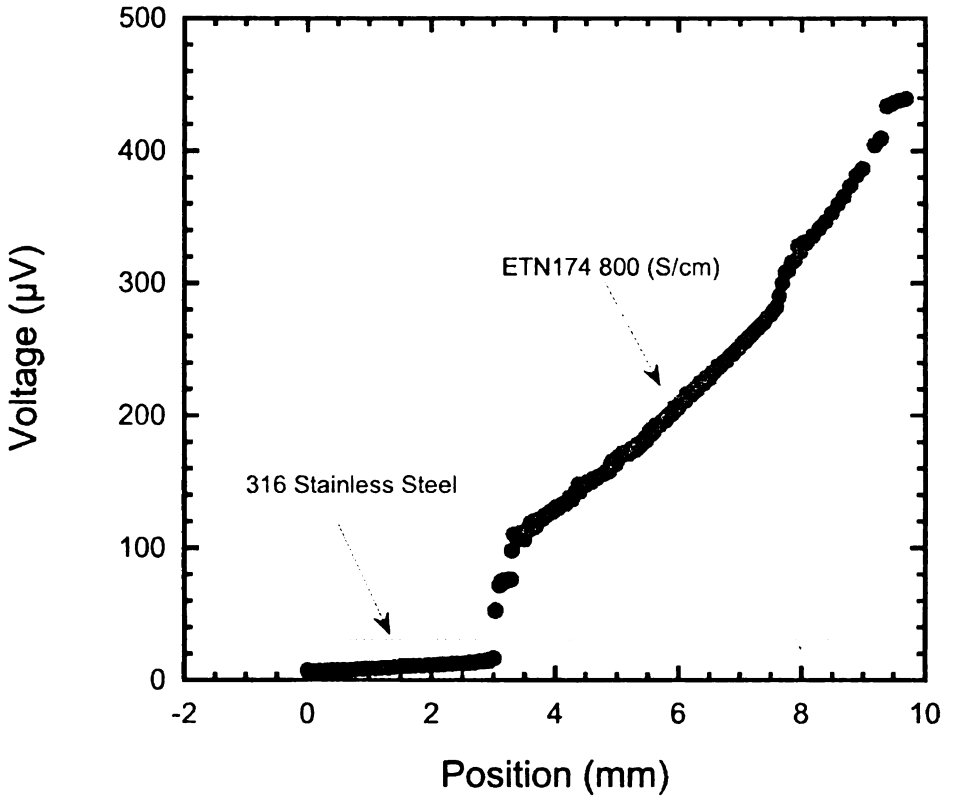

Figure 132: Scan of ETN174 bonded to 316 stainless steel. The horizontal line represents a contact resistance of $20\mu\Omega\cdot cm^2$.

Unicouple run AW was a bond of ETN173 and ETN174 to 316 stainless steel with a soak temperature of 800°C. The ramp time was 1 hour with a 6.5 hour soak. The higher soak temperature was used to see how it effects the bonding results. The higher bonding temperature did not melt the samples but they did change in color as seen in Figure 133.

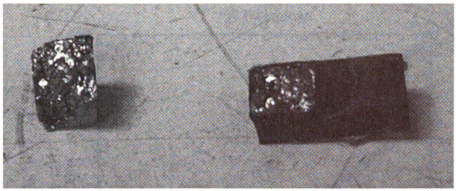

Figure 133: Photograph of bond of LAST to 316 with a soak temperature of 800°C.

Figure 133 shows how the material bonded to the 316 but then the leg cracked off while preparing the sample for a contact scan. Stage 2 of AW used samples of ETP40with a 4.5 hour ramp and 6.5 hour soak at 700°C. Only 3 total unicouples were fabricated from this bonding run. Future experiments would not use the soak temperature of 800°C.

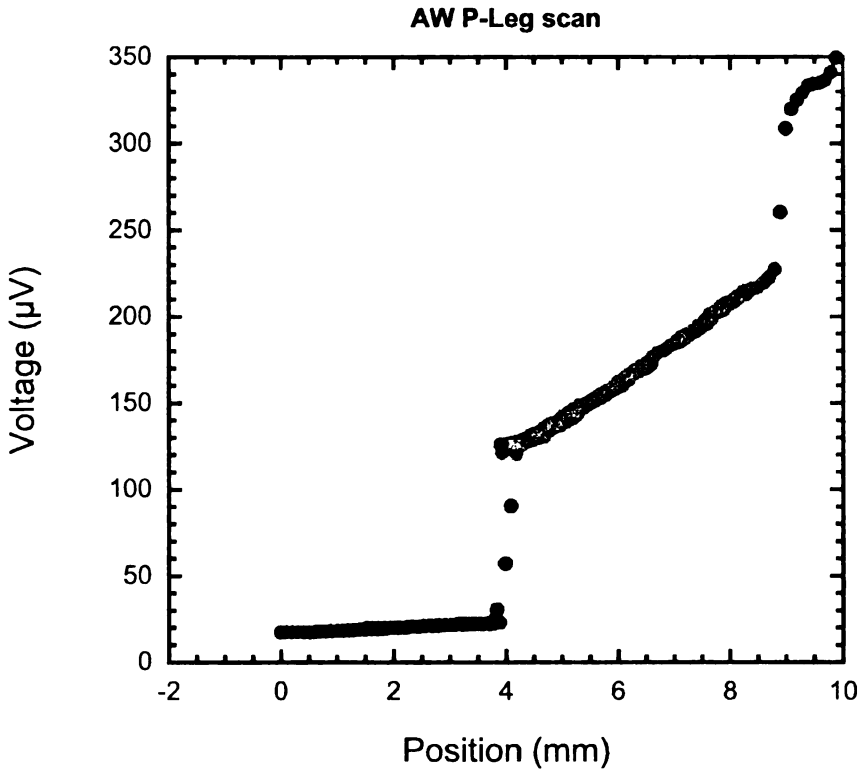

Figure 134: Scan of P leg from unicouple run AW.

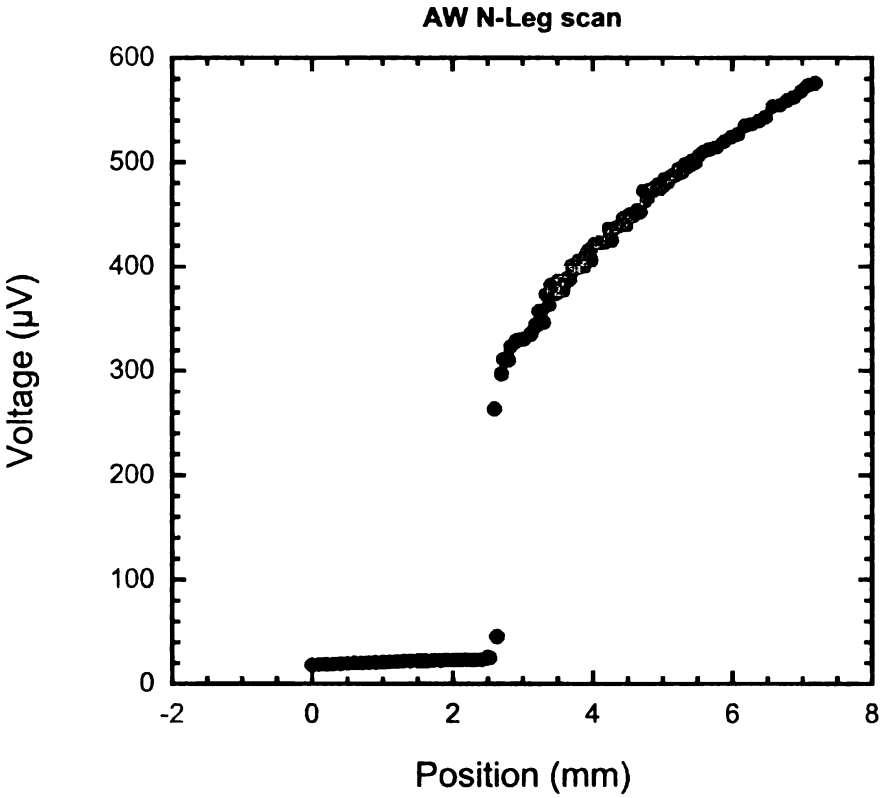

Figure 135: N leg scan of bonding run AW.

The conductivity of the n-type material after bonding at 800°C was 902.9 S/cm. This gives insight on how the material reacts at higher temperatures for long periods of time. Even though the properties did not change from bonding run AW, the yield was low suggesting longer bonding times and/or higher mechanical pressure on the interface may be needed.

A hot pressed experiment was done with powdered 316 stainless and powdered LAST. The hope was that the stainless steel and LAST would sinter during the hot pressing run. A voltage scan across the interface between the hot pressed stainless steel to LAST is shown in Figure 136.

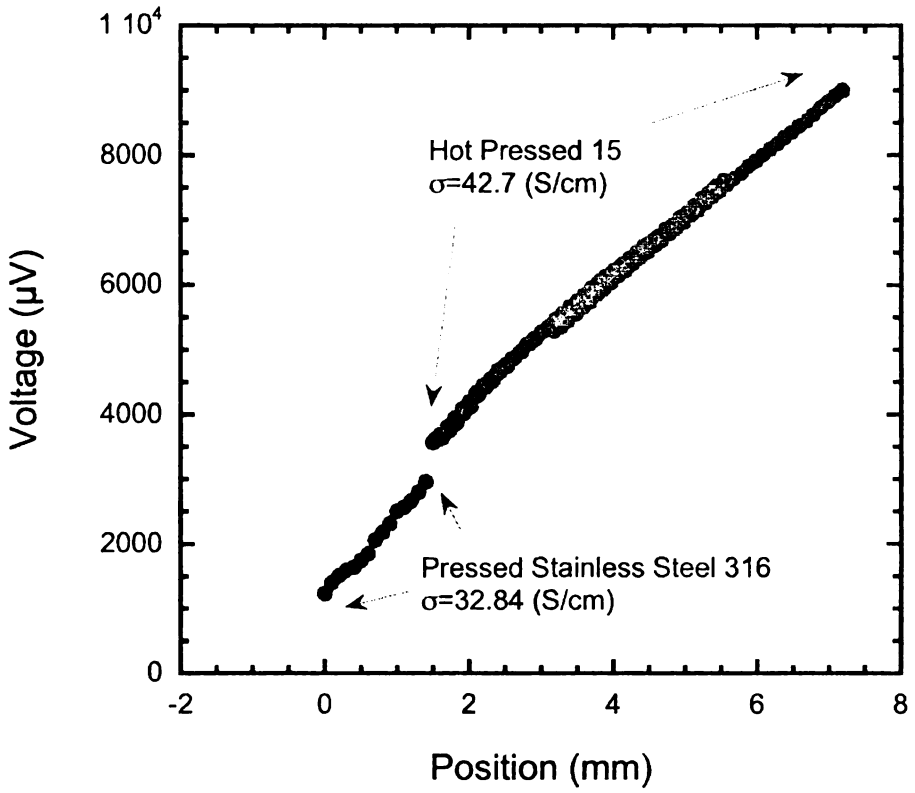

Figure 136: Scan of hot pressed 316 and LAST.

The conductivity of cast stainless steel 316 is nearly 13,000 S/cm, but the hot pressed powder done in this experiment was only 32.84 S/cm. The large differences in the optimal pressing and sintering conditions of stainless steel compared to those for LAST are believed to be the cause of the relatively low electrical conductivity for the stainless steel. Annealing of this sample at 700°C for 6.5 hours did not improve the stainless steel, but rather lowered its conductivity to 3 S/cm.

Unicouple run AX was a bond of ETN173 and ETN174 to 316 stainless steel. The soak temperature of the run was 720°C for 12 hours. The bonding time was

taken to an extreme to see how the bonding results. The pressure was maintained at 780 Torr with a flow of 1LPM of an Ar/H_2 forming gas.

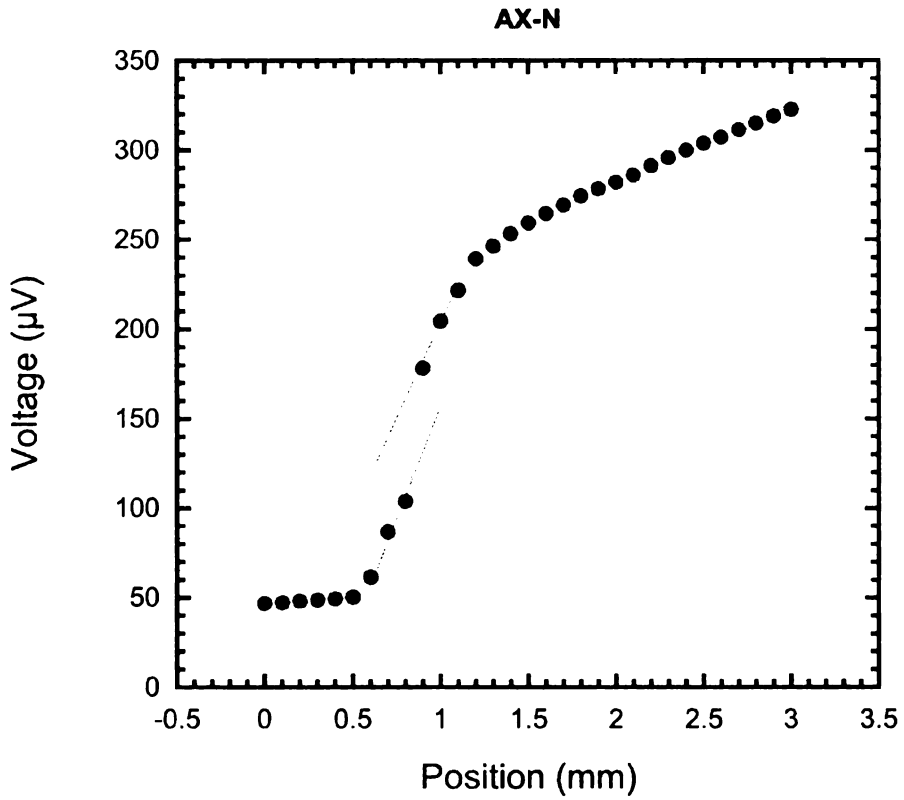

Figure 137 Scan of N leg contact scan from run AX

Figure 138: EDS maps of unicouple run AX bond.


Pb

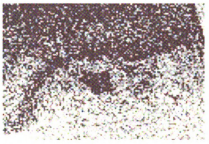
O


Cr


Mn


Fe


Ni


Cu


Ag


Sb


Te

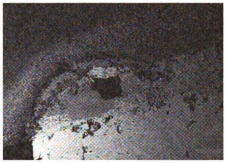

Figure 138 Contiued: EDS maps of unicouple run AX bond.

Error! Reference source not found. shows an EDS mapping of the contact between the stainless steel and LAST material after a 12 hour bonding at 720°C. The contact area appears to have plastically deformed.

Unicouple run BA was a bond of ETN176 and ETP42 to 316 stainless steel. A two stage bond was used. Both stage soak temperatures were 700°C for 4.5 hours. Unicouple run BB was similar to bonding run BA but used all hot pressed materials. It was a bond of HPMSU12-N and HPMSU18-P to 316 stainless steel. Stage 1 of bonding used a 30 minute ramp and 6.5 hour soak at 700°C. It had a flowing gas rate of 1LPM maintained at a pressure of 790 Torr. None of the bonds resulted from this stage of the bonding. Stage two also showed no bonds between the p-type

material and the 316. No conclusions were made as of yet on why the hot pressed material did not bond to the 316.

Unicouple run BG was a bond of ETN179 to 316 stainless steel. Stage one of the bond was done with a 30 minute ramp and 6.5 hour soak at 720°C. Stage 2 of the bond was done with a 4.5 hour ramp and 6.5 hour soak at 720°C. Unicouple run BG fabricated 8 out of 11 modules.

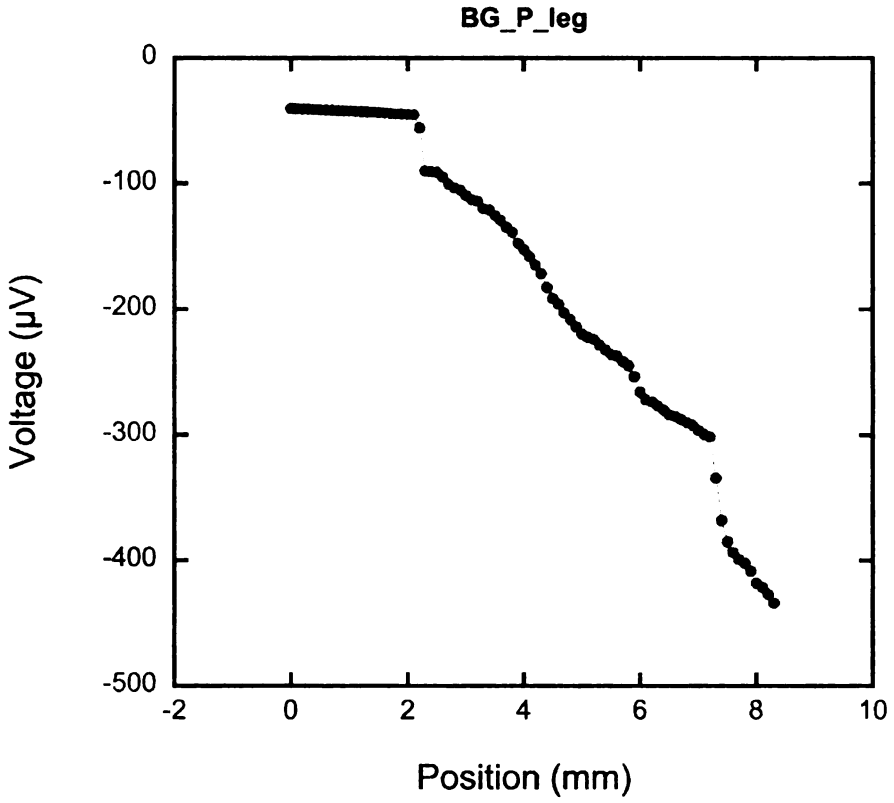

Figure 139: Unicouple run BG P leg scan.

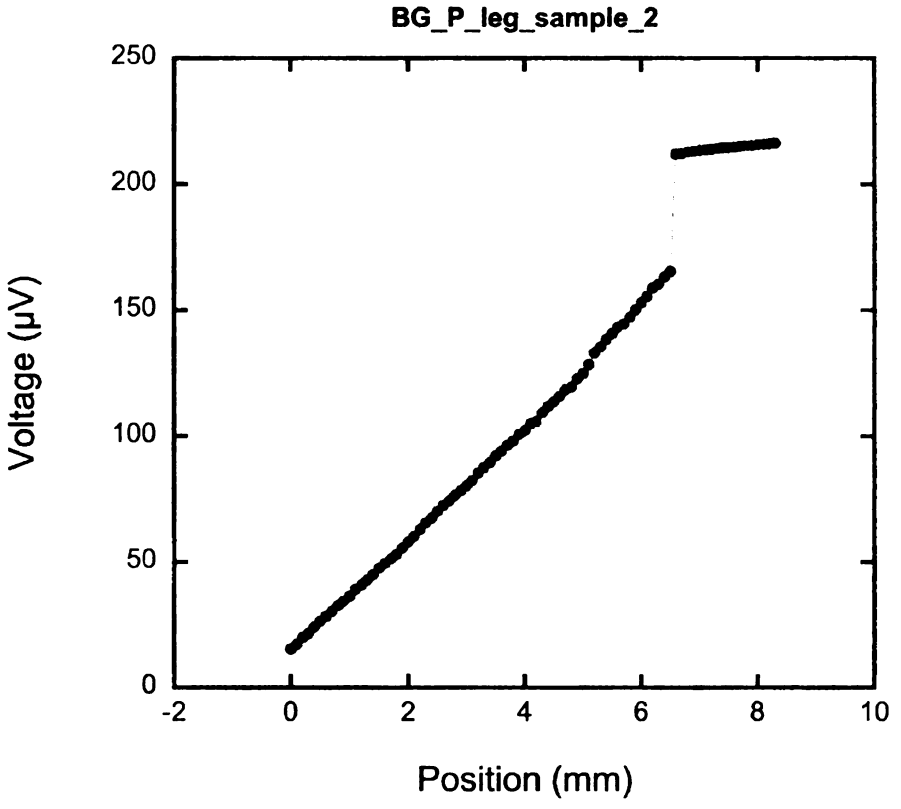

Figure 140 BG sample 2 P leg scan

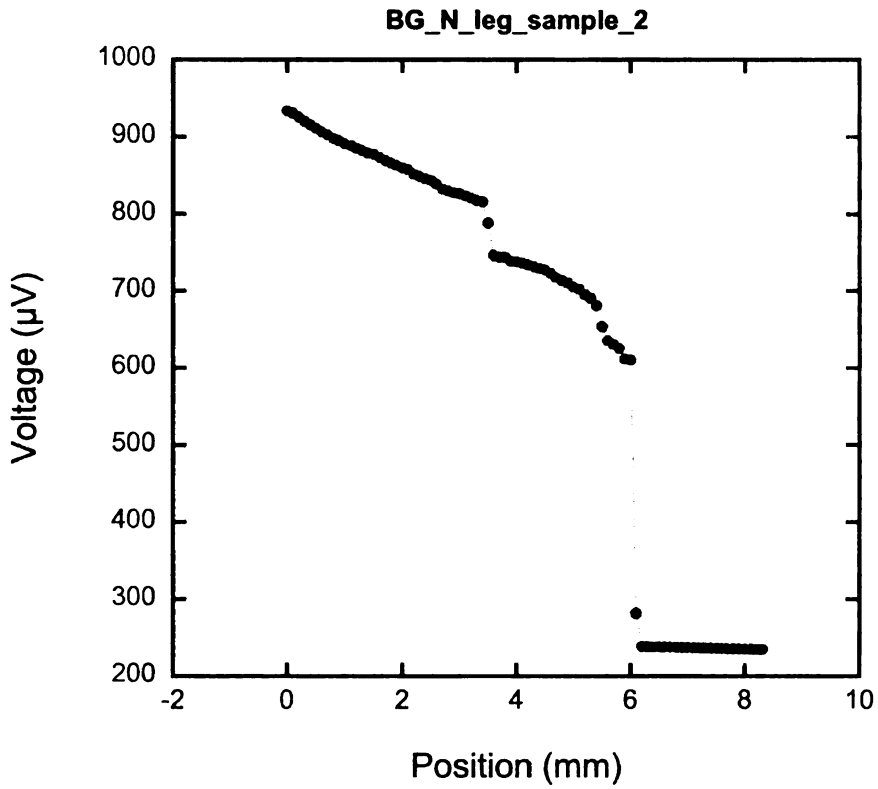

Figure 141 Unicouple run BG sample 2 N leg scan

Unicouple run BH was a bond of MSUHP20 and ETP44 to 316 stainless steel. The bond was done with a 4.5 hour ramp and 6.5 hour soak at 720°C. BH run completed with 5 unicouples bonded. One unicouple was scanned while the other were machined for segmentation with Bi_2Te_3.

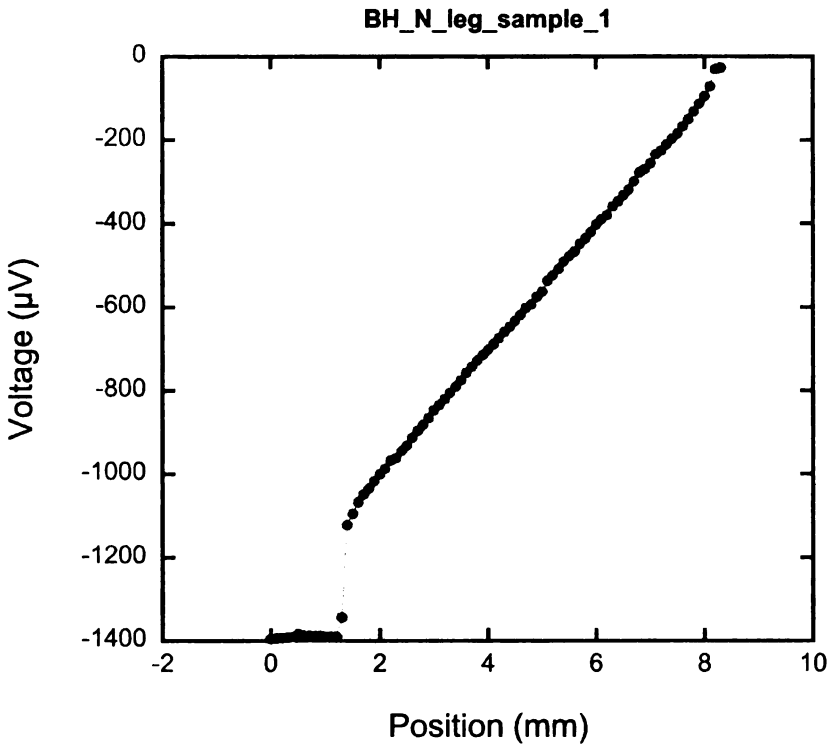

Figure 142: Unicouple run BH N leg scan.

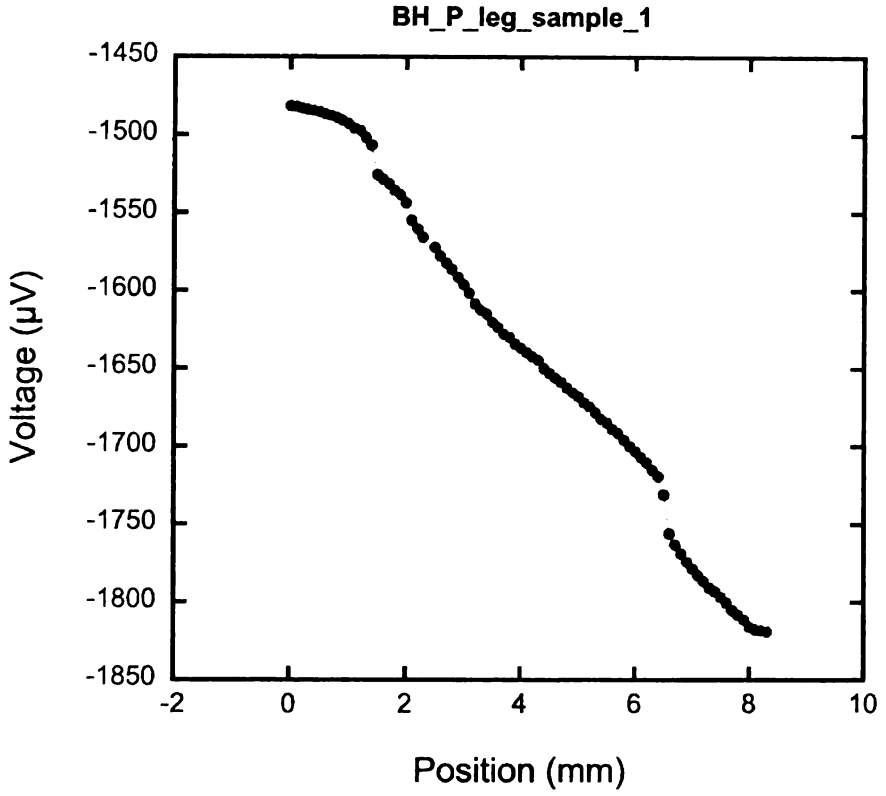

Figure 143: Unicouple run BH P leg scan.

Unicouple run BI was a bond of ETP44 with stainless steel bonded on both sides. The bond was done with a 4.5 hour ramp and 6.5 hour soak at 720°C. During the run there was a flow of argon-hydrogen at a pressure of 790 Torr.

Unicouple run BJ was a bond of HPMSU20-N and ETP44 to stainless steel 316. The bond was done with a 4.5 hour ramp and a 6.5 hour soak at 720ºC.

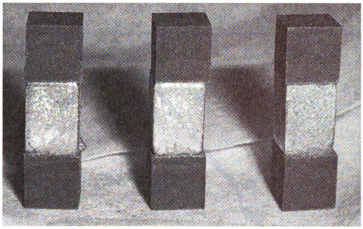

Figure 144: Three p-types with 316 stainless bonded to both ends.

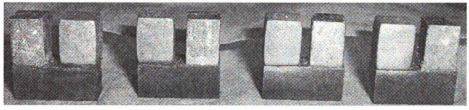

Figure 145 Unicouples fabricated from run BJ.

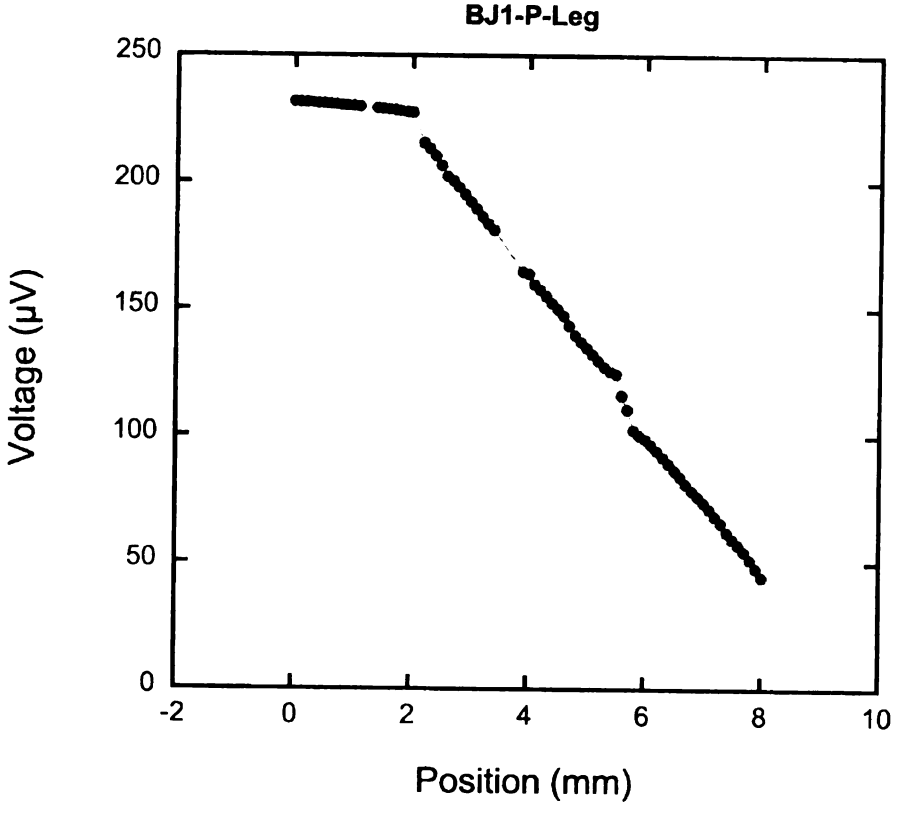

Figure 146: BJ1 P leg scan.

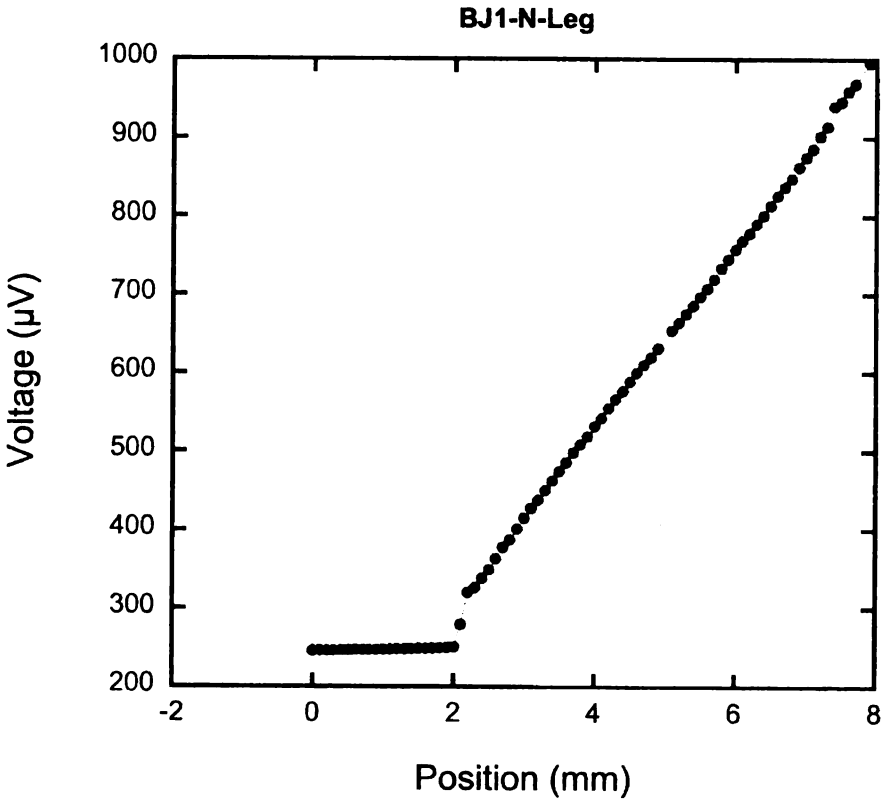

Figure 147: BJ1 N leg scan.

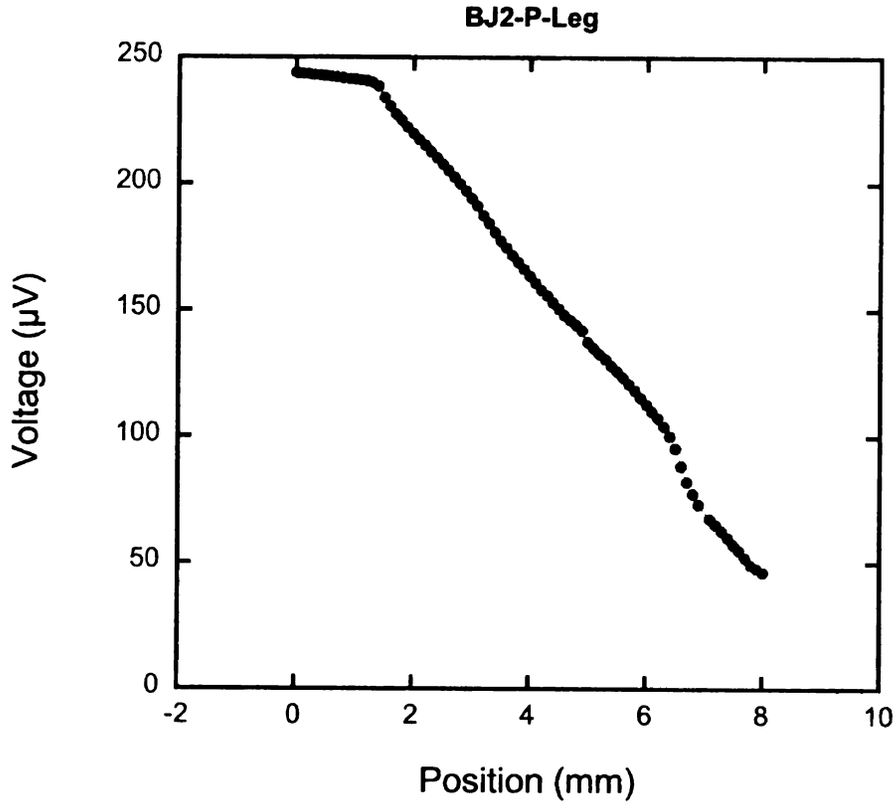

Figure 148: BJ2 P leg scan.

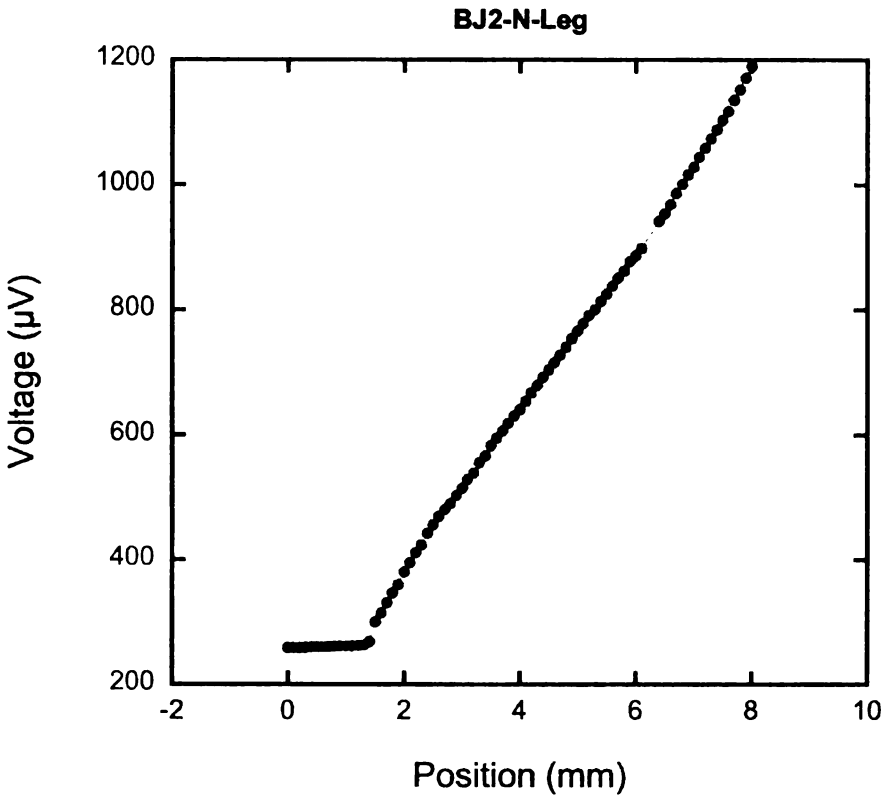

Figure 149: BJ2 N leg scan.

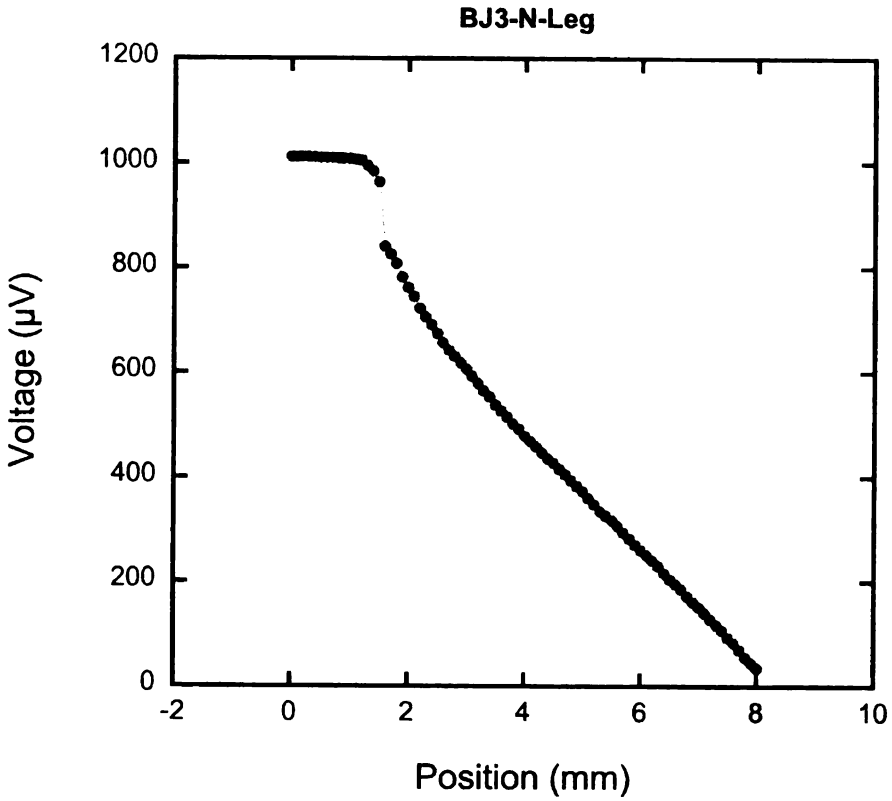

Figure 150: BJ3 N leg scan.

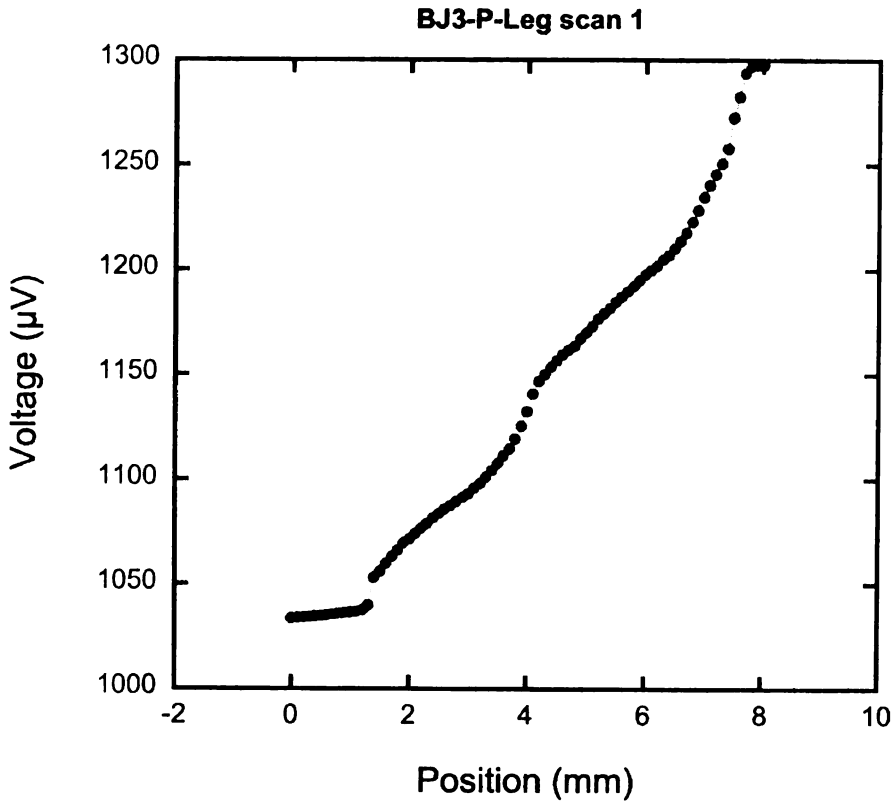

Figure 151: BJ3 P leg scan.

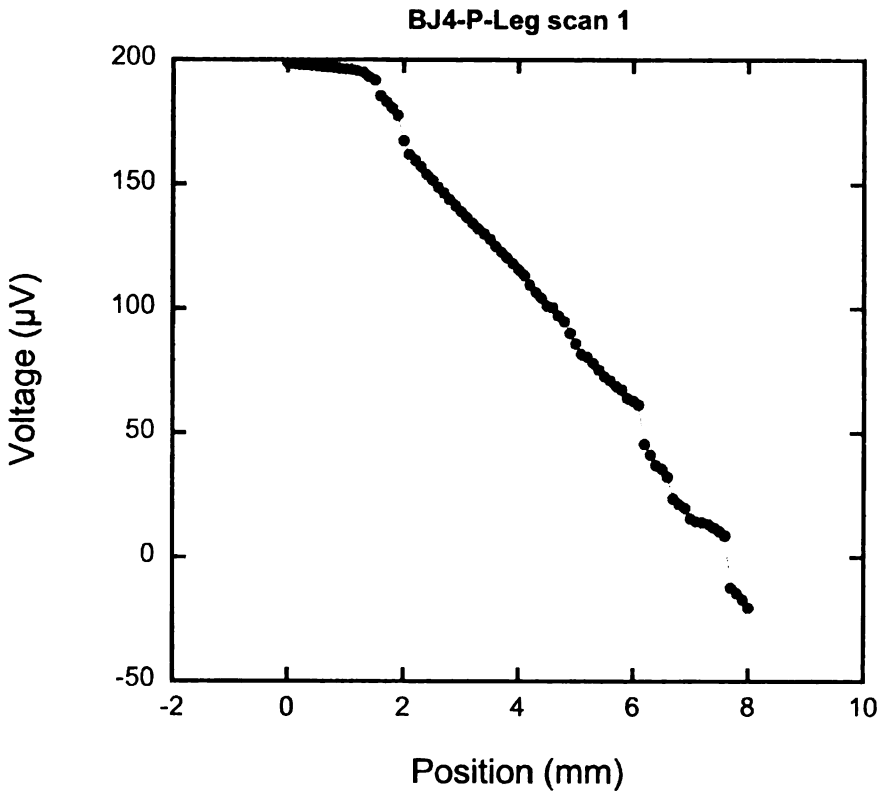

Figure 152: BJ4 P leg scan.

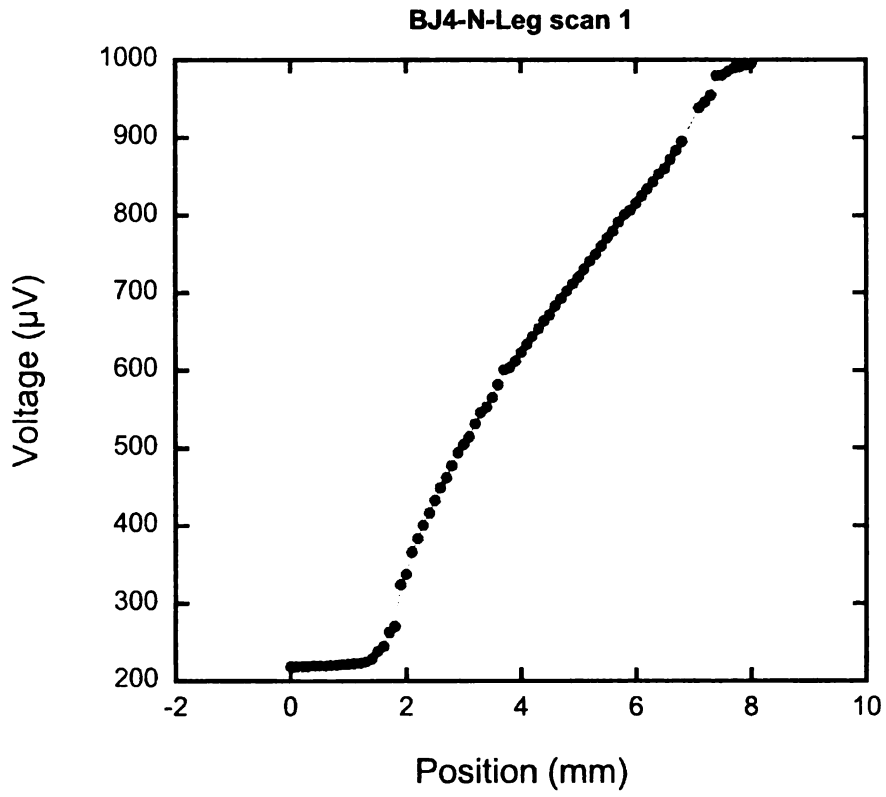

Figure 153: BJ4 P leg scan.

As shown in the figures above most of the scans show good contact resistance and the material does not have many cracks. The average resistance of the unicouples in run BJ was 10mΩ. The unicouples are nickel plated and then coated with QS/B4. The QS/B4 is used to inhibit outgassing of the unicouple legs during high temperature operations. The legs are nickel plated to protect the unicouples from the QS/B4, due to the fact that it is very basic and eats away at the legs during curing.

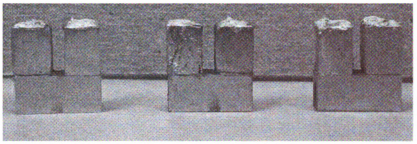

Figure 154: The unicouples were nickel plated for preparation to be coated with QS/B4.

Unicouple run BK was a bond of MSUHP24 and ETP44 to 316 stainless steel. The bond was done with a 4.5 hour ramp and 6.5 hour soak at 720°C. The gas flow was at 1 LPM at a pressure of 800 Torr. All 4 unicouples attempted successfully bonded.

A bonding run of seven HPMSU30-N to 316 stainless steel was done. The 316 stainless steel was polished with 800 grit sandpaper. The MSUHP30-N was then polished lightly with 1200 grit sandpaper. The torque on the bonding device was 6 inch-lbs. The first stage of bonding was done at 720°C for 6 hours with a 4 hour ramp. Unfortunately, none of the samples bonded after this first stage. Either it was the hot pressed material not being able to bond to the 316 or the polishing of the 316 and the LAST caused poor bonding conditions. Past results have also shown failed bonds when polishing of the legs was involved.

A new bonding device was developed to have a spring loaded mechanical pressure during bonding. Using this device (Figure 155), a sample of ETP44 was bond to 316 stainless steel at 720°C with a 4.5 hour ramp and 6.5 hour soak.

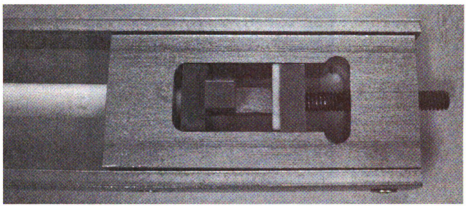

Figure 155: Head piece of spring loaded bonding device.

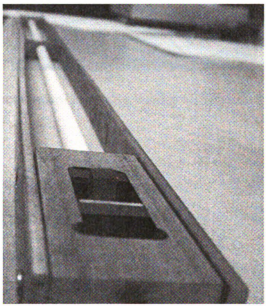

Figure 156: Long view of spring load device from main head down shaft.

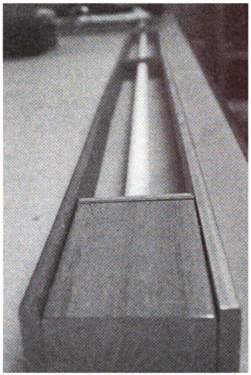

Figure 157: Base mechanism of spring loaded device which houses the spring.

The spring loaded bonding structure was fabricated to keep the spring in the cold section of the furnace. This would help assure a constant pressure on the leg and stainless during the bonding run.

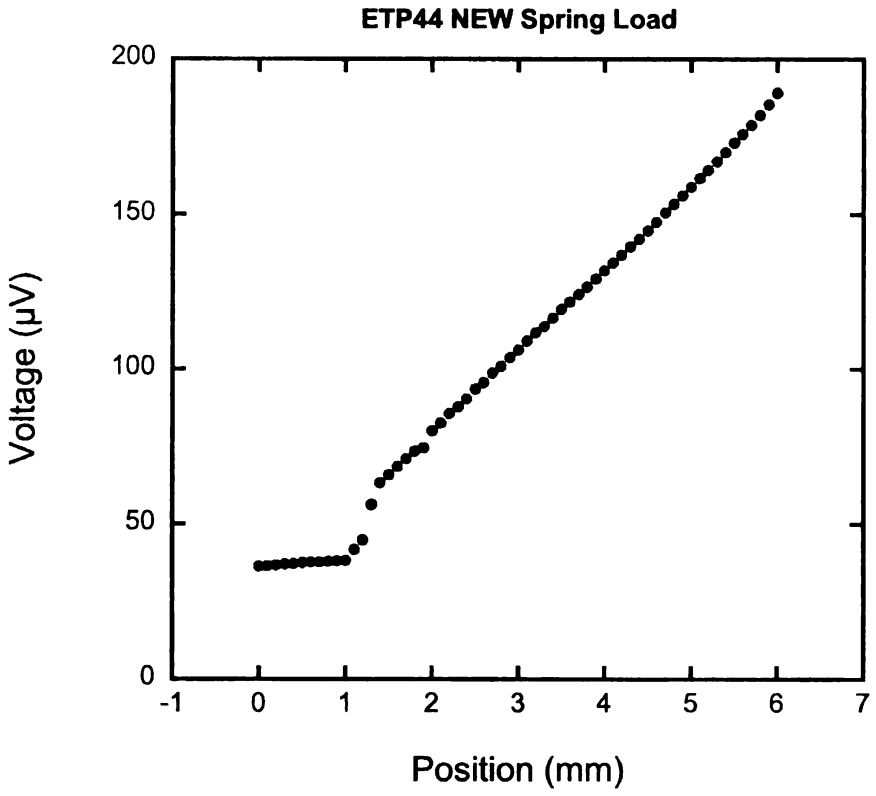

Figure 158: Scan of p-type contact to 316 stainless steel with spring loaded bonding device.

Figure 158 shows the scan of a resulting bond using the spring loaded device. The new bonding device is good for bonding, but because of its physical structure only 3 or 4 legs can be bonded at once.

A hot pressed leg, HP30, was placed into the spring loaded bonding device to be bonded to 316 stainless steel. The hot pressed material plastically deformed due to creep. The small grain size in the hot pressed material allows it to creep which can be advantageous in forming intimate contact at the junction.

An EDS study of p-type LASTT to 316 stainless steel was donebefore and after a post bonding annealing step. Figure 159 shows the EDS of the sample before annealing.

Figure 159: EDS of LASTT bonded to 316 stainless steel before annealing

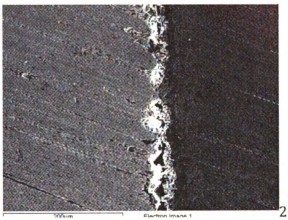

200μm Scale

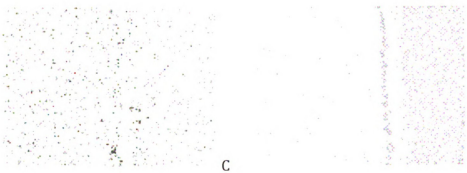

C Cr

O Fe

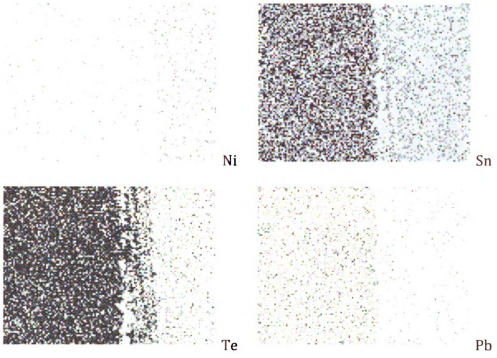

Figure 159 Continued: EDS of LASTT bonded to 316 stainless steel before annealing.

Figure 160: EDS of LASTT to 316 after an anneal at 620°C for 4 days.

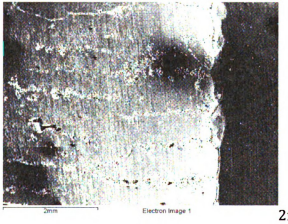

2mm Scale Bar

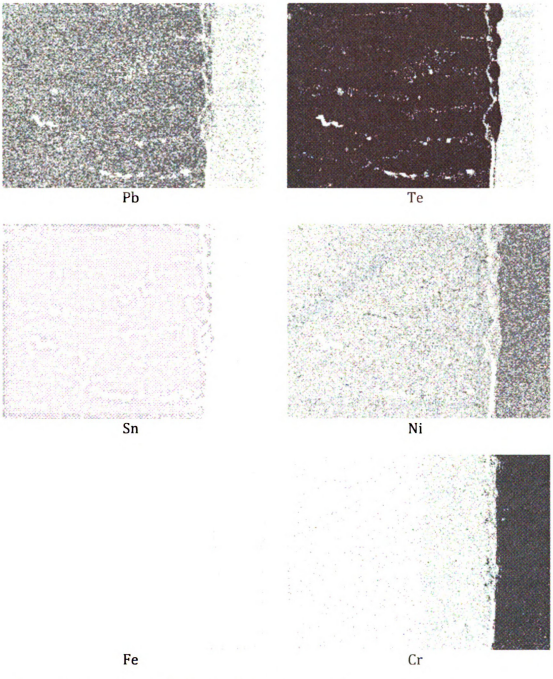

Figure 160 Continued: EDS of LASTT to 316 after an anneal at 620°C for 4 days.

The anneal was done at 620°C for 4 days in an argon-hydrogen atmosphere at 800 Torr. As seen from the EDS maps above, the nickel and chromium may have

diffused into the LASTT material. Lead looks to have diffused into the 316 stainless steel.

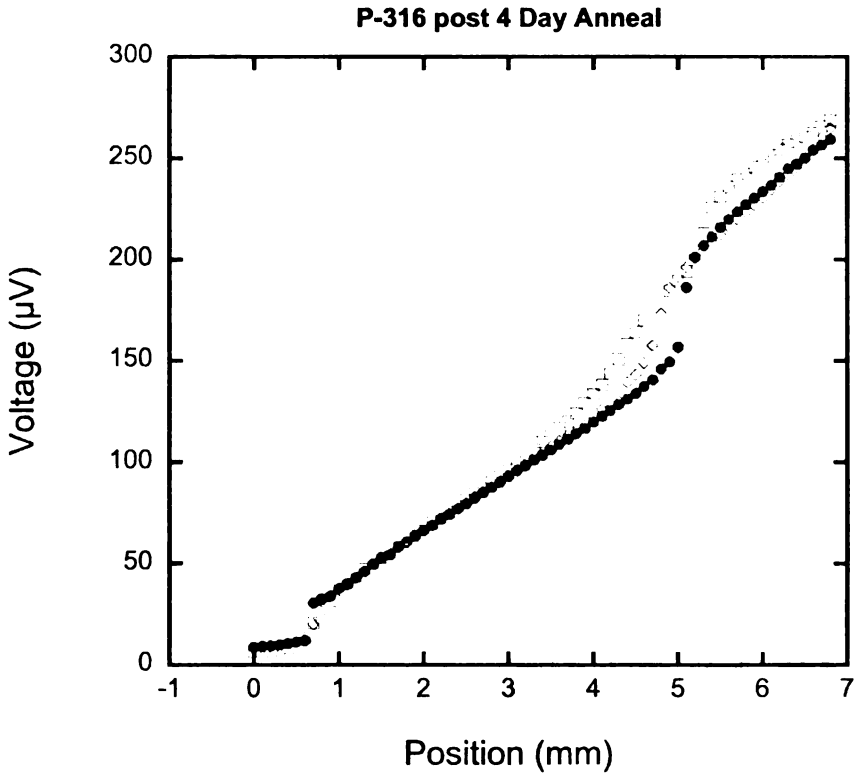

Figure 161: Post anneal scans of LASTT to 316 contact.

The SALT, $Na_{0.8}Pb_{20}Sb_{0.4}Te_{22}$, material has exhibited a high ZT [72], and an attempt was done to bond the SALT material to 316 stainless steel using 720°C for 6 hours with a 4 hour ramp. The torque on the set screw on the bonding ram rod was set to 6 lbs-inches. The gas was set to a pressure of 800 Torr and a flow of 1 LPM of Ar/H_2 gas was used. The $Na_{0.8}Pb_{20}Sb_{0.4}Te_{22}$ material did not bond to the stainless steel and a longer bonding time may be necessary.

A quenching experiment was done of a diffusion bond of 316 to LAST. An N leg was sealed in a quartz tube and placed into a furnace for eight hours at 600°C. After the soak it was quenched in a water bath. Contact scans were done before and after the quench to see the effects of the rapid temperature change.

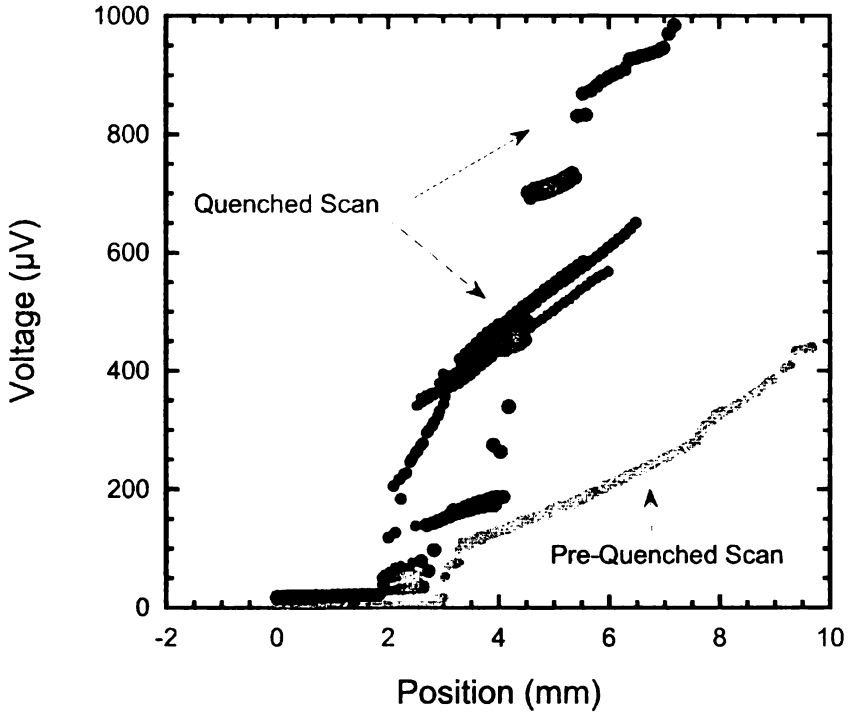

Figure 162: Before and after scans of quenching experiment.

The quenched sample exhibited many cracks in the sample showed by the voltage scan in Figure 162. The different colors in the scans are the measurements that wre taken across the entire sample. This proves if the module were to undergo rapid changes in temperature, it would destroy the module.

4.10 Diffusion Bonds of Molybdenum to LAST and LASTT Materials

Six n-type LAST legs were coated with a 20nm molybdenum film as a diffusion barrier. These samples were then attempted to be bonded to 316 stainless steel. The bond was done with a 30 minute ramp and 6.5 hour soak at 700°C. No bonds resulted from the experiment.

4.11 Diffusion Bonds of 347 Stainless Steel to LAST and LASTT Materials

Unicouple run AR was a bond of ETN137 to stainless steel 347. The 347 was used because it has a lower resistance than stainless steel 316 along with having a CTE of 18 ppm/K. The bond was done with a 30 minute ramp and 6.5 hour soak at 700°C. The cast n-type material did not bond to the 347 stainless steel.

Unicouple run AS was a bond of HP n-type to 347 stainless steel. The run conditions were the same as run AR. The hot pressed LAST did not bond to the 347 stainless steel.

4.12 Diffusion Bonds of 'Maganin' to LAST and LASTT Materials

An alloy of copper, manganese, and nickel was attempted to be bonded to LAST and LASTT. The alloys name is Manganin and has a coefficient of thermal expansion (CTE) of 13-19 ppm/K. ETN154 was bonded to the Manganin with a 4.5 hour ramp and 6.5 hour soak at 720°C. The end result was a melt of both the Manganin and LAST.

5.0 Module Fabrication and Measurements

5.1 Long Term Module Testing System (LTMTS)

5.1.1 System Fabrication

The system's main chamber is a stainless steel cylinder 5 inches in diameter. The structure of the main chamber is designed to pump down to pressures below a milli-Torr, and to be pressurize slightly above atmosphere. The flanges on either end of the main chamber have ISO flange connections. With the quick connect flange, it is easy to add or remove gas, electrical, or any other connection needed for the system. The stage of the system, which is also the cold plate, is welded directly to the main chamber flange. The cold plate is a liquid cooled plate that is controlled by a chiller. The chiller has a maximum cooling capacity of 215 Watts.

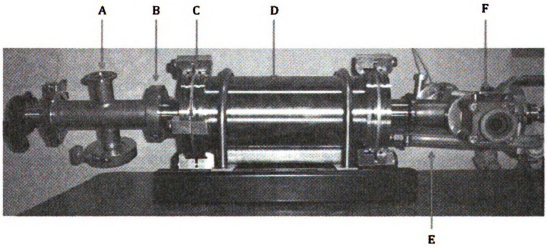

Figure 163: Long Term Module Testing System. A) Gas port; B) KF-40 quick connect; C) ISO Flange; D) Main Chamber; E) Chiller feed throughs for cold plate; F) Vacuum Port.

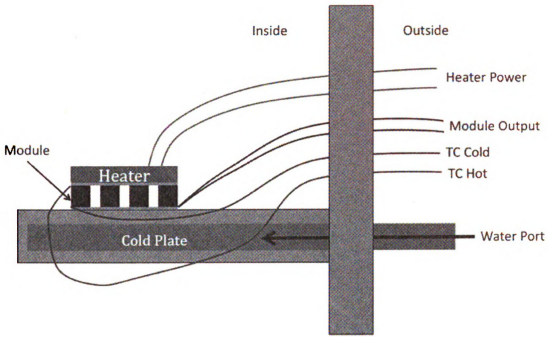

Figure 164: Schematic drawing of long-term module testing system.

The heater for the hot side of the thermoelectric is fabricated out of a 140μm thick nickel-chromium foil. During operation of the heater from room temperature to 150°C, the heater resistance varies from 2Ω to 1.8Ω. As shown in Figure 165 below the nickel-chromium heater has a temperature dependent coefficient of resistance of 0.001755 Ω/K. The nickel chromium heater has a very small dependence on temperature.

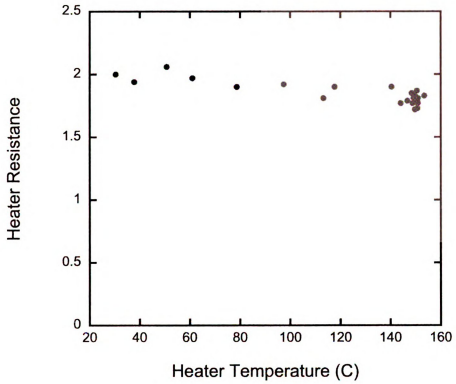

Figure 165: Heater Resistance as a function of temperature.

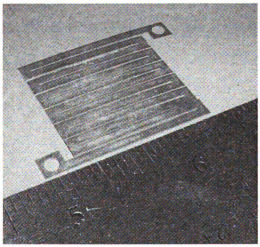

Figure 166: Nickel-chromium meandering line heater.

Figure 166 shows the nickel-chromium heater. The electrodes are connected to the heater with a nut and bolt assembly. The leads to the heater are attached to the cold

plate to keep the wire insulation from melting during operation. The heater is powered by a 1200W power supply. Thermocouples are attached to the heater to measure the temperature for feedback to the power supply. The placement of the hot side thermal couple is at the base of the heater next to the module's hot side. The cold side thermocouple is placed next to the module on the cold plate (shown in Figure 164). Computer control and data acquisition is maintained using software developed in the LabView™ programming environment. The software is used to monitor the temperatures of the hot side and cold side of the module and to set the current that is being supplied to the hot side heater.

A Keithley 2182 Nanovolt Meter is used to measure the output voltage to the load. A True RMS AC/DC Mini Clamp Meter measures the current to the load by magnetic pickup from the load wires. Combinations of resistors are used for loads.

The system uses a tri-scroll dry pump with a base pressure of 1mTorr. High vacuum is not needed for this system. A tank of argon is used to pressurize the main chamber with an inert gas.

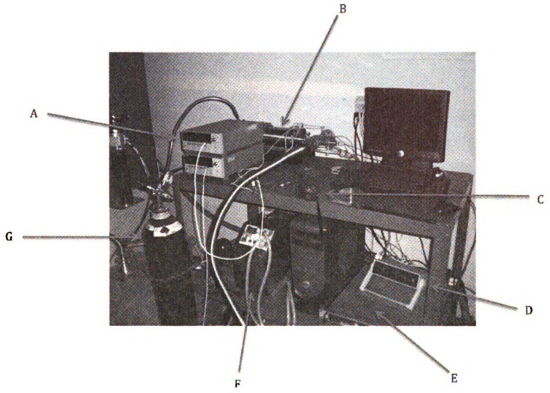

Figure 167: Complete system. A) Nano Voltmeter; B) Main Chamber; C) Current Meter; D) Temperature Monitor; E) Power Supply; F) Chiller; G) Argon Gas Cylinder.

5.1.2 Experimental Procedure

The module is placed on the cold plate using a thermal grease. For this study a Tellurex power generation module was used as a reference sample[73]. Thermocouples were placed on the hot side and cold side to monitor their temperatures. The module leads were soldered to 14 gauge copper wire feed-throughs. The nickel-chromium heater is bolted to a separate pair of 14 gauge copper wire feed-throughs.

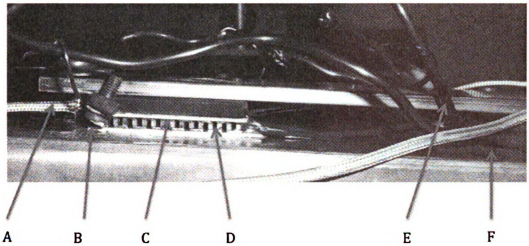

Figure 168: Test Setup. A)Thermocouple; B)Bolt heater connection; C)Nickel-chromium heater; D)Thermoelectric module E)Module leads to feed-through solder connection; F)Thermally grounded leads.

The standard procedure is that the cold plate is placed into the main chamber, and the chamber is initially pumped down with the roughing pump. The chamber is then backfilled with argon gas followed by pumping down to 1mTorr and this backfill/pump down procedure is repeated at least three times to ensure a better oxygen free vacuum. After sufficient pumping, the system is filled with argon to approximately 780 Torr. The chiller is initially set to 30°C. Since the heater is custom made, an initial slow heating is done to monitor the power input vs. temperature of the nickel-chromium heater as shown in Figure 169.

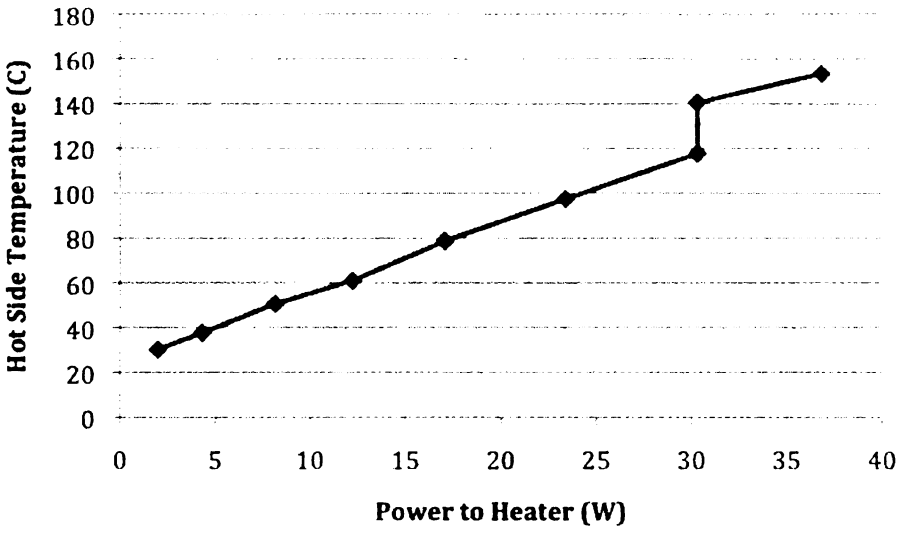

Figure 169: Power to hot side heater and corresponding temperature. Note: At heater power 30Watts the chiller temperature was increased from 30°C to 35°C. All temperatures are measured under an open circuit condition.

The effect of heat flow through the module is clearly seen in Figure 169 by a change in the cold side temperature (chiller) by 5°C. Under an open circuit condition, the input power to the heater of 37 watts gives the maximum operating temperature of the Tellurex module, 150°C. Once a load is applied to the module the Peltier Effect will begin to decrease the hot side temperature, and heater power must be increased to maintain the hot side temperature of 150°C. Under short circuit condition, the hot side temperature drops to 113°C with a heater power of 40 watts. For testing under a matched load condition, 5(Ω), the heater power must be increased to 70 watts to obtain a hot side temperature of 150°C.

5.1.3 Results

For characterizing the system's measurement accuracy a commercial power generation module was used [73]. Over a period of one month different loads were attached and the corresponding voltages, currents, and powers were measured.

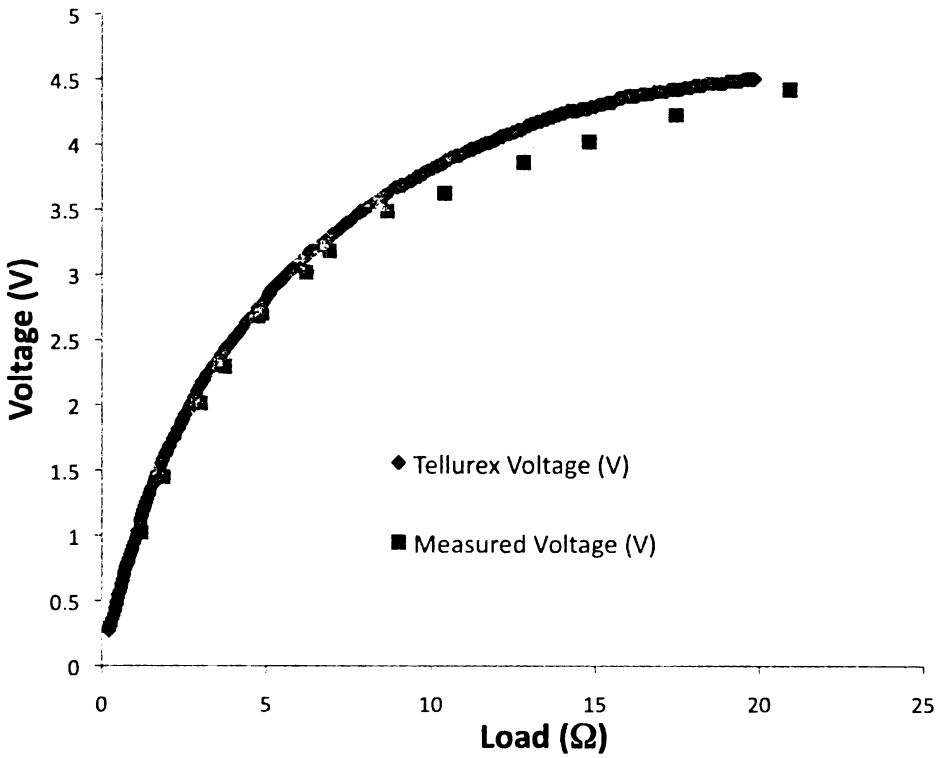

Figure 170: Comparison of voltage measured by the LTMTS and published Tellurex results.

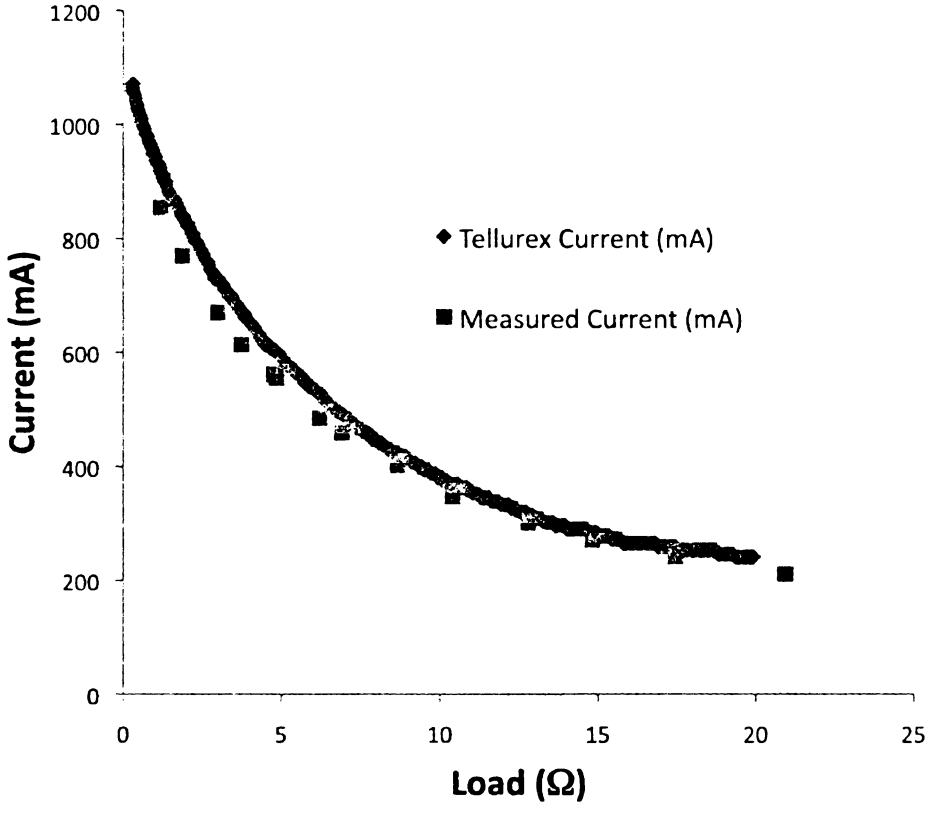

Figure 171: Comparison of the current measured by the LTMTS and Tellurex.

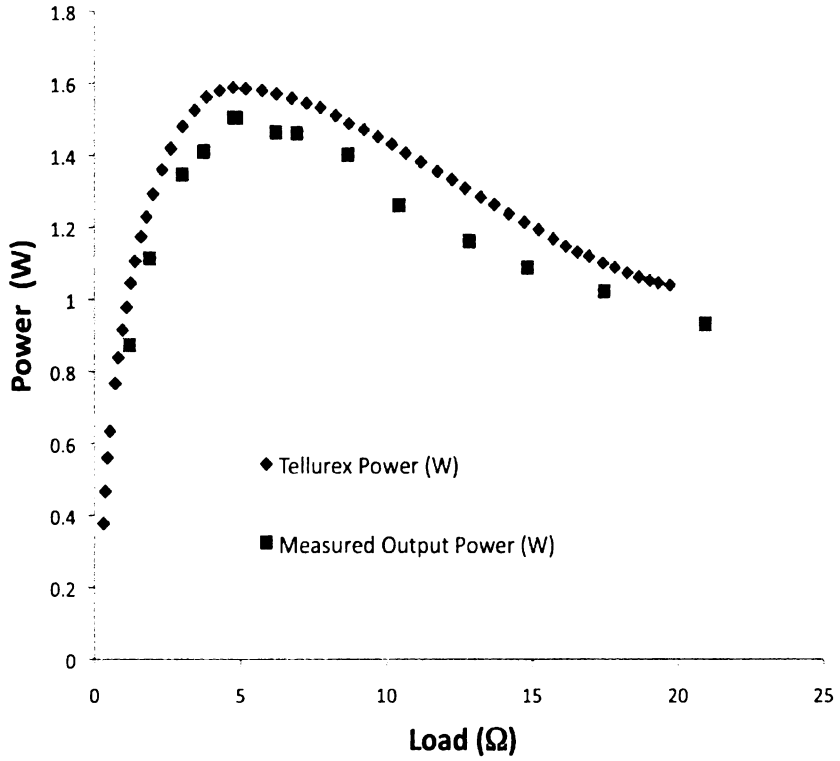

Figure 172: Comparison of the power measured by the LTMTS and Tellurex.

As shown in the above figures, the LTMTS is capable of accurate measurements of thermoelectric power generation devices. After the characterization of the LTMTS, a long-term test was done on the same module with the results shown in Figure 173.

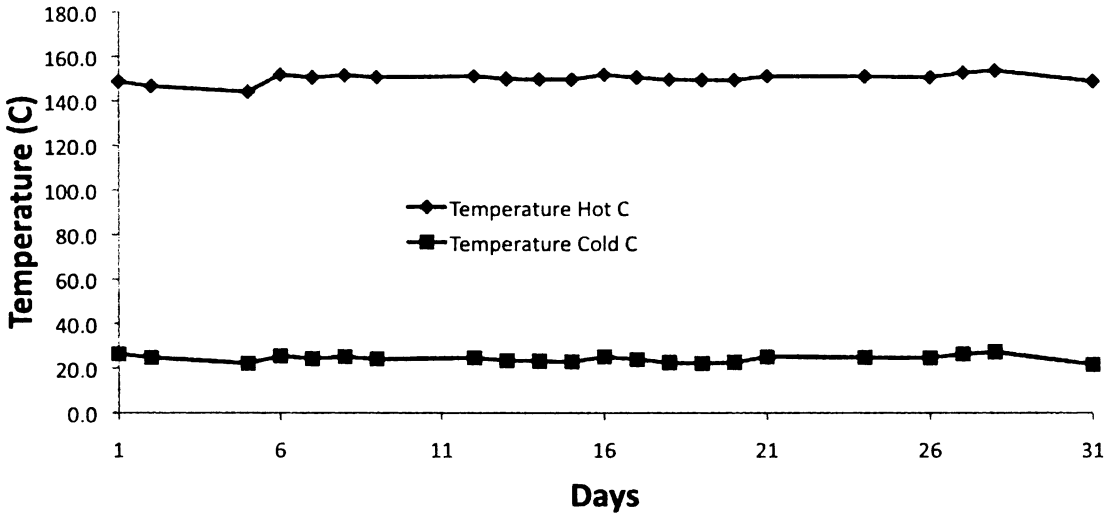

Figure 173: Hot side and cold side temperatures of module during month long test. After one week of operation the heater power was increased to raise the hot side temperature, and then it was maintained for the duration of the experiment.

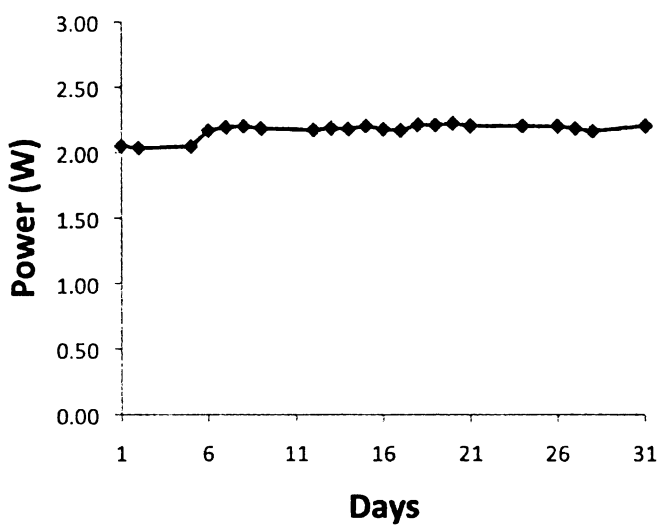

Figure 174: Power output of the Tellurex module over one month of operation.

Figure 174 shows the measured power output of the purchased Tellurex module over a month long period of time. These results give confidence in an accurate long term measurement can be done with the LTMTS.

A small heater for individual unicouples was built using a nickel-chromium wire wrapped around an alumina substrate and then cast in an alumina adhesive.

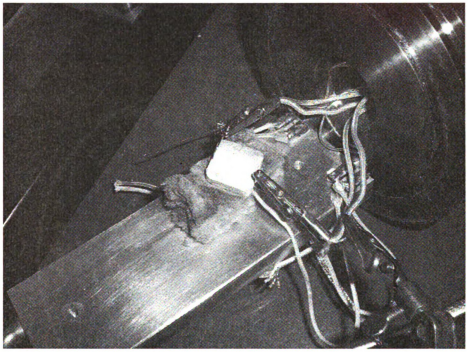

Figure 175: Hand made heater being tested in the LTMTS.

The heater shown in Figure 175 was tested at 600°C for 48 hours. This showed that the heater could be used for testing unicouples for long periods of time. Another heater was tested for 120 hours at 600°C and also worked without degrading. A photo of the heater is shown below after being strapped down to an insulation encapsulated module.

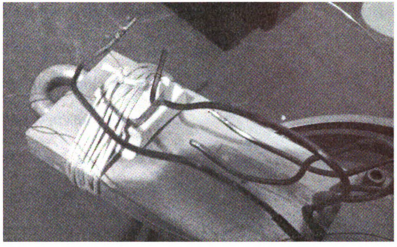

Figure 176: Top view of heater in LTMTS.

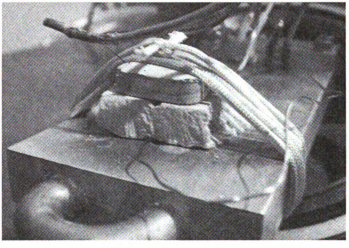

Figure 177: Front view of experimental setup of heater in the LTMTS.

5.2: LAST and LASTT Modules

Metalizing the cold side alumina plates has been a concern. A thermally conductive and electrically insulating material is needed as a substrate which can be metalized to define the electrodes. A patent was found that is used to metalize aluminum nitride [74]. The patent explains how to deposit chromium to the

aluminum nitride followed by anneals in air and then argon. This method was used to fabricate the cold side contacts of the modules built here. The chromium was sputtered to the aluminum nitride with a shadow mask. The first sputtering stage was done at 300 Watts for 1 hour. It was then annealed at 450°C for 2.5 hours in air. The second sputtering stage was also done at 300 Watts for one hour. Without breaking vacuum tungsten was e-beamed to the chromium for 1/2 hour at 450mA. The contacts were then electroplated with nickel and then annealed at 250°C for 4 hours with an argon-hydrogen atmosphere.

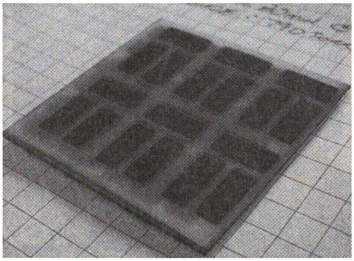

Figure 178: Completed cold side contacts of chromium to aluminum nitride.

Later it was discovered that initial depositions of the chromium at 350 Watts for 30 minutes anneals better to the aluminum nitride. After the initial anneal in air for 2 hours at 450°C the chromium contacts turn a brown color, which is known to be the color of chromium oxide. The plating step of nickel showed best results when plated for 15 minutes at 1.3 volts for each individual contact. After nickel plating

one more anneal was done at 250°C for 4 hours under vacuum. These contacts worked best for modules built.

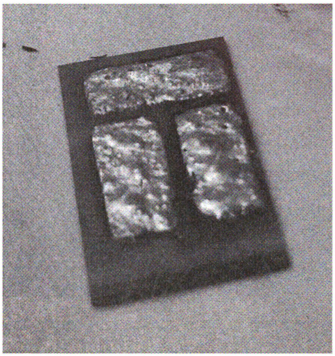

Figure 179: Contact with PbSn solder.

Unicouples from runs AW and AX were nickel plated, soldered into four leg modules and then coated with QS/B4. Then the modules were tested in air for power output.

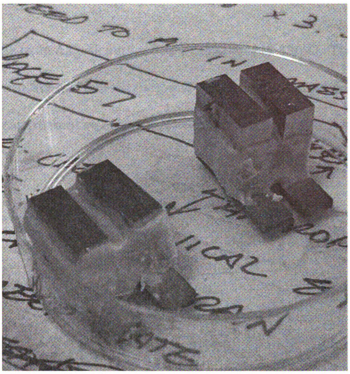

Figure 180: Modules fabricated from unicouples AX and AW.

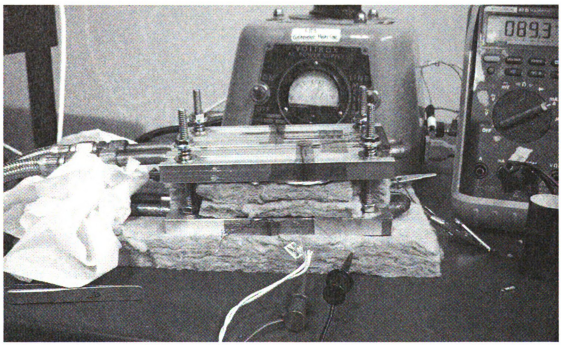

Figure 181: Test set-up for module power output test.

The module made from AX unicouples had a resistance of 33mΩ. The module made from unicouple run AW had a resistance of 276mΩ. The AW module resistance is too high for a measurement so only the AX module was used in this setup.

Table 6: Module AX output results.

Day	Time	Th (°C)	Tc (°C)	ΔT	Voc (mV)	Isc (mA)
1	16:15	481.11	70.02	411.09	179	84.8
1	18:40	485.84	72.69	413.15	188	89.1
2	9:25	484.6	71.67	412.93	193.3	90
2	13:15	484.4	71.29	413.11	194.2	90.3
5	10:00	491.3	65.01	426.29	196.2	86.6
5	12:04	599.01	85.55	513.46	235.9	99
5	18:58	603.83	88.42	515.41	228.5	87.1
6	5:25	603.31	88.33	514.98	228.1	79.5
7	10:20	600.46	88.33	512.13	228.1	79.5

The test setup had a lot of parasitic resistances so actual short circuit current was higher than the values shown in Table 6. The output voltage under open circuit conditions is in good agreement with thermopower measurements of these materials, which is approximately 200mV.

Unicouple run AY and AZ was a bond of MSUHP12 and ETP40 to 316 stainless steel. This was a two stage run. All of the legs to be bonded were cut to lengths of 5mm because samples will be soldered to Bi_2Te_3 after bonding in order to form segmented legs. Stage 1 had a 30 minute ramp and stage two had a 4.5 hour ramp and both stages had a 6.5 hour soak at 700°C. The gas flow rates for both stages were 1LPM with a pressure of 790 Torr. A module made from these runs had an open circuit voltage of 192mV with a 206.2°C temperature gradient across the four leg modules.

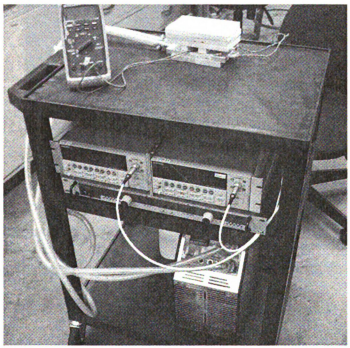

Figure 182: Mobile module testing setup. This set up can be used in the lab and also for public demonstrations.

Unicouple run BF was a bond of four ETN179 to 316 stainless steel samples. Stage one of the bond had a 30 minute ramp and 6.5 hour soak at 700°C. The gas was flowing at 1LPM with a pressure of 790 Torr. All 4 ETN179 bonded to the 316.

Stage 2 of bonding run BF was a bond of p-type material (ETP ??) to the 316 to complete the unicouple. The bond was done with a 4.5 hour ramp and 6.5 hour soak at 700°C. The pressure was 790 Torr and the gas flowed at 1LPM. One unicouple was fabricated from run BF and was built into a module.

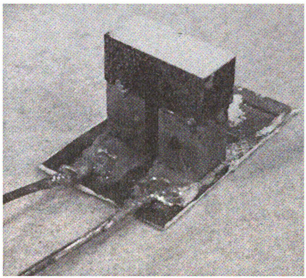

Figure 183: Unicouple BF built into module.

The module was tested in the mobile testing device shown in Figure 182. The short circuit current out of the module was up to 3.3 Amperes which was the highest current reported out of a module in the labs to that day.

One module was fabricated, BG2, and had a room temperature resistance of 9.08mΩ. This room temperature resistance was comfirmed with the room temperature scans shown in Figure 140 and Figure 141. The module was put into the mobile testing system.

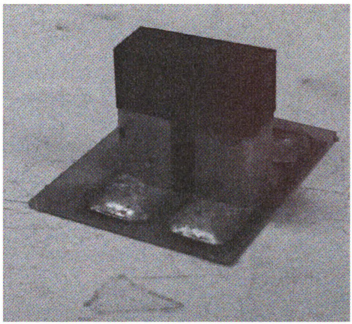

Figure 184: Unicouple module BG2.

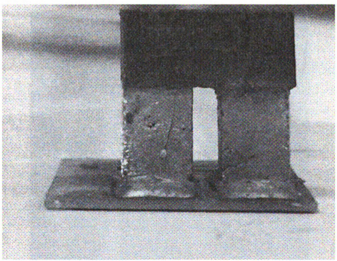

Figure 185: Unicouple module BG2 front view.

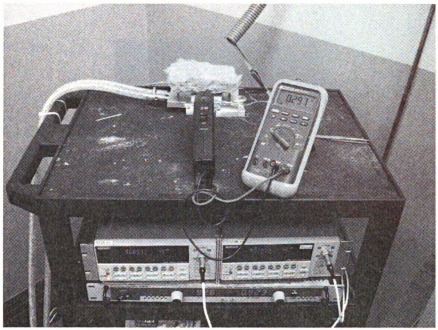

Figure 186: Picture of experimental setup.

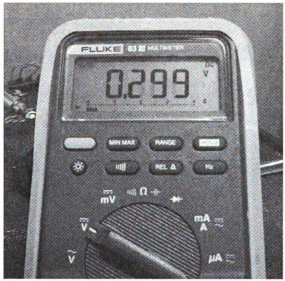

Figure 187: Reading from current sensor (1 volt is a reading of 10 amps).

Figure 188: Hot side temperature reading.

Figure 189: Cold side temperature reading.

Module BG2 produced 3 amps with a ΔT of 570.48°C. This experiment showed good repeatability with the results from module BF. Modules can be built from different bonding runs and show similar results.

A cold plate with contacts for 18 unicouples was fabricated using the chromium deposition technique onto aluminum nitride.

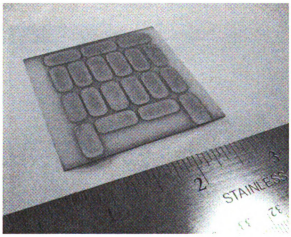

Figure 190: Cold side contact for a 36 leg module.

The unicouples were soldered to the cold side contact, but during this fabrication step 2 of the unicouple were destroyed so only 16 unicouples were used in the device.

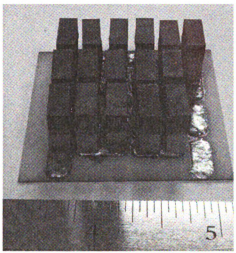

Figure 191: 32 leg module.

The module was the filled with QS/B4 and then had its resistance tested. No current could flow through the device indicating an open circuit condition at one or more of the junctions.

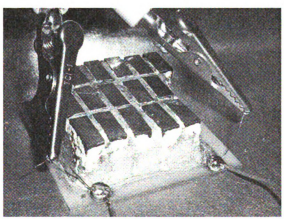

Figure 192: The electrical resistance was tested and it was an open circuit.

The conductance between adjacent unicouples was tested and the figure below shows the only places were the module was connected.

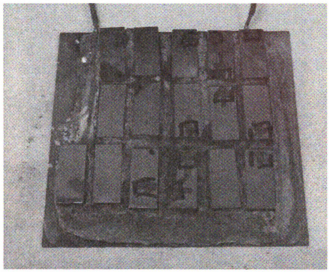

Figure 193: The red marks show were there is an electrical connection between unicouples.

Only five connections were sustained through a few hours of operation. The module was broken apart and studied. One of the largest construction failures was that the individual unicouples were not nickel plated before being coated with the QS/B4. This may be one of many other reasons for the breakdown of the device.

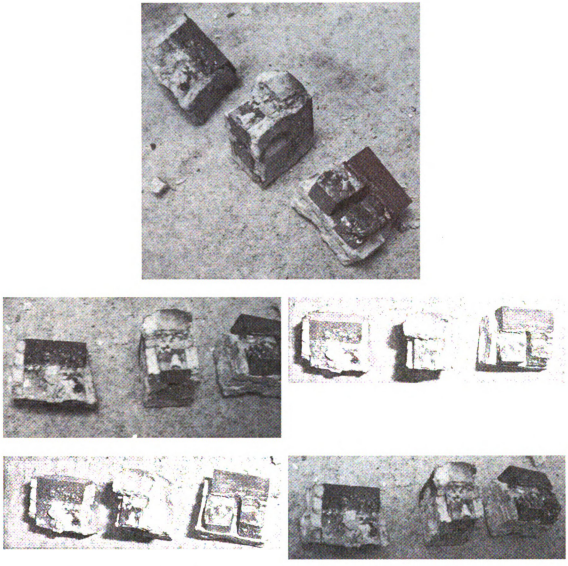

Figure 194: Photographs of unicouples taken out of the 32 leg module.

The photos above show oxidization developing between the stainless steel and the hot pressed LAST material. This is due to an oxidization of the iron in the stainless steel.

Using unicouples fabricated in runs BJ and BK, 4 modules were built.

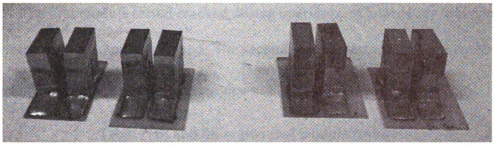

Figure 195: Unicouples built from runs BJ and BK.

Each module was nickel plated and then coated in QS/B4. Boron nitride was sprayed on top of each module to keep the electrodes from shorting to the heater.

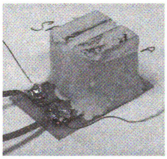

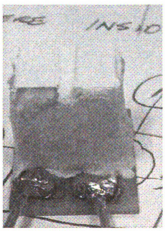

Figure 196: Completed module.

The first module tested cracked during operation. A later study was done to determine why the module cracked. The second module tested was segmented with Bi_2Te_3. The table below shows its results.

Table 7: BJ and BK segmented module results

T Hot	T Cold	Voltage	Current
613°C	30.92°C	408.7mV	0A
632°C	27°C	1.7mV	1.12A

The max power calculated for this module was 114mW. For a 4 leg device the expected power is around 500mW. The module ran under this gradient for one week.

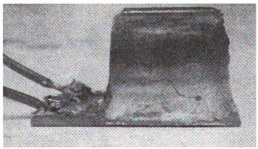

Figure 197: Module after one week of operation.

The module was dismantled and a scan was done on the legs.

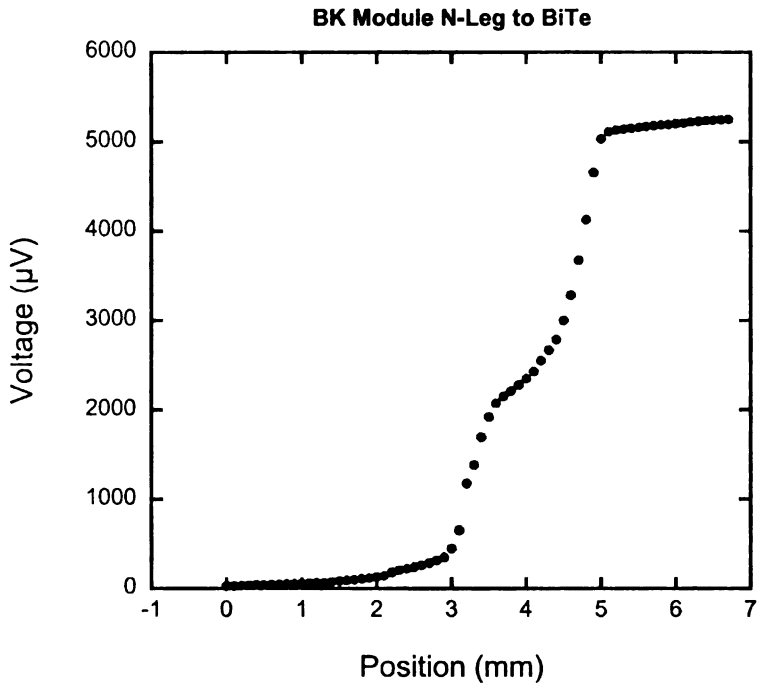

Figure 198: Scan of N leg of a module that ran for one week under a 585°C gradient.

As shown in Figure 198 the leg resistance increased. The properties of the leg changed after the diffusion bond. The module resistance went from 10mΩ to 50mΩ after operating for 7 days. EDS was done on the interface between the Bi_2Te_3 and LAST.

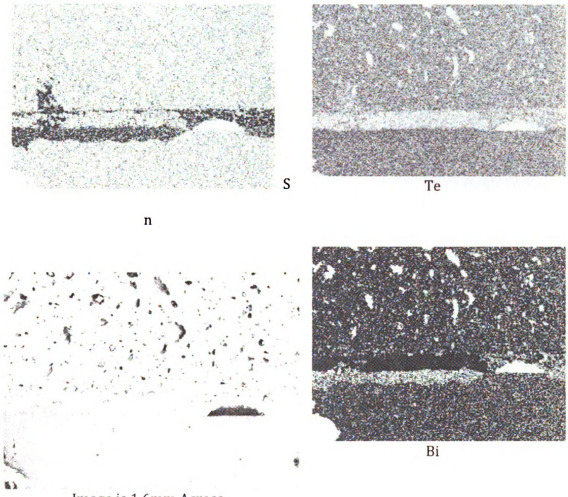

Figure 199: EDS of contact. Top is LAST, then solder junction (Bi-Sn-Sb), Bottom Bi_2Te_3.

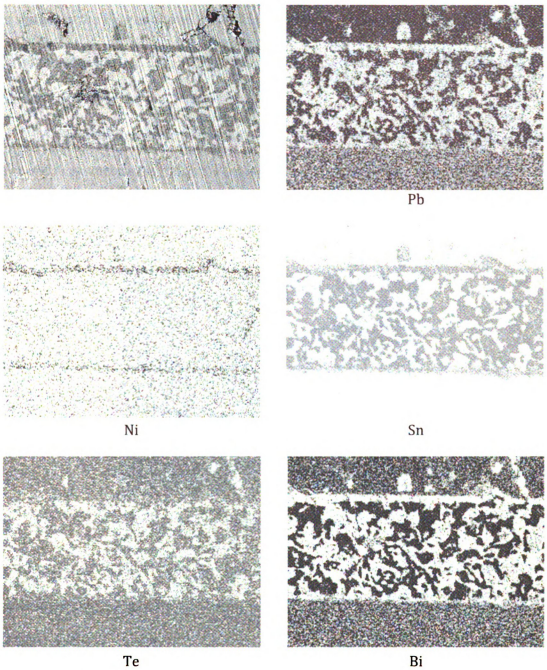

Figure 200: EDS of same junction as figure above, but at a higher magnification, the picture shows an area approximately 200μm across.

As shown in the figures above, bismuth looks to have diffused from the Bi_2Te_3 and the solder into the LAST material. This could be the reason why there is a change in the conductivity of the material.

A completed module underwent a testing of its mechanical stability by being dropped from increasing heights starting from 1 foot to 10 feet onto a concrete floor. To test the effects of each drop the resistance was documented followed by photographs.

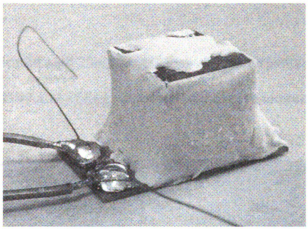

Figure 201: Module before drop testing.

The initial module resistance was 70mΩ. The drops between 1 foot and 8 feet did not change module resistance or damage the module. After dropping the module 9 feet the module resistance changed to 87mΩ. The figure below shows how the aluminum nitride cracked off of the bottom of the module.

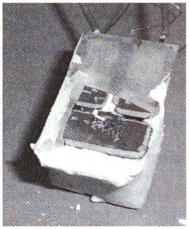

Figure 202: After the module dropped 9' the base aluminum nitride cracked.

A module was fabricated with 2 unicouples that was soldered together with a BiSbSn solder. ETN197 and ETP44 were used to build the module. The module is pictured below.

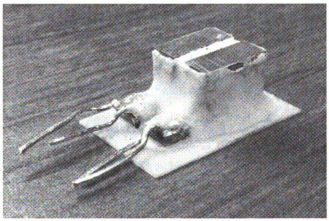

Figure 203: Module built with solder for contacts.

It was first thought to only use this module for a low delta T, but with the QS/B4 around the legs, the module could be used to higher temperatures than the melting point of the solder. If the solder melts the electrical contact on the hot side will then be liquid and allow for CTE mismatches between the LAST and the hot side

electrode. The QS/B4 would maintain the mechanical integrity of the module. More modules were built by this technique and will be discussed later.

A unicouple was soldered together at both the cold and hot side contacts with ETN152 and ETP44. A nickel-chromium-aluminum nitride cold side substrate was used. The hot side was nickel and was solder to the legs with a Bi-Sn-Sb solder. The room temperature resistance of the module was 6.4mΩ. The unicouple was placed into the LTMTS for measurement of the output power. With T_h=135.26°C and T_C=29.7°C the short circuit current was 700mA. The hot side temperature was raised to 196.3°C and the cold side temp was 30.34°C. The short circuit was 1.06 amps. The hot side temperature was set to 221.23°C and the corresponding open circuit voltage and short circuit current were 53.1 mV and 1.26 Amps respectively. The hot side temperature remained around 225°C for 5 days to see if the output of the module would change.

On the fifth day the hot side temperature was 225°C and the cold side was 29°C. The short circuit current was 1.27 Amps. Over the 5 days of operation the modules output did not decrease. There was no change in the current output, which gives evidence that module did not degrade over the 5 days of operation. After one week of operation the hot side temperature was 214°C and the short circuit current was 1.22 Amps. Slowly the hot side temperature was brought down to room temperature. The initial resistance of the module was 6.4mΩ and after the test the resistance changed to 7.6mΩ.

After the good results of "Unicouple Built," a second soldered module was built named "Ghost Rider." The substrate for the module was a metalized aluminum nitride.

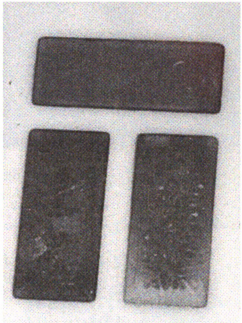

Figure 204: Cold side substrate for the module called Ghost Rider.

Figure 204 shows the nickel plated chromium contact that was deposited to aluminum nitride. Nickel plated copper was then soldered to the substrate as shown below.

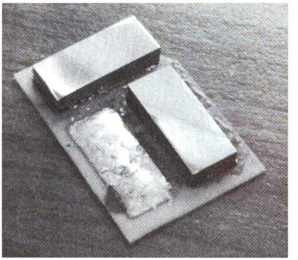

Figure 205: Cold side electrodes soldered to cold side substrate.

First the four legs of the unicouple were solder to the cold side electrodes before soldering on the copper hot side electrodes.

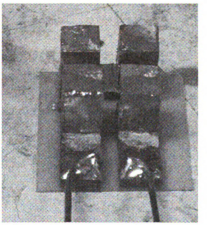

Figure 206: Front view of Ghost Rider's legs soldered to cold side.

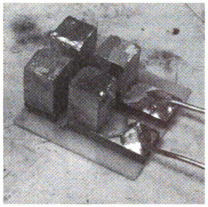

Figure 207: Thermoelectric legs soldered down to cold side.

The legs were then nickel plated and the copper was soldered to the hot side. The entire module was coated with QS/B4 with the completed module shown in Figure 208.

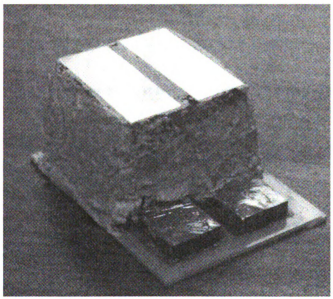

Figure 208 Ghost Rider

Figure 209: Ghost Rider output voltage and output current for a temperature gradient across the module of $\Delta T = 184°C$.

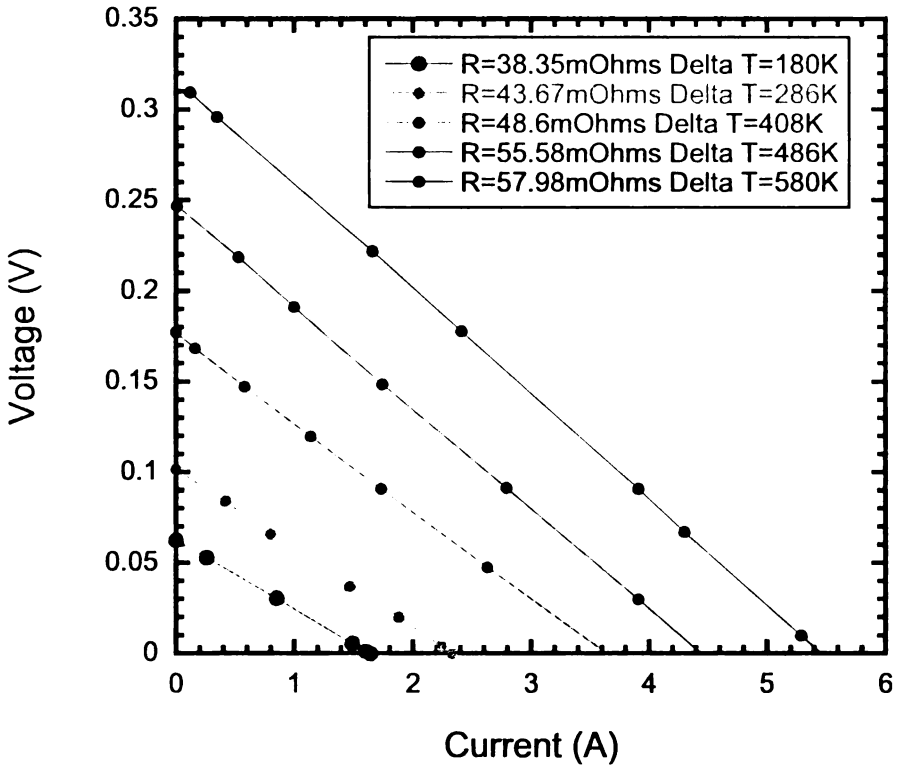

Figure 210: Ghost Rider I-V Characteristics.

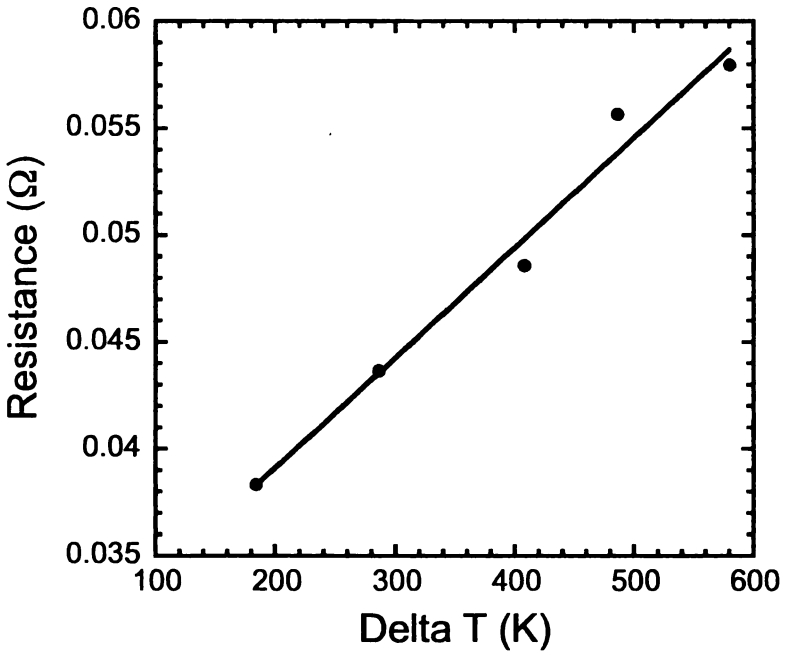

Figure 211: Plot of the resistance compared to the ΔT.

The straight line fit in Figure 211 gives a 0 ΔT resistance of 28.85mΩ. The actual room temperature resistance of the module was measured using a four probe configuration to be 15mΩ. This means there was around 15mΩ of parasitic resistances in the measurement setup (part of the measurement system, and external to the module). For a ΔT of 570°C the short circuit current of the module would have been closer to 7.2 amps, rather than the 5.5 amps measured if the parasitic resistance was zero.

Another 4 leg module was fabricated based on soldered junctions and the module was titled "Jen". For this module nickel instead of copper for the hot side electrodes was used, and the module resistance at room temperature was 24.1mΩ.

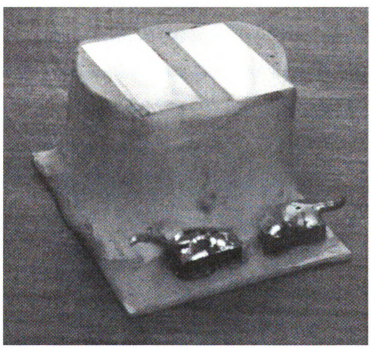

Figure 212: Module "Jen" built with cast materials and coated with QS/B4.

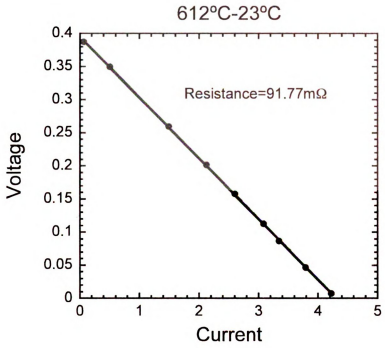

Figure 213: Output voltage and current for the four leg module "Jen" with a temperature gradient of 589°C.

With the higher module resistance, the short circuit current is lower for "Jen" than for "Ghost Rider", but the open circuit voltage is higher for "Jen". After running the measurement the room temperature resistance of "Jen" increased to 136mΩ. The QS/B4 was removed and the legs investigated.

Figure 214: Module "Jen", side view.

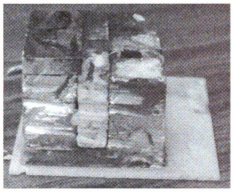

Figure 215: Module "Jen" rear view.

As shown in Figure 214 and Figure 215 no visible cracks or degradation of the legs could be seen, however increases in junction resistances may not be visibly apparent, and cutting marks left from removal of the QS/B4 may have masked cracks in the legs.

A simplified technique for fabrication of the cold side electrodes was also investigated. Using a double-sided thermally conductive tape the cold side electrodes were attached to the aluminum nitride substrate. With the ease for making contact to the aluminum nitride a 8 unicouple module was fabricated as shown in Figure 216.

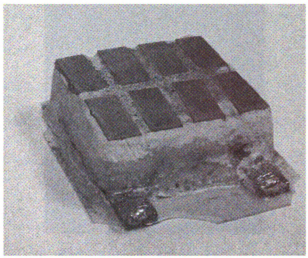

Figure 216: Sixteen leg module called "Tape".

The "Tape" module had a room temperature resistance of 160mΩ. The expected resistance of the module was 80mΩ. Some of the solder contacts may not have been bonded well. This module ran for 93 hours with a hot side temperature of 225.4°C and cold side temp of 25.1°C. The short circuit current was 440mA. With approximately the same ΔT the four leg module "Ghost Rider" was giving close to 1.5A of short circuit current.

A 4 leg module with 6.35mm thick nickel was also built, and the room temperature resistance was 27mΩ. This resistance is close to the resistance of the module "Jen".

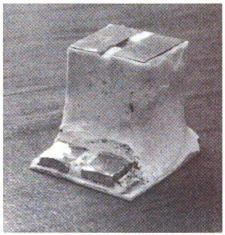

Figure 217: Four leg module using nickel electrodes and titled "0001".

Module "0001" had an open circuit voltage of 23.4mV with a hot side temperature of 96.6°C. The hot side temperature was increased to 98.2°C and the short circuit current was measured, 270mA. With the hot side at 118.6°C, the short circuit current increased to 353mA. For modules previously built, the short circuit current at this ΔT was nearly 1Amp. This module was not showing good results so it was shut down.

A module was built with ETP52 and MSUHP-41-N. The resistance of the module was 362mΩ. This modules resistance is very high; one leg of the module typically is only 3.18mΩ, however the hot pressed material is known to have a lower electrical conductivity at room temperature (then increasing with increasing temperature). The room temperature resistance of 362mΩ was still an order of magnitude too high. Normally a hot pressed leg has a room temperature resistance of approximately 20mΩ. The legs of the module may have cracked during the

soldering process. Results in the past have shown legs cracking during soldering, but during recent constructions this has not been the case.

A module was built with another set of legs from MSUHP-41-N and ETP52. For the p-type material Cerromatrix™ solder was used, and for the n-type leg, the BiSnSb solder alloy was used. The 0.25" nickel was used as the hot side electrode.

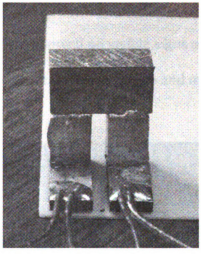

Figure 218: Module 7-09-08-2Leg.

The module was placed in the LTMTS. With a hot side temperature of 247.1°C and cold side temperature of 18.4°C the open circuit voltage was 122.9mV and short circuit current was 354mA. Based on these measurement the calculated resistance of the module at this ΔT was 346mΩ. The expected resistance of the module for this temperature gradient is XX mΩ.

Dr. Nurraddin Matchanov built a unicouple using SnTe as the contact material. The unicouple's resistance was 6mΩ. It was put into the LTMTS for testing.

Table 8: SnTe unicouple measurements.

Hot side Temperature (°C)	Cold Side Temperature (°C)	Open Circuit Voltage (mV)	Short Circuit Current (A)	Unicouple Resistance (mΩ)
191.1	16.8	-	1.3	-
248	17.4	82.8	1.97	41.6
316	18.2	113.5	2.8	40.5
381.8	19.6	150	3.16	47.8
497	21.9	194.4	3.8	51.15

After running the module there showed no visible signs of degradation of the unicouple. The unicouple was not coated in QS/B4 and measurements were taken in an argon atmosphere.

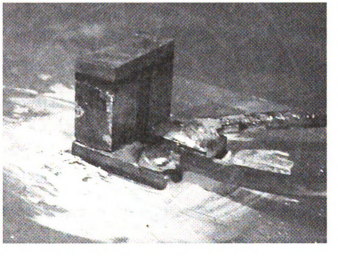

Figure 219: Nuraddin's SnTe unicouple after running in the LTMTS.

6.0 Conclusions and Future Directions

6.1 Conclusions

This dissertation has been a record of experiments done in diffusion bonding, temperature cycling, and long term tests. Diffusion bonds were attempted to many different materials. Bonds to 410 and 316 stainless steel produced good results. Some modules were fabricated with a direct soldering of the hot side electrode, and have given high short circuit currents at maximum ΔTs.

These contacts were subjected to temperature cycling. Contacts such as nickel showed that the material fractures after temperature cycling, while bonds to 316 stainless steel do not. Mechanical pressure showed an importance during bonding. Many bonding runs did not have uniform mechanical pressure. Runs that kept close measurement of individual mechanical bonding pressure showed 100% bonding yield.

Bonds were studied to distinguish if the bonding material poisons or degrades the thermoelectric material. Measurements of the thermoelectric properties along with EDS plots were done. EDS showed that mostly tellurium, chromium, and nickel would readily diffuse through contact materials as well as the thermoelectric leg itself.

Diffusion barriers of molybdenum were studied but showed to not bond with the LAST material. Other experiments in the lab have shown if SnTe is added to the contact, molybdenum coated LAST bonds to stainless steel.

A system has been built to measure contact resistances at high temperatures (700K), by other teammates in the lab [reference Farhan's thesis].

Spring loaded module designs have been investigated and built. None of these modules entered the measurement phase due to high resistances. Recent results have shown high contact resistances with a pressed contact of LAST to copper.

In all, the main challenge is the LAST and LASTT material. Contacts to these materials have been made and shown to have low contact resistance, but during operation or fabrication of these contacts the LAST material has a propensity to fracture. Initial investigations were done to powder process this material and hot press to increase the strength and uniformity of its properties, but this showed to be a challenge. Significant increases (three fold) in sample fracture strength has been made through powder processing, however additional challenges of sample bloating and good repeatability require further studies.

6.2 The Next Step, Spark Plasma Sintering

Spark plasma sintering (SPS) is an innovative technique for pressing and sintering powders. Powders are loaded into a graphite die and while pressing the material a large DC current is passed through the die and material. Unlike hot pressing that uses external heating elements to the graphite die, the die and the powder charge are heated due to the electrical current. This allows for rapid heating and cooling of the material. Also a novel idea is to press an entire thermoelectric part at once. The n-type, p-type, and electrode can be pored into the die at once and sintered all together. The tooling of the graphite die would govern the temperatures of the different zones to be sintered. Work has been done on $AgPb_mSbSe_{m+2}$ materials in an SPS system, which is a cousin to the LAST material

[75]. These materials have shown comparable results to that of the LASTT materials. SPS will also speed up the production of material as it was shown in the SPS of β-$FeSi_2$ [76]. Lastly, Zhou has SPS a high lead content LAST material and has shown outstanding ZTs [77]. Their materials showed ZTs above 1 and improvement of the thermal conductivity after a 30 day anneal. Perhaps the best feature of SPS processing is the rapid throughput such that a variety of parameter adjustments can be investigated in a relatively short amount of time.

References

[1] Thomas Johann Seebeck, http://chem.ch.huji.ac.il/~eugeniik/history/seebeck.html. 8/29/2009.

[2] Introduction into Thermoelectrics, *http://www.thermoelectrics.com/introduction.htm#ref3*

[3] Sim Loo, "Transport Characterization of New High Temperature Quaternary Thermoelectric Materials And Devices", Ph.D. thesis, Michigan State University, 2003.

[4] A. F. Ioffe, "Semiconductor Thermoelements and Thermoelectric Cooling", Infosearch Limited, London, 1957.

[5] M. G. Kanatzidis, "The Role of Solid-State Chemistry in the Discovery of New Thermoelectric Materials," in *Solid State Physics*, ed. H. Ehrenreich, F. Spaepen, vol. 69, pp 51-100, Academic Press, New York, 2001.

[6] Kuei Fang Hsu et al., "*Cubic $AgPb_mSbTe_{2+m}$ Bulk Thermoelectric Materials with High Figure of Merit*," Vol. 303, Science, www.sciencemag.org

[7] H.J. Goldsmid, "The use of semiconductors in thermoelectric refrigeration," British Journal of Applied Physics, pages 386-390, 1954.

[8] M.H. Ettenberg, W. A. Jesser and P.D. Rosi, "A New n-type and Improved p-type Pseudo-ternary $(Bi2Te_3)(Sb_2Te_3)(Sb_2Se_3)$ Alloy for Peltier Cooling," Proc. 15th Int. Conf. On Thermoelectrics 52-56, 1996.

[9] M.G. Kanatzidis, "The role of Solid-State Chemistry in the Discovery of New Thermoelectric Materials," in Solid State Physics, ed. H. Ehrenreich, F. Spaepen, Vol. 69, pp 51-100, Academic Press, New York, 2001.

[10] R.P. Chasmar and R. Stratton, J. Electron. Control 7, 52 (1959).

[11] L.D. Hicks, M.S. Dresselhaus, "Effect of quantum-well structures on the thermoelectric figure of merit," Phy. Rev. B, Vol. 47, no. 19, pp. 12727, 1993.

[12] G. Mahan, "Good Thermoelectrics," Solid State Physics, vol. 51,pp 82-155, 1997.

[13] G.A. Slack, *CRC Handbook of Thermoelectrics,* ed. D.M. Rowe, 1995, pp. 407-440.

[14] H. Scherrer and S. Scherrrer, *CRC handbook of Thermoelectrics,* pp. 211-237

[15] G. Mahan, "Good Thermoelectrics," Solid State Physics, vol. 51, pages 113-114, 1997

[16] C.B. Vining, CRC Handbook of Thermoelectrics, pp. 329-337

[17] G. Mahan, "Good Thermoelectrics," Solid State Physics, vol. 51, pages 115-116, 1997

[18] A.L. Jain, "Temperature Dependence of the Electrical properties of bismuth antimony alloys," Physical Review, Vol. 114, No. 6, June 15, 1959.

[19] G. Mahan, "Good Thermoelectrics," Solid State Physics, vol. 51, pages 116, 1997

[20] G. Mahan, "Good Thermoelectrics," Solid State Physics, vol. 51, pages 117-119, 1997

[21] G.S. Nolas, D.T. Morelli, T.M. Tritt, "Skitterudites: A Phonon-Glass-Electron Crystal Approach to Advanced Thermoelectric Energy Conversion Applications," Annual Review Material Science, pp. 89-116, 1999.

[22] G.S. Nolas, et al., "High figure of merit in partially filled ytterbium skutterudites materials," Appl. Phys. Letts. Vol 77, No. 12, 2000

[23] G.A. Lamberton, et al., "High figure of merit in Eu-filled $CoSb_3$-based skutterudites," Applied Physics Letters, Vol. 80, No. 4, 2002

[24] G.S. Nolas, et al., "Semiconducting Ge clathrates: Promising candidates for thermoelectric applications, Applied Physics Letter, Vol. 73, No. 2, July 13, 1998

[25] G.S. Nolas, et al., "Transport properties of polycrystalline type-I Sn clathrates," Physical Review B, Vol. 65, 165201, 2002

[26] S. Bhattacharya, et al., "Effect of Sb doping on the thermoelectric properties of Ti-based half-Heusler compounds, $TiNiSn_{1-x}Sb_x$," Applied Physics Letters, Vol 77, No. 16, 16 October 2000.

[27] E. A. Skrabek and D.S. Trimmer, CRC Handbook of Thermoelectrics, ed. D.M. Rowe, 1995, pp. 267-274

[28] R. Venkatasubramanian, "Thin-film thermoelectric devices with high room-temperature figure of merit," Nature, 2001

[29] R. Venkatasubramanian, et al., "Low temperature organometallic epitaxy and its application to superlattice structures in thermoelectrics," Appl. Phys. Lett. 75, 1104-1106 (1999)

[30] R. Venkatasubramanian, "Low temperature chemical vapor deposition and etching apparatus and method," US Patent No. 6071351 (6 June 2000).

[31] T.C. Harman, et al., "Quantum Dot Superlattice Thermoelectric Materials and Devices," Science, Vol. 297, Sep. 27, 2002

[32] N.F. Mott, "The Theory of the Properties of Metals and Alloys," Dover Publications, New York, NY.

[33] L. D. Hicks, M. S. Dresselhaus, "Effect of Quantum-Well Structures on the Thermoelectric Figure of Merit," *Physical Review B*, Vol. 47, No. 19, pp. 12 727-12 731, 1993.

[34] T. C. Harman, M. P. Walsh, B. E. LaForge, G. W. Turner, "Nanostructured Thermoelectric Materials," *Journal of Electronic Materials*, 34 (5), pp. L19-L22, 2005.

[35] D.M. Rowe, "Handbook of Thermoelectrics," CRC Press, 1995, pp 496- 497

[36] M.H. Cobble, "Calculations of Generator Performance," *CRC Handbook of Thermoelectrics*, CRC Press, 1995.

[37] T. Caillat, et al, "Development of a High Efficiency Thermoelectric Unicouple for Power Generation Applications," 18th International Conference on Thermoelectrics, 1999.

[38] F. Chen, "Low-frequency ac measurement of the Seebeck coefficient," *Rev. Sci. Instrum.*, vol. 72, no. 11, 2001, pp. 4201-4206.

[39] A. T. Burkov, A. Heinrich, P. P. Konstantinov, T. Nakama, K. Yagasaki, "Experimetal set-up for thermopower and resistivity measurements at 100-1300K, " *Meas. Sci. Technol.*, vol. 12, 2001, pg. 264-272.

[40] A. L. Pope, R. T. Littleton, T. M. Tritt, "Apparatus for the rapid measurement of electrical transport properties for both "needle-like" and bulk materials," *Rev. Sci. Instrum.*, vol. 72, no. 7, July 2001, pp. 3129-3131.

[41] R. T. Littleton IV, et. al., "High Temperature Transport Probe for Thermopower and Resistivity Measurement," *Materials Research Society Symposium Proceedings,* 1998.

[42] Z. Zhou, C. Uher, "Apparatus for Seebeck coefficient and electrical resistivity measurements of bulk thermoelectric materials at high temperature," *Rev. Sci. Instrum.,* vol. 76, 2005.

[43] M. Putti, M. R. Cimberle, A. Canesi, C. Foglia, A. Siri, "Thermopower measurements of high-temperature superconductors: Experimental artifacts due to applied thermal gradient and a technique for avoiding them," *Phys. Rev. B,* vol. 58, no. 18, Nov. 1998.

[44] Downey, Adam Darwin, "Advancing Thermoelectric Research with New Measurement Systems and Thermoelectric Modeling for AC Electrical Measurements," Ph.D. Dissertation, Michigan State University, 2006.

[45] Merker J., Lupton D., Töpfer M., Knake H., "High Temperature Mechanical Properties of the Platinum Group Metals," Platinum Metals Review, Volume 45, Number 2, 1 April 2001 , pp. 74-82(9).

[46] Kuei Fang Hsu et al., "Cubic $AgPb_mSbTe_{2+m}$ Bulk Thermoelectric Materials with High Figure of Merit," Vol. 303, Science, www.sciencemag.org

[47] M. G. Kanatzidis, "The Role of Solid-State Chemistry in the Discovery of New Thermoelectric Materials," in Solid State Physics, ed. H. Ehrenreich, F. Spaepen, vol. 69, pp 51-100, Academic Press, New York, 2001.

[48] N. Uchitomi et al., "Characterization of a β-$FeSi_2$ p-n junction formed by the PECS method," Thin Solid Films 461, pp 174-178, Science Direct, 2004.

[49] N. Jaussaud et al., "n- and p- Type behavior of the gold-substituted type-I clathrate, $Ba_8Au_xSi_{46-x}$ (x=5.4 and 5.9)," C.R. Chimie 8, pp 39-46, Science Direct, 2005.

[50] S. Schlecht et al., "Nanoscale Zinc Antimonides: Synthesis and Phase Stability,"
Inorganic Chemistry, 45, pp 1693-1697, 2006.

[51] Y. Gelbstein et al,. "Powder metallurgical processing of functionally graded p-$Pb_{1-x}Sn_xTe$ materials for thermoelectric applications," Physica B 391, 2007, pages 256-265

[52] T. Pham Hong, et al., "Water Absorption in a Glass-Mica-Epoxy Composite I: Influence on Electrical Properties," IEEE Transactions on Dielectric and Electrical Insulation Vol. 16, No. 1; February 2009.

[53] A.A. Shirzadi, H. Assadi and E.R. Wallach, "Interface Evolution and Bond Strength when Diffusion Bonding Materials with Stable Oxide Films," Suface and Interface Analysis 2001; 31:609-618.

[54] I. Cadoff, E. Miller, "Thermoelectric Materials and Devices," Reinhold PublishingCorporation, 1960, pp. 68.

[55] W. D. Callister Jr, "Material Science and Engineering," Third Edition, John Wiley & Sons, INC., 1994, pp. 646.

[56] F. Ren, E.D. Case, E.J. Timm, et al., Phil. Mag. Lett. 86 (2206) p. 673.

[57] D.A. Porter and K.E. Easterling, "Phase Transformations in Metals and Alloys," 1993, Chapman and Hall.

[58] W. D. Callister, Jr. "Materials Science and Engineering An Introduction," Sixth Addition, John Wiley & Sons, Inc. 2003, pp. 221-224.

[59] S.-X. Li et al., "A Probabilistic Model for Prediction of Bonding Time in Diffusion Bonding," Materials Science and Engineering A 407 (2005) 250-255

[60] W. D. Callister, Jr. "Materials Science and Engineering An Introduction," Sixth Addition, John Wiley & Sons, Inc. 2003, pp. 222.

[61] A. L. Eiss, "Studies of Lead Telluride Thermoelectric Elements," Hittman Associates, Inc. Baltimore, Maryland.

[62] Y. Kuru et al., "Interdiffusion and Stress Development in Thin Film Diffusion Couples," Materials Science Forum Vols. 524-525 (2006) pp. 801-806.

[63] A. Smigelskas and E. Kirkendall, *Trans.* AIME, 171, 130 (1947).

[64] H. Ono, T. Nakano, and T. Ohta, "Diffusion Barrier Effects of Transition Metals for Cu/M/Si Multilayers (M=Cr, Ti, Nb, Mo, Ta, W)," Appl. Phys. Lett. 64 (12) 21 March 1994.

[65] Kyung-Hoon Min, Kyu-Chang Chun, and Ki-Bum Kim, "Comparative Study of Tantalum and Tantalum Nitrides as Diffusion Barrier for Cu Metallization," J. Vac. Sci. Technology B 14(5), Sep/Oct 1996.

[66] R. C. Weast, M. J. Astle, and W. H. Beyer, "CRC Handbook of Chemistry and Physiscs," 64th edition, CRC, Boca Raton, Florida, 1983, p. F-47.

[67] R. J. Borg, G. J. Dienes, "An Introduction to Solid State Diffusion," Academic Press 1988, pp. 81.

[68] Jonathan D'Angelo, "Low Resistance Contacts to Thermoelectric Materials," M.S. Thesis, Michigan State University, 2006.

[69] A. D. Downey, T. P. Hogan, B. Cook, "Characterization of thermoelectric elements and devices by impedance spectroscopy," *Review of Scientific Instruments,* Vol. 78, No. 9, 2007.

[70] G. Q. Wu, et al., "The effects of various finished surfaces on diffusion bonding," Modeling and Simulation in Materials Science and Engineering, 16, 2008

[71] B. I. Boltaks, "Diffusion in Semiconductors," Academic Press, New York, 1963, page. 57

[72] P. F. P. Poudeu, J. D'Angelo, A. Downey, J. L. Short, T. P. Hogan, M. G. Kanatzidis, "High thermoelectric figure of merit and nanostructuring in bulk p-type $Na_{1-x}Pb_mSb_yTe_{m+2}$," Angewandte Chemie-International Edition, Vol. 45, No. 23, pp. 3835-3839, 2006

[73] www.tellurex.com, 3-9-2009

[74] Arledge, et al., "Adherent metal coating for aluminum nitride surfaces," 5,382,471, January 17, 1995

[75] K.F. Cai, et al., "Preparation and thermoelectric properties of $AgPb_mSbSe_{m+2}$ materials," Journal of Solid State Chemistry 181 (2008), pages 1434-1438.

[76] K. Nogi, T. Kita, "Rapid production of β-$FeSi_2$ by spark-plasma sintering," Journal of Materials Science 35, 2000, pages 5845-5849.

[77] Min Zhou, et al., "Nanostructured $AgPb_mSbTe_{m+2}$ System Bulk Materials with Enhanced Thermoelectric Performance," JACS Articles, 03/08/2008.